Towards laser cooling and trapping of unstable caesium atoms

by

Alexandros Giatzoglou

Supervisor: Prof. Ferruccio Renzoni

Department of Physics and Astronomy

University College London

United Kingdom

15 April 2019

I, Alexandros Giatzoglou, confirm that the work presented in this thesis is my own. Where information has been derived from other sources, I confirm that this has been indicated in the thesis.

Signed ..... Date .....

Abstract

The thesis reports on the work I carried out during my PhD to set up and test a new experimental facility at the Accelerator Laboratory of the University of Jyväskylä, Finland. The final aim was the realisation of a facility for cooling and trapping unstable caesium atoms.

Ideally, my work can be divided in two phases, and the structure of this thesis mirrors this goal. The first phase of the work led to setting up the off-line, i.e. independent from the accelerator, set-up for laser cooling and trapping at the Accelerator Laboratory in Jyväskylä. This was necessary to test the effectiveness, robustness, and stability of our laser, optical and control systems for creating and fully-characterising a magneto-optical trap (MOT) of stable ^{133}Cs in the harsh and noisy environment of the Accelerator Laboratory. This required dedicated design of the experimental set-up, with requirements and specifications more strict than those of a conventional atomic physics experiment. The second phase led to setting up the complete, on-line experiment, with the atom-trapping chamber being permanently connected to one of the accelerator's beam lines positioned within the IGISOL-4 facility.

Tests and full characterisation of the "on-line" set-up were conducted. This led to the successful production of a MOT from neutralised $^{133}Cs^{+}$ produce as a high-energy beam. At full operation, ^{133}Cs is brought from 10^{4} eV to 10^{-8} eV in around 5 s. Tests with radioactive beams were also performed and preliminary results are discussed in the thesis.

Atomic samples were cooled down to 150 μK. This opens avenues for precision spectroscopy of unstable atomic samples and nuclear forensic applications. In the long term, the facility will allow the realisation of an isomeric Bose-Einstein condensate (BEC), constituting an experimental benchmark for the recently proposed theory of collective gamma-ray decay.

Impact Statement

The work reported in this thesis is the result of an international collaboration between University College London (UCL), United Kingdom and the University of Jyväskylä (JYU), Finland. In 2016, the Laser Cooling group of UCL begun the assembly of a facility for laser cooling of Cs isotopes and isomers, coupled to one of the K130 cyclotron's beam lines positioned in the IGISOL-4 area of JYU's Accelerator Laboratory. The facility has been fully operational since the end of 2017. Our work has been supported by various funding bodies from inside the UK and the European Union: Engineering and Physical Sciences Research Council (EPSRC), Atomic Weapons Establishment (AWE) and the European Commission under Horizon 2020. The research has short-term and long-term benefits for both inside and outside academia.

Ultra-cold gases, due to the reduced atomic motion, constitute the perfect environment for testing theories and gaining a deeper understanding in fundamental physics. The facility in JYU is the first laser cooling and trapping facility dedicated to Cs in Europe. It will open avenues for acquiring high-precision spectroscopic data for a chain of unstable isotopes and isomers, and testing new theories. Academia will also benefit from the collaboration between UCL and JYU since it provides a solid ground for joining expertise towards new research challenges, and cross-field and cross-country mobility of researchers and students.

Our facility also constitutes the first milestone towards the recently proposed theory of coherent gamma-ray generation using ultra-cold caesium atoms excited in higher nuclear states (isomers). The generation of coherent gamma-rays, once listed in the 30 most important physics problems, will have a huge impact inside and outside academia. Some of the sectors that can benefit from high-energy coherent gamma-rays are as follows: the medical field (e.g. preciser and safer stereotactic surgery), the security sector (e.g. higher resolution and shorter exposure time in gamma-imaging) and fundamental research fields (detectors' calibration, material testing etc.). In addition, the facility could be used for creating and validating nuclear forensic techniques. The ratio of some of the caesium isotopes have been long proven to be a valuable tool for non-proliferation and environmental monitoring purposes, and cold-atom techniques can detect them with high precision.

Our work contributes to UCL's, and UK's in general, impact in science. The UCL's Laser Cooling group has presented results related to the facility in Finland in numerous physics and industry international conferences, including four poster and two oral presentations, and one invited talk. The best poster awards have been received for our presentations in

the European Radioactive Ion Beam (EURORIB2018) conference and in the Defence and Security Doctoral Symposium (DSDS15). The facility's progress and results have been also presented by our collaborators in Finland in conferences and public engagement events. In addition, recently the results from the experimental demonstration of the facility's operation were published in the international peer-reviewed journal *Nuclear Instruments and Methods in Physics*. Finally, the project is featured in the STFC and CORDIS (European Commission) websites.

Acknowledgments

I would like to express my gratitude to all the persons that helped me during my PhD journey and had a positive effect on my work and my personal development.

First I would like to thank my supervisor, Prof. Ferruccio Renzoni, for giving me the opportunity to work with his group and introduced me to the field of laser cooling and trapping. It is always a pleasure to meet and work with highly intelligent and enthusiastic people.

Dr. Luca Marmugi has been supporting and guiding me from my first day in Ferruccio's group. He taught me a lot about almost every aspect of my PhD work, from the theory behind laser cooling to how tight CF components have to be. He is one of the most skilled and determined experimental physicists I have met so far, and I am looking forward to watch his scientific impact keep increasing year by year. Moreover, I would like to thank Mr. Tanapoom Poomaradee (aka Pik) for his work and contribution in the progress of our experiment. Pik is a natural problem-solver and skilled experimental physicist.

My PhD work would never reach the current level without my colleagues in the IGISOL group. I would like to thank Prof. Iain Moore for his continuous guidance and support during the years I have spent working with IGISOL. He made me a part of the group (although I was just a long-term visitor), provided me with everything that I needed during my work, and he even introduced me in the Finnish night-life. The continuous encouragement to all the IGISOL members and students is just one of the numerous characteristics that make Iain a great scientist, tutor and leader. I am definitely going to miss his British humour. I also owe special thanks to Dr. Sami Rinta-Antila and Dr. Ilkka Pohjalainen for teaching me so many things regarding experimental nuclear physics, and specifically Ilkka for sharing his knowledge in programming and 3D-designing with me. I will not list all the members of IGISOL here, although all of them have been very helpful, and I am really grateful for working and collaborating with them.

Finally, I would like to thank my family for believing in me and supporting me with all the means they had during the 9 years of my university studies.

Contents

1 Introduction **9**

1.1 Long-term goals . . . 9

1.1.1 High-precision spectroscopy of caesium isotopes and isomers . . . 9

1.1.2 Coherent gamma-ray source . . . 10

1.1.3 Nuclear forensics . . . 10

1.2 Theoretical background . . . 11

1.2.1 Isotopes and isomers . . . 11

1.2.2 Alkalis: structures and frequency shifts . . . 13

1.2.3 Laser cooling and trapping of neutral atoms . . . 16

2 First Phase: Offline set-up **22**

2.1 Experimental set-up . . . 22

2.1.1 Laser system . . . 22

2.1.2 MOT configuration . . . 25

2.2 Imaging system: absorption imaging . . . 30

2.2.1 MOT number of atoms . . . 31

2.2.2 MOT temperature, spatial and phase-space density . . . 32

2.3 Controlling the experiment . . . 34

2.3.1 Hardware controls . . . 34

2.3.2 Software controls . . . 34

2.4 ^{133}Cs MOT characterisation . . . 36

2.4.1 Loading rate and lifetime . . . 36

2.4.2 Temperature, density and phase-space density measurements . . . 47

3 Second Phase: On-line set-up **55**

3.1 Experimental set-up . . . 57

3.1.1 Ion-optics: X-Y plates and Einzel Lens . . . 58

3.1.2 Dedicated beam line . . . 59
3.1.3 MOT set-up . . . 61
3.2 MOT characterisation: fluorescence imaging . . . 72
3.2.1 Fluorescence signal calibration . . . 73
3.3 Characterisation of the facility: MOT from $^{133}Cs^{+}$ beam . . . 74
3.3.1 Diffusion and trapping: slow and fast dynamics . . . 75
3.3.2 Loading from pre-implanted foil . . . 77
3.3.3 Direct loading from the $^{133}Cs^{+}$ beam . . . 79

4 Towards ^{134,135}Cs trapping **83**
4.1 Hyperfine splitting and isotope shifts of unstable Cs . . . 83
4.1.1 Preparing the laser system for Cs isotopes . . . 86
4.2 On-line tests: production and implantation of radioactive beams . . . 88
4.2.1 ^{134}Cs . . . 89
4.2.2 ^{135}Cs . . . 91

5 Conclusions and Outlook **99**
5.1 Future work . . . 101

Chapter 1

Introduction

1.1 Long-term goals

A facility for laser cooling and trapping stable and unstable Cs atoms has been installed in the Accelerator Laboratory of the University of Jyväskylä (JYU), Finland, and is coupled to one of the K130 cyclotron's beam lines within IGISOL-4 [1]. The operation of the facility was recently demonstrated using a stable beam of $^{133}Cs^{+}$ [2]. The ions were successfully neutralised and trapped in a magneto-optical trap (MOT). The production of ultra-cold atomic samples of unstable caesium atoms has the potential to broaden our knowledge on nuclear structure, to provide more accurate trace detection of isotopes and isomers, and to constitute the building block towards the demonstration of collective phenomena in ultra-cold nuclear matter. The main long-term goals of the research are described in the following.

1.1.1 High-precision spectroscopy of caesium isotopes and isomers

The cold temperatures in a MOT (or ultracold in a Bose-Einstein condensate (BEC)) allow long and Doppler-free interrogation times, giving the possibility for very high-precision spectroscopy [3]. Precise measurements of the hyperfine constants A and B of isotopes and isomers as well as isotopic and isomeric shifts of optical transitions, e.g. for ^{134,134m}Cs, has not only high value for the field of spectroscopy, but can provide new data for the investigation of charge radii anomalies in Cs isotopes (e.g. see [4] for ^{178}Hf). Laser-cooled radioactive atoms have also been used for Standard Model tests [3] [5].

By trapping unstable Cs isotopes in a MOT, the facility will provide opportunities for high-precision determination of the hyperfine structure and isotope shifts with various methods, such as trap depletion [6] [7] and two-photon spectroscopy [3] using fluorescence imaging and absorption spectroscopy based on absorption imaging. Lock-in detection

techniques will be implemented when needed to reduce the background and increase the measurements' sensitivity.

1.1.2 Coherent gamma-ray source

The production of coherent gamma-rays by exploiting the coherence transfer, triggered by the spontaneous emission of a γ-photon, from an isomeric BEC to the γ-photon field has been recently proposed [8]. This "double-coherence" will result in a catastrophic collapse of the BEC and the production of a coherent directional γ-burst. The proposed candidate isomer is the ^{135m}Cs with nuclear spin J^{π} =19/2^{-} and half-life $T_{1/2}$ =53 min, decaying to an intermediate level J^{π} =11/2^{+}, emitting an M4 846.1 keV γ-photon and immediately after to the ground state, ^{135}Cs with J^{π} =7/2^{+}, via the emission of an E2 786.8 keV γ-photon.

Recent measurements [2] in IGISOL-4 showed that the ^{135m}Cs is produced in sufficient numbers, and specifically more than 10^4 isomers/s can be successfully delivered to our accelerator-coupled laser cooling facility. The technology for establishing quantum degeneracy, i.e. achieving a BEC of Cs, is well established and readily available. While BECs of unstable Cs atoms (or of any other unstable species) have not been produced yet, there are no fundamental differences in the laser cooling and trapping processes involved to the ones of the stable case. The difficulties in achieving a BEC of unstable species arise mainly from the fact that the latter are produced in small numbers. The procedure of realising a BEC would normally include a forced evaporation stage, which induces huge losses that can be detrimental for trapping unstable atoms. Nevertheless, recently, BEC approaches which induce small losses have been experimentally demonstrated. A notable example is the realisation of an ^{87}Rb BEC, starting from just 2000 atoms (placed in an optical lattice), and achieving the quantum degeneracy of 1400 atoms ($\sim$30% losses) using only laser cooling techniques (Raman sideband cooling) [9]. "Sympathetic cooling" is another potential candidate for circumventing evaporation processes and minimising losses [10].

1.1.3 Nuclear forensics

The ratio ^{135}Cs/^{137}Cs can be a useful forensic tool for discriminating between fission conditions and reactor types. Characteristically, in Russel et al. [11], a difference of a factor $\sim$5 (as deduced from their published graph where numerous sources are cited) is shown, between the measured values of ^{135}Cs/^{137}Cs from samples of nuclear weapon test fallouts and the characteristic isotopic signature of Chernobyl accident's fallout. In addition to

their non-proliferation applications, the ^{135}Cs/^{137}Cs and the ^{134}Cs/^{137}Cs ratios can act as geochemical tracers and time markers. A representative example is the use of these ratios to follow the environmental impact of the Fukushima Daiichi accident [12], and to identify the contribution from each of the reactor units and spent fuel pools involved [12] [13].

A MOT can overcome difficulties faced by nuclear and mass spectrometry techniques, such as the decay mode, the interference signals from strongly abundant isotopes and the long half-life of ^{135}Cs ($T_{1/2}$ =2.3×10^6 years), and can determine the ^{135}Cs/^{137}Cs and ^{134}Cs/^{137}Cs with very high accuracy. Using a similar facility to the one installed in JYU, Di Rosa et al. [14] reported very high selectivity and a lower limit of 4% in their accuracy in determining the ratio ^{135}Cs/^{137}Cs, which is comparable to the majority of the cutting-edge mass spectrometry techniques [15].

1.2 Theoretical background

1.2.1 Isotopes and isomers

Isotopes are atoms with the same number of protons, Z, and electrons (when not in an ionic form), but a different number of neutrons, N, in their nucleus. The total number of the nucleons (protons and neutrons) in the atomic nucleus is called the mass number, and it is defined as A=N+Z. Isotopes (of the same element) are usually chemically indistinguishable due to the fact that the chemical properties of an atom are mainly defined by its electronic structure. Nevertheless, the isotopes can be distinguished based on their physical properties (e.g. mass, volume etc.), as it is routinely happening for example in a mass-separator coupled to a cyclotron. The term “isotope” was first used by Frederic Soddy [16]. Based on their nuclear properties, they can be categorised as stable or radioactive isotopes (radioisotopes). To date, more than 3200 isotopes have been discovered, with only ∼300 being stable.

In physics, an atom is defined as an isomer when one (or more) of its nucleons is excited to a nuclear state, as those described by the shell model, with a commonly accepted half-life lower limit ≥ns. These excited quantum states are usually described as “metastable” (due to their relatively long half-life), and their excitation energies range from ∼eV (e.g. ^{229m}Th) to MeV (e.g. ^{206m}Bi). Frederic Soddy was the first who predicted the existence of isomers by identifying isotopes who had the same mass (in addition to being chemically identical) but different half-lives and decaying modes [17]. A few years later, in 1921, the first experimental observation of nuclear isomers was made by Otto Hahn [18],

and the first theoretical explanation was published from von Weizsäcker [19] in 1936. A detailed review on isomers is presented in [20].

The isomers are divided in three categories based on the underlying energy-trap mechanism [21]: *Shape isomers* − Occur in the presence of a secondary energy minimum, separate from the ground state, which is considered the primary minimum, at large nucleus's elongations. *Spin-trap isomers* − The spin of the isomeric state is significantly larger than the spin of the next lower energy state. *K-trap isomers* − K isomers are named after the K quantum number, which is used to describe the projection of the total nuclear spin along the nucleus's symmetry axis. Those isomers are different, not only in the magnitude, but also in the orientation of their spin vector with respect to the lower energy state. For all the isomeric cases above, the excitation energy of the isomer is considered "trapped" (thus the term energy-traps) due to the lower probability meeting the shape/spin/spin-orientation conditions of the lower energy state that they are decaying to. The isomer is eventually deexcited via α/β decay, proton/neutron emission, isomeric transition (IT), fission or gamma emission. The most common decay process for isomers is IT, which involves electromagnetic radiation and results in the emission of a γ photon or internal conversion (the electromagnetic energy is transferred directly to an orbital electron ejecting it from the atom). In the case that the isomer decays via gamma emission, based on whether an electric or magnetic operator is involved, the γ-photon is described as E1, E2,...Ex or M1,M2,...Mx. The number next to the letter represents the multipolarity of the photon or, in other words, quantifies the angular momentum carried away by the photon [22].

1.2.1.1 Caesium (Cs) isotopes

In this thesis, we will focus on the laser cooling and trapping of isotopes (both stable and radioactive) and isomers of caesium (Cs). Caesium, $_{55}$Cs, is an alkali metal with atomic number Z=55 and electron configuration: $1s^2 2s^2 2p^6 3s^2 3p^6 3d^{10} 4s^2 4p^6 4d^{10} 5s^2 5p^6 6s^1$ or [Xe]$6s^1$. Cs has a melting point at 28.5 °C and very high reaction rate with water (including the humidity in the air). The rest of the elements in the *alkali metals* group are: lithium ($_3$Li), sodium ($_{11}$Na), potassium ($_{19}$K), rubidium ($_{37}$Rb) and francium ($_{87}$Fr). Alkali metals have only one electron in their outermost shell (valence electron), which makes easier the formation of cations (positively-charged ions). In addition, the simple electronic structure (similar to hydrogen) played an important role, together with the availability of suitable wavelength laser sources, in the alkali metals being the first atomic species to be laser cooled and trapped in a MOT (further information in Section 1.2.3). There is only one

stable Cs isotope with N=79 (therefore A=133), and 39, to this date, discovered radioisotopes. In Fig.1.1, the neutron number and the half-lives of 7 neutron-rich Cs isotopes and 4 of their isomers are shown together with the stable ^{133}Cs.

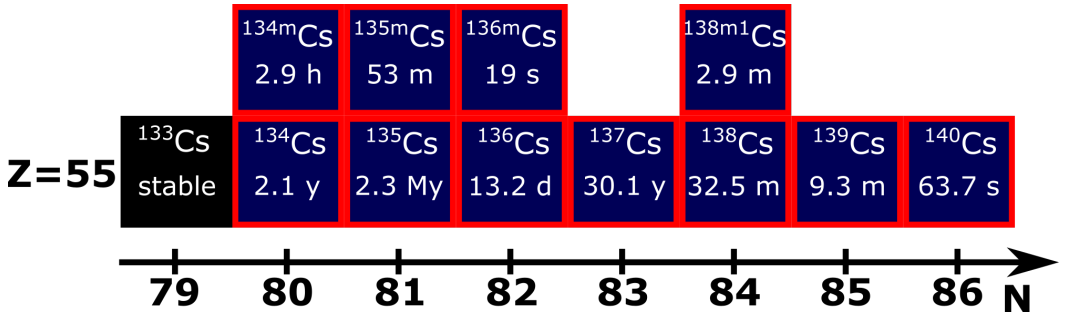

Figure 1.1: Isotopes and isomers of Z=55 (Cs), 79≤N≤86 and half-lives $T_{1/2}$ ≥19 s. The half-lives (with one decimal precision) are reported under each neutron-rich isotope (retrieved from [23], citing various sources).

It must be noted that changes in the nuclei's constituents, for example the addition of a neutron (i.e. different isotope) or the excitation of nucleon(s) to an isomeric state, also induce changes in the spectroscopic signature of each isotope by affecting the way the valence electron(s) interacts with the nucleus. This is translated in different hyperfine structure, but also a different (larger or smaller) energy difference between the ground and the fine-structure components of the excited state, described as isotope or isomer shifts. The fine and hyperfine structure in alkalis are introduced, together with the definitions of isotope and isomer shifts, in the following section.

1.2.2 Alkalis: structures and frequency shifts

The term "structure" is used in the field of spectroscopy to describe the arrangement of spectral lines as seen under high resolution. In turn, that structure was characterised as fine or hyperfine depending on the level of resolution (e.g. the resolution of a spectrograph) necessary to identify its characteristics [24]. Particularly, the fine structure (fs) in alkalis refers to the splitting of the electronic levels due to the coupling of the outer electron's angular momentum, **L**, with its spin's angular momentum, **S**. The products of the splitting, caused by the spin-orbit or **L-S** coupling, are electronic levels described by the total electron angular momentum quantum number, **J**:

$$\mathbf{J} = \mathbf{L} + \mathbf{S}. \tag{1.1}$$

Using Eq. 1.1 and taking into account all the possible combinations of **S** and **L**, the values of **J** lie in the range:

$$|L - S| \leq J \leq L + S. \tag{1.2}$$

A characteristic example of fine structure can be found in the first excited state of Cs, 6^2P. The state has L =1, indicated by the letter P, S =1/2, given in the superscript based on the formula 2S+1, and it is split in two components. The two components (or equivalently the fine-structure doublet) comprise the states $6^2P_{1/2}$ and $6^2P_{3/2}$, which are separated by a frequency $\approx h\cdot$16.6 THz. The subscript represents the J value as it is given from Eq. 1.2. The ground state of Cs, $6^2S_{1/2}$, does not have any fine-structure splitting because L =0 (indicated by the letter S), thus again based on Eq. 1.2, this gives only one possible state with J =1/2. The transition from the ground state $6^2S_{1/2}$ to the excited state $6^2P_{1/2}$ or equivalent $6^2S_{1/2} \rightarrow 6^2P_{1/2}$ is the D_1 line, and the $6^2S_{1/2} \rightarrow 6^2P_{3/2}$ is the D_2 line. The importance of the fine-structure doublet of Cs in the laser cooling context, particularly of the D_2 line for this experiment, will become more clear in the next Section 1.2.3.

The fine-structure states, in this case of alkalis, are further split due to the interaction of the electron's total angular momentum, **J**, with the nucleus's angular momentum, **I**. The hyperfine structure (hfs) levels are described by the total atomic angular momentum quantum number, **F**:

$$\mathbf{F} = \mathbf{J} + \mathbf{I}, \tag{1.3}$$

with values in the range:

$$|J - I| \leq F \leq J + I. \tag{1.4}$$

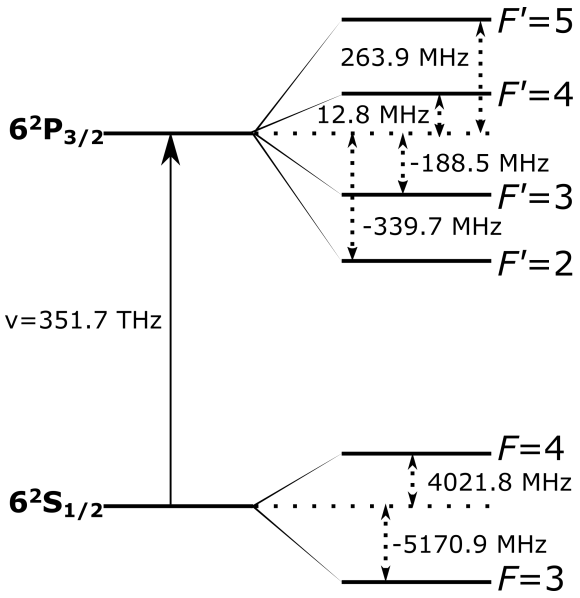

Figure 1.2: The hfs of the D_2 transition of ^{133}Cs. The frequency shifts of the hfs components with respect to the fs component are shown with one decimal precision and their values are reported in Chapter 4, Table 4.1. The frequency shifts are also reported in [25]. The diagram is -not- to scale (i.e. the distance ratio between levels does not represent the ratio of their frequency intervals).

In contrast to the fs case, the hfs is present also in the ground state, since the total angular momentum, J, is not zero ($S = 1/2$ regardless the electronic state). Using the same example, the ground state $6^2S_{1/2}$ of ^{133}Cs, with I =7/2, is split (based on Eq. 1.4) into the $6^2S_{1/2}F$ =3 and $6^2S_{1/2}F$ =4 states. The first excited state (D_1) is split into the $6^2P_{1/2}F$ =3 and $6^2P_{1/2}F$ =4, while the D_2 excited state into the $6^2P_{3/2}F$ =2, $6^2P_{3/2}F$ =3, $6^2P_{3/2}F$ =4 and the $6^2P_{3/2}F$ =5 states. The frequency differences between the hyperfine components lie in the range of ∼GHz, which is about 3 orders of magnitude smaller than the frequency differences present in the fine structure. This also justifies the etymology of their names since fine (for the THz) and hyperfine (for the GHz) resolution is needed to resolve them. In Fig. 1.2, the hfs of the D_2 line of ^{133}Cs is shown together with the frequency shifts of the hfs components. It is the first time that we need to specify the isotope of Cs (i.e. ^{133}Cs), and this is due to the hfs frequency shifts, in contrast to the fs shifts, varying for different isotopes (further discussed in Section 1.2.2.1).

1.2.2.1 Calculating the hfs frequency shifts

The hfs frequency shifts for each of the fine-structure components are calculated based on Eq. 1.5, as it is derived from the Hamiltonian describing the interaction of the outer electron with the nucleus (i.e. hfs Hamiltonian or H_{hfs}) considering J a good quantum number. For a detailed review on the calculation of the hfs frequency shifts of alkalis, including the theory behind, one can see [26].

$$\Delta E_{hfs} = \frac{1}{2} A_{hfs} K + B_{hfs} \frac{\frac{3}{2}K(K+1) - 2I(I+1)J(J+1)}{2I(2I-1)2J(2J-1)}, \tag{1.5}$$

where A_{hfs} is the magnetic dipole constant, B_{hfs} the electric quadrupole constant and $K = F(F+1) - I(I+1) - J(J+1)$. Eq. 1.5 can be also found in the literature with thee terms, when measurements of the magnetic octupole, C_{hfs}, are available. A representative example is found in Gerginov et al. [27] where, by measuring the hfs of the ^{133}Cs D_2 line with ≤2 kHz accuracy, the value of C_{hfs} was determined for the first time for a Cs isotope. The second and third terms require I, J ≥1 [26] (for M3 transitions, I, J ≥3/2), therefore apply only to the D_2 or D_1 excited states and not to the ground state where J =1/2.

Eq. 1.5 is used for calculating the hfs frequency shifts for all the alkali isotopes and isomers. The change in the interaction between the outer electron and the nucleus for different isotopes and isomers is “inserted” in Eq. 1.5 via the experimentally determined values for the A_{hfs}, B_{hfs} and I.

1.2.2.2 Isotope and isomer frequency shifts

The isotope and isomer shifts, normally denoted as $\delta\nu$, refer to the frequency shifts of the centre of gravity of the hfs. Specifically, for a transition between a high-energy state and a lower one with the hfs centre of gravity at a characteristic frequency ν, the isotope/isomer frequency shifts for two different isotopes/isomers, denoted as *A* and *B*, is defined as:

$$\delta\nu^{AB} = \nu^{A} - \nu^{B}. \tag{1.6}$$

The most important factor behind those shifts for heavy nuclei has been concluded to be the size of the nucleus's charge density distribution arising from the fact that the charge is distributed in a finite volume [28]. The addition (or removal) of a neutron or the excitation to an isomeric state changes the radius or/and the shape of the nucleus's charge, thus affecting the electronic energy levels. Other factors, such as the mass shift contribution, are becoming important to the isotope shifts of lighter elements (e.g. Na), where the relative change of the nucleus's mass by the addition of a neutron can be significant. For a detailed overview regarding isotope and isomer shifts and generally spectroscopic approaches for the determination of nuclear properties, one can see [29].

The shifts have to be taken into account, together with the differences in each of the hfs components, when one is tuning the lasers for trapping different isotopes or isomers. Examples can be found in Chapter 4, Sections 4.2.1 and 4.2.2, where the lasers are tuned for trapping different Cs isotopes. Due to the variances in the hfs of different isotopes/isomers, the MOT offers high selectivity, especially since the matching of two frequencies (repumper and cooling transitions) is required to successfully trap them. At this point, it will be useful for the reader to have an introduction to the basic concepts behind laser cooling and magneto-optical trapping.

1.2.3 Laser cooling and trapping of neutral atoms

1.2.3.1 History

The first theoretical approaches describing how lasers, and specifically resonance or near-resonance electromagnetic radiation, can be used for cooling and/or trapping neutral atoms were published nearly four decades ago [30] [31] [32]. In the following years, various pioneering groups further developed the original idea, overcame problems, and successfully used lasers for decelerating, cooling, and trapping neutral atoms. Phillips et al. [33], in 1982, published results from the deceleration of sodium (Na) atomic beams -a technique

known as the Zeeman slower-. Chu et al. [34], in 1985, reported on the cooling and confining of Na atoms using a technique called “optical molasses” (OM), with atomic temperatures T≈240 μK and holding times ∼0.1 s. Raab et al. [35], in 1987, demonstrated the first trapping of neutral atoms, holding Na atoms for 2 min at T≈600 μK in a spontaneous-light-force trap, which is now known as a magneto-optical trap (MOT). The first experimental observation of Na gas cooled down to T≈40 μK, a temperature about 6 times below the theoretical limit (Doppler limit-T_D =240 μK for Na), using OM took place in 1988 by Lett et al. [36]. One year later, the theoretical explanation of how the OM can achieve temperatures below the Doppler limit was published by Dalibard and Cohen-Tannoudji [37]. Steven Chu, Claude Cohen-Tannoudji and William D. Phillips won the 1997 Nobel Prize in Physics for developing methods for laser cooling and trapping neutral atoms.

Further developments in the field of laser cooling and trapping of neutral atoms followed, resulting in a systematic decrease of the minimum temperatures, increase in the control over the atoms and subsequently a deeper understanding of the phenomena involved. One of the most important milestones was the realisation of the first Bose-Einstein condensate (BEC) in alkalis, in 1995, using evaporation cooling of magnetically trapped rubidium (^{87}Rb) gas [38]. Very recently, ^{87}Rb BEC was realised only by laser cooling techniques, and specifically using Raman sideband cooling in a three-dimensional optical lattice with minimum losses [9]. More information on the progress of laser cooling over the years can be found in [39], [40] and other works not cited here. In these days, the cold atoms are at the centre of a new generation of quantum-based technologies, including high-precision atomic clocks [41], gravimeters [42] and magnetometers [43].

1.2.3.2 Basic concepts: two-level atom in optical molasses (OM)

The basic idea behind the cooling of atoms using lasers is the exploitation of the momentum-transfer, by resonant or near-resonant radiation during the light-atom interaction. When a resonant photon is absorbed, the atom is excited to a higher-energy atomic state, while its momentum changes by an amount equal to the photon’s momentum, $\hbar k$. After a characteristic time τ, the atom returns back to its ground state (de-excitation), and a photon is spontaneously emitted in a random direction inducing a momentum change in the atom of the same amplitude ($\hbar k$). The latter can be described also as a “recoil kick”. The average velocity of the atoms, caused by the recoil kicks, decreases to zero after many scattering events due to the random directionality of the phenomenon. Considering the latter, and by using radiation which opposes the atomic motion, the velocity of an atom with mass, m,

can be effectively decreased by $\hbar k/m$ in each scattering event.

For a moving atom, the Doppler effect shifts the absorption frequency. Accordingly, it was pointed out that detuned laser beams need to be used to effectively cool down atoms. When the atomic speed needs to be reduced in three dimensions (3D), six red-detuned laser beams have to be utilised in order to cover, on average, all the possible atomic trajectories. The above were taken into account and implemented during the first successful cooling and confinement of alkali atoms using the OM technique [34]. The velocity-dependent force applied on a two-level atom, in one dimension, placed in OM is given by:

$$\vec{F}_{molasses} \cong \frac{8\hbar k^2 \Delta (I/I_s)\vec{u}}{\Gamma(1+(I/I_s)+(2\Delta/\Gamma)^2)^2} = -\alpha\vec{u}, \tag{1.7}$$

where $\hbar$ the Planck's constant, I the laser's intensity, I_s the saturation intensity characteristic of the ground-excited state transition, Δ the laser's frequency detuning from resonance, Γ the transition's natural linewidth, α the damping coefficient and $\vec{u}$ the atomic velocity. The exact steps for the derivation of Eq. 1.7 can be found in many text books, including [39], [40].

The theoretical minimum temperature produced in OM is given by:

$$T_D = \frac{\hbar\Gamma}{2k_B}. \tag{1.8}$$

This temperature limit arises from the fact that while the atomic velocity averages to zero, the mean squared velocity is non-zero. The atom performs a random walk in the momentum space due to the recoil kicks of spontaneous emission events, a process that can be described as diffusive heating [39]. The Doppler temperature, T_D, is the temperature that is acquired at the point where the heating and cooling effects are balanced.

Nevertheless, as it was stated in the beginning, this description is strictly speaking correct only for an ideal two-level atom. Therefore, it is an over-simplification of the case of alkalis in the presence of hfs. Surprisingly enough, this complication offers important benefits in the real world since temperatures much lower than the Doppler limit, and close to the recoil limit, are observed with OM. The recoil limit, $T_r = (\hbar k)^2/2k_B m$, is equivalent to a few times the recoil energy. The theoretical explanation of the sub-Doppler temperatures present in OM experiments was provided by Dalibard et al. [37] (also see Chapter 2, Section 2.4.2.0.1).

When OM is combined with a quadrupole magnetic field, the force felt by the atoms becomes position dependent, additionally to the dependence on speed, resulting in their trapping. The hybrid technique is called magneto-optical trap (MOT), and it is analysed in detail in the next section.

1.2.3.3 Magneto-optical trap (MOT)

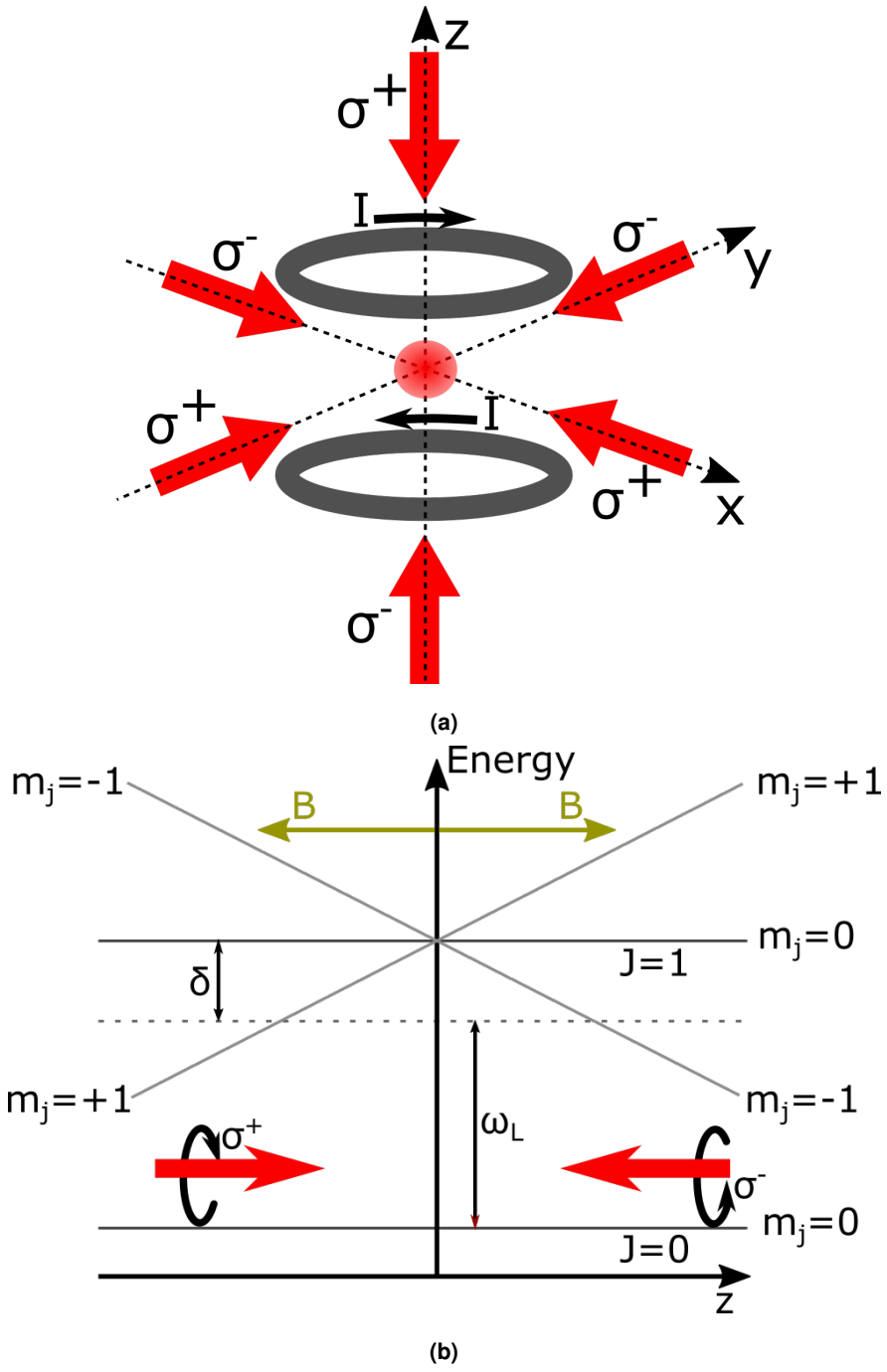

Figure 1.3: Magneto-optical trap (MOT). Bottom: MOT mechanism shown for a two-level atom. Top: MOT achieved from three orthogonal pairs of red-detuned laser beams combined with a magnetic field gradient produced by two coils in an anti-Helmholtz configuration. The circularly polarised beams that drive the $\sigma^{\pm}$ (with $\Delta m_j = \pm 1$) transitions are labelled as $\sigma^{\pm}$, while the black arrows indicate the direction of the coils' currents.

A 3D MOT configuration consists of six laser beams in a crossed-beam configuration

(Fig. 1.3a) and a magnetic field gradient produced from two anti-Helmholtz coils. Each pair of counter-propagating beams has circular polarisation of the same handedness, but since they propagate in opposite directions, they have opposite effects on the atom's angular momentum. The beams that drive the transitions with $\Delta m_j = +1$ are labelled as σ^+ and as σ^- the beams driving the transition with $\Delta m_j = -1$. The beams are red-detuned from the cooling transition. For Cs, the amount of detuning is about two times the natural line-width, but that depends strongly on the experimental conditions.

The red-detuning of the beam is essential for cooling, since only moving atoms will interact with the counter-propagating beam due to the Doppler shift, while atoms with "zero" speed (trapped atoms) will feel no force (the same applies for atoms moving in the same direction as the laser beam). In order to ensure that the atoms will continuously interact with the cooling laser and not be optically pumped to a "dark" state, repumper laser beams are completely overlapped with the six cooling-beams. The atoms are confined in the crossing point of the beams, however this confinement can only last for a few seconds (for a beam of 1 cm diameter [39]). The addition of a quadrupole magnetic field gradient causes an imbalance in the scattering force felt by the atoms resulting in their trapping. The magnetic gradient at the middle point of the coils, which is the crossing point of the cooling beams, is zero since the coils have currents of opposite directions.

For simplicity, we take into consideration a two-level atom, with a ground state J =0 and an excited state J =1, connected by an optical transition, in 1 dimension along z. If a magnetic quadrupole field is applied to the atoms, a linear gradient with 0 offset (i.e. the magnetic field at z=0 is 0) is produced, as sketched in Fig. 1.3b. As a consequence, the Zeeman splitting produces three sub-levels in the excited state ($M_J = -1, 0, +1$), whose energy varies linearly with z. As it can be seen from the figure, this has two effects: i) the resonance with the circularly polarised ($\sigma^{\pm}$) laser light varies with the position of the atom along z, and ii) the absorption probability in a given position is different for σ^+ or σ^- light. If the Doppler shift due to atomic motion is then added to the picture, one obtains a position-dependent scattering force, which pushes atoms towards the centre (z=0), plus a velocity-dependent viscous force produced by radiation pressure, which dissipates part of the atoms' kinetic energy. In detail, given a red-detuned laser frequency (ω_L in Fig. 1.3b) and atoms travelling towards $z > 0$, only the transition $\Delta M_J = -1$ would be close to resonance with the laser, and due to the selection rules this transition can only be driven by σ^- radiation. Considering the direction of the σ^- beam in the figure, the atoms would be pushed towards z=0. The same reasoning applies for atoms moving towards $z < 0$

and the σ^+ radiation. As a result, motion along $\pm z$ is effectively damped, and atoms are pushed towards the centre of the trap, where the minimum of the magnetic field gradient lies. By generalising the reasoning to 3D, one obtains a phenomenological explanation of the laser cooling and trapping in the 3-dimensional MOT.

The above method has been successfully applied to trap alkali and non-alkali atoms, and constitutes the workhorse trap in the majority of cold-atom experiments, from loading optical lattices to pre-cooling atoms to be used in an atomic fountain. MOT is implemented in our experiment both during the preliminary and the main experimental phases.

Chapter 2

First Phase: Offline set-up

The first experimental stage of my work was the realisation and full characterisation of a MOT of ^{133}Cs. The aim of this stage was to test and validate the trapping and diagnostic systems, thus including lasers, optics, vacuum, imaging systems just to name a few components. In addition, this work gave us the opportunity to test and further develop the software for controlling the experiment and characterising the MOT. The data from the characterisation of the MOT are included in this chapter. An important part of this work was achieved in collaboration with Dr. Luca Marmugi and Mr. Tanapoom Poomaradee.

2.1 Experimental set-up

In this section, I report on the details of the laser system, the vacuum system, and the other parts of the experimental set-up. The MOT system (including optics, coils and vacuum chamber) has been designed and installed directly at our laboratory in the University of Jyväskylä, while the laser system had been already designed, prior to the initiation of this experiment, at the UCL laboratories. Nevertheless, modifications and upgrades were necessary to adapt the laser system to the new conditions in Finland. More specifically, space constraints, lack of environmental control and a noisier environment (both electronically and mechanically) required modifications of the original design.

2.1.1 Laser system

In its final form, which was assembled in Jyväskylä during my activity, our laser system consists of two commercially available Radiant Dyes NarrowDiode external cavity diode lasers (ECDL). Longitudinal single-mode operation is achieved with the use of low loss built-in interference filters. The first laser is the cooling laser, which cools down the atoms in order to be captured in a MOT. The cooling laser is red-detuned from the transition of the

ground state of ^{133}Cs $6^2S_{1/2}$ F =4 to the excited state $6^2P_{3/2}$ F' =5. As typical of laser cooling experiments, this transition has been chosen because the atom can decay - with high probability - back to the initial ground state F =4. An atom however can also decay to the F =3 level. In this case, a second radiation - resonant with the F =3 to F' =4 transition, the repumper - ensures that it re-enters the excitation cycle of the cooling laser creating a closed-loop, which ensures the efficient cooling of the atom. The laser beams are manipulated and conditioned with optics (e.g. mirrors, polarising beam splitters etc.), acoustic optical modulators and locking techniques, which offer the necessary tuning and stabilisation of their frequencies.

2.1.1.1 Cooling laser configuration

The configuration used for tuning and stabilising the light from the cooling laser (see Fig. 2.1) can be separated into three main parts: detuning, locking, and amplification.

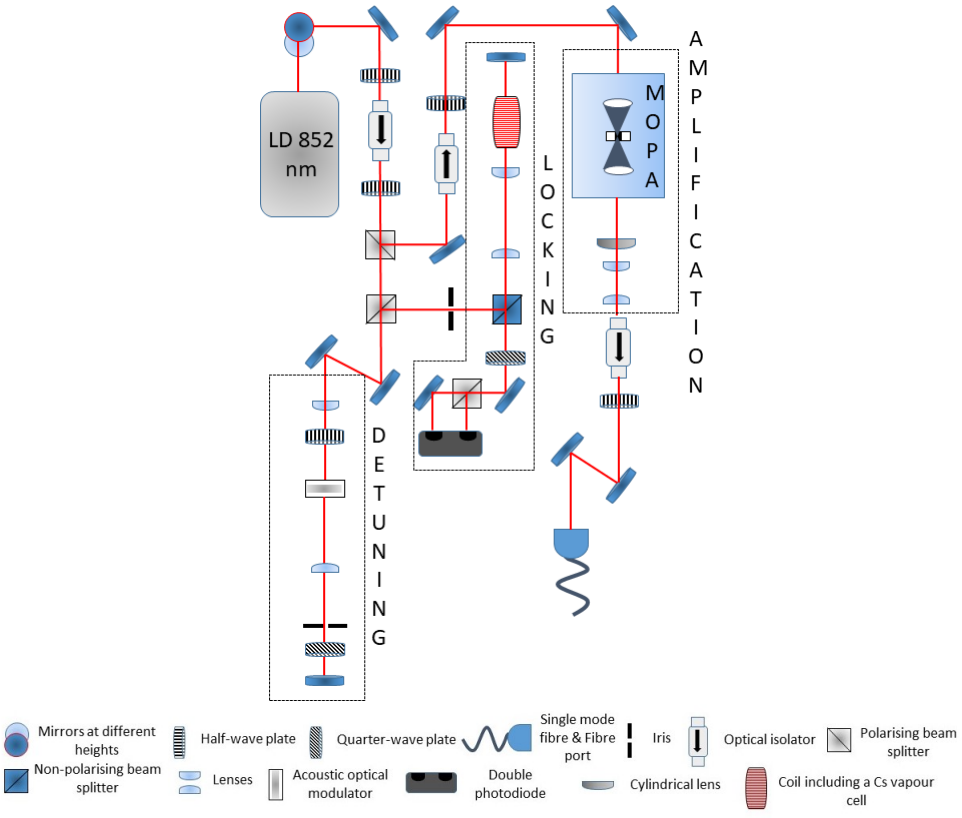

Figure 2.1: Experimental arrangement for the generation and control of the cooling light.

The emission of the cooling laser is split, sending ∼23 mW to the amplification section and ∼5 mW to the detuning and locking parts. The detuning part is mainly a 110 MHz AOM in a double-pass configuration, setting the desired frequency which is then passed to the locking part, where a Dichroic Atomic Vapour Laser Lock (DAVLL) system [44] is

implemented. The cooling light needs to be slightly (a few natural linewidths) red-detuned with respect to the $6^2S_{1/2}$ F =4 to the $6^2P_{3/2}$ F' =5 transition for cooling the ^{133}Cs atoms. However, we cannot lock on this transition due to its relatively small absorption peak, i.e. small DAVLL capture range. The double-pass AOM is therefore used to tune the light to the $6^2S_{1/2}$ F =4 to the $6^2P_{3/2}F'$ =4,5 crossover transition, which is ∼3 times larger than the F =4 to F' =5 peak. The extra detuning is compensated by an 80 MHz AOM placed on the MOT table. In addition, by using a double-pass AOM, we can tune the laser with higher accuracy and also sweep its frequency, as demonstrated in the following. We note that the double-pass configuration allows us to eliminate the misalignment due to changes in the AOM's driving frequency. Finally, the part of the laser light which has gone to the amplification stage, is amplified by a Master Oscillator Power Amplifier (MOPA) based on a tapered amplifier (m2k TA 0850 2000), producing a power output ∼1 W. The output of the MOPA is injected to the single-mode polarisation maintaining optical fibre to be transferred to the MOT configuration.

2.1.1.2 Repumper laser configuration

Analogous to the cooling laser, the repumper's configuration includes a locking section, while it does not require detuning nor amplification parts (see Fig. 2.2).

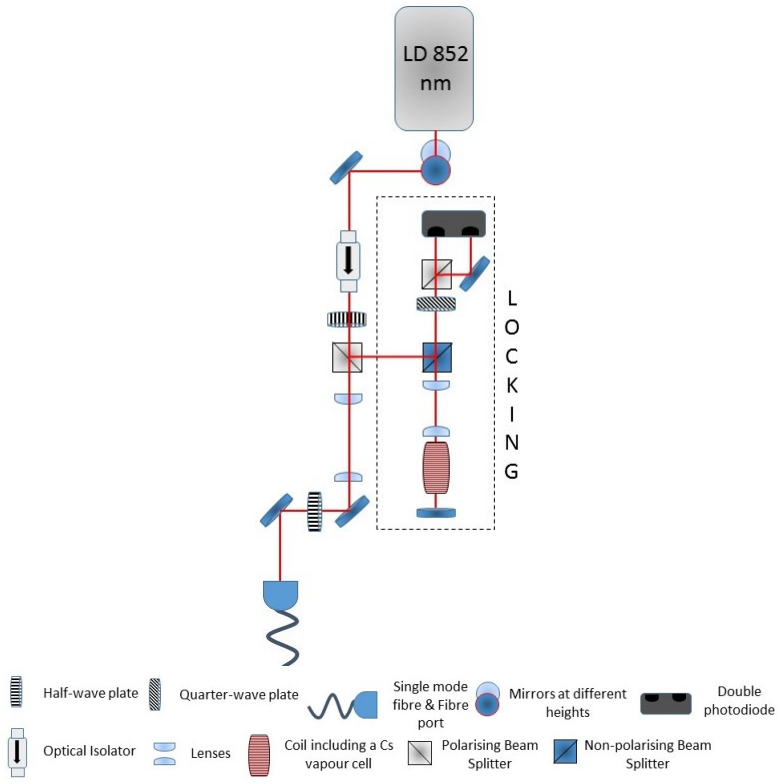

Figure 2.2: Experimental arrangement for the generation and control of the repumper light.

The repumper's laser beam is split into the locking part ($\sim$300 μW), and the remaining power ($\sim$50 mW) is injected to the single-mode polarisation-maintaining optical fibre to be transferred to the MOT configuration. The laser is locked to the F =3 to the F' =4 transition (via DAVLL), which offers sufficient capture range.

2.1.2 MOT configuration

The cooling and repumper beams are transferred to the MOT optical table via single-mode polarisation maintaining optical fibres. After the light arrives on the optical table, the configuration shown in Fig. 2.3a is used to create the conditions for a MOT. The cooling beam (red line) is first separated into two beams: the imaging and trapping beams. The imaging beam is red-detuned by an AOM in order to be on resonance with the cooling transition, F =4 to the F' =5 (see Section 2.2). The trapping beam is red-detuned by another AOM in order to be close to resonance with the cooling transition (described in Section 2.1.1.1). The repumper beam (blue line) eventually follows the same path as the trapping beam towards the trapping area.

Finally, the beams arrive at the science chamber (see Fig. 2.3b), where they form the trapping region. The imaging beam comes orthogonally to the trapping region (i.e. MOT's position), interacts with the atomic cloud, and the information passes through the system of mirrors and lenses to the CCD camera. For the realisation of the trap, coils in an anti-Helmholtz configuration were installed. In addition, three pairs of compensation coils are adjusted so to cancel any background magnetic field (e.g. strong magnet for mass-separation a few metres far from the science chamber).

2.1.2.1 Helmholtz and anti-Helmholtz coils

In this section, I report on the building and testing of the anti-Helmholtz coils, which will produce the magnetic field gradient required for the MOT. The coils' mount was designed in order to allow the addition of another coaxial set of coils to operate in the Helmholtz configuration. The Helmholtz coils were built and tested in order to investigate Feshbach resonances in a later stage of the experiment. Feshbach resonances occur when a molecular bound state approaches energetically the scattering state, affecting the collision cross-section of the atoms. In the case that these two states have different magnetic moments, a bias magnetic field (such as the magnetic field produced from Helmholtz coils) can be used to tune the energy levels, achieving resonant coupling or a Feshbach resonance between the two states [45]. The tunable collision properties with the use of a bias magnetic

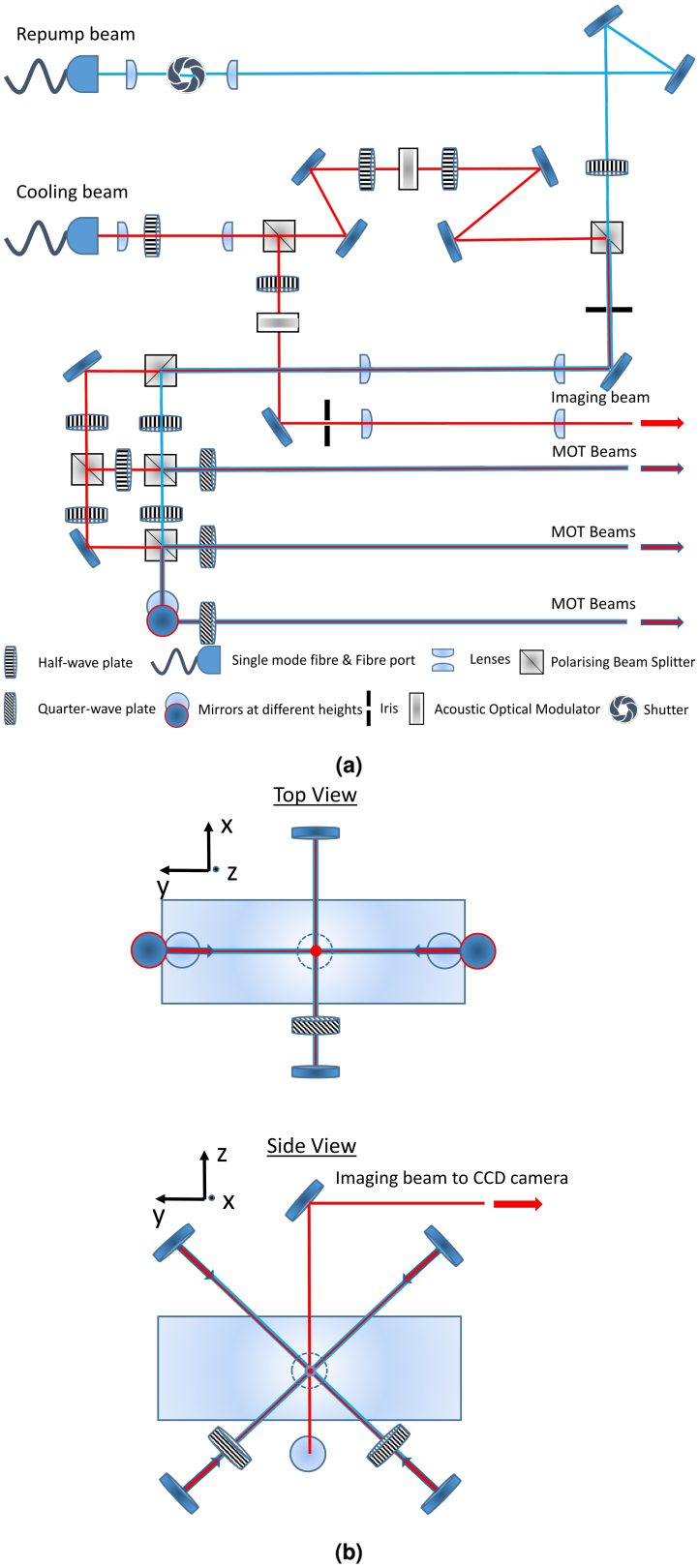

Figure 2.3: Magneto-optical trap configuration. (a) Optical configuration for achieving a single MOT. (b) Science chamber and six beams (blue-red lines) creating the trapping area. The single red line represents the imaging beam passing through the atomic cloud towards the CCD camera.

field can be used for increasing or decreasing the losses in ultracold gases (e.g. atoms in a dipole trap). For ^{133}Cs, two resonances have been identified at 17 and 48 Gauss [46]. Considering that the ^{135m}Cs is likely to exhibit resonances at similar values, and that our Helmholtz coils have the capability of reaching magnetic fields of more than 90 Gauss, it will be possible to use the coils for exploitation of Feshbach resonances during the ^{135m}Cs BEC experimental phase.

The design and simulations of the two sets of coils were realised by Conor Bradley [47]. The design of the mount was produced in the 3D Inventor CAD software, and the specifications (e.g. type of wire, coils' diameter etc.) in order to achieve the necessary quadrupole and bias fields were calculated and simulated with COMSOL Multiphysics. The anti-Helmholtz coils were utilised only during this experimental phase. The two configurations are described below.

2.1.2.1.1 Realisation of the coils Based on the 3D design (see Fig. 2.4), the UCL MAPS workshop built the coils' mounts, while winding and testing were realised during my first year activity. The anti-Helmholtz and Helmholtz coils have 48 turns and internal diameters of 27 and 100 mm respectively. Adjustments to the width of the coils' mounts were necessary in order to account for the insulation layer of the wire.

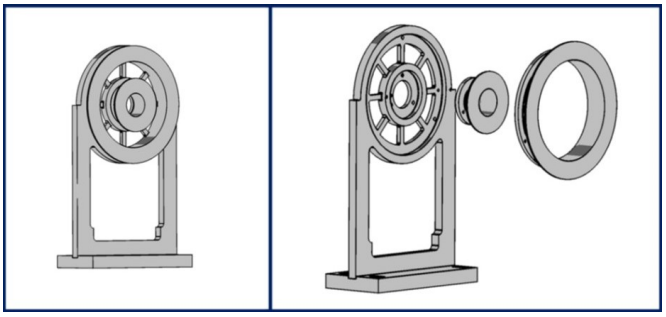

Figure 2.4: The ring with the smallest diameter is the mount for the anti-Helmholtz coils, while the bigger one was used for the Helmholtz (Feshbach) coils. Both of the constituents are screwed onto the holding plate. Image from [47].

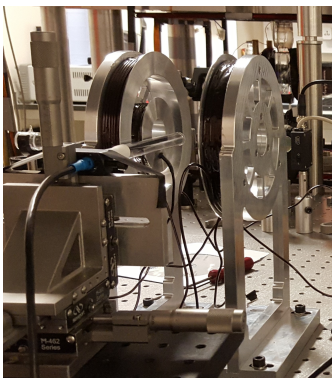

Figure 2.5: Picture of the coils during the magnetic field measurements using the Tesla Meter 5170.

2.1.2.1.2 Coils testing The bias magnetic fields and gradients produced by the two pair of coils were measured along the coils' main axis. The centre-to-centre distance was chosen to be 80 mm, which is the minimum distance the coils can have as imposed by the science chamber's width. It has to be noted that the simulations and design were done

for a different science chamber, where the actual centre-to-centre distance was smaller, thus realising the proper Helmholtz (anti-Helmholtz) configuration. Therefore, one expects some deviation from the simulation values in the current configuration.

The measurements of the magnetic field were realised with a Tesla Meter 5170 Hall probe. The probe was mounted on a ThorLabs translational stage (see Fig. 2.5) providing us with the ability to measure the magnetic field, with a precision of 10 μm, up to 15 mm far from the centre of the two-coils configuration. An HP 6256B DC power supply, in constant-current mode, was used to supply current to the two sets of coils.

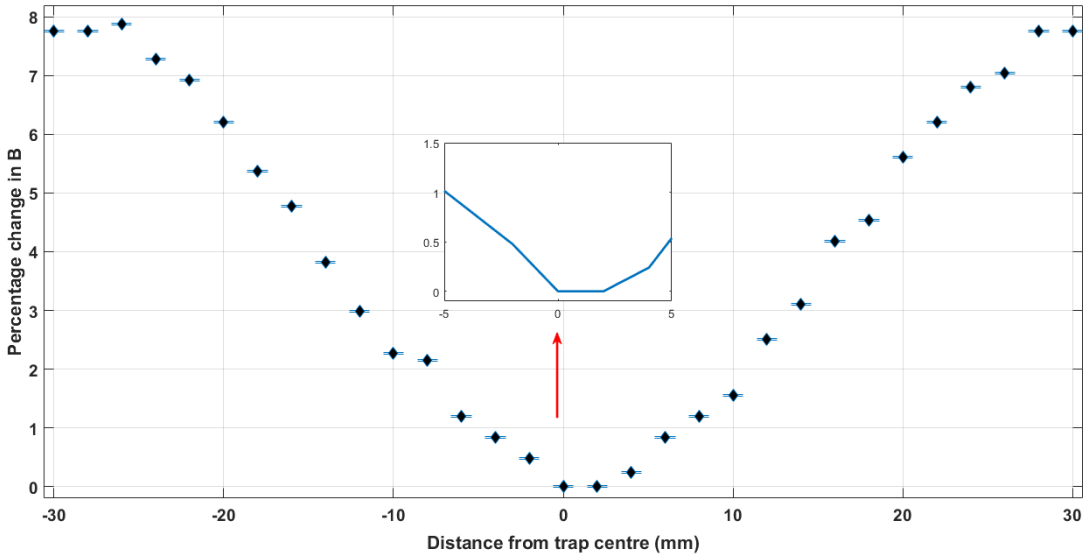

Figure 2.6: Percentage change of the bias field, B, along the coaxial axis produced from the Helmholtz coils for a centre-to-centre distance of 80 mm and 15 A supplied current. Inset: showing the variation of the magnetic field for $\pm$5 mm from the centre of the configuration.

Figure 2.6 shows the percentage change of the bias field along the coaxial axis produced from the Helmholtz (Feshbach) coils. By increasing the centre-to-centre distance to 80 mm and keeping the diameter the same, i.e. 100 mm, we deviated from the ideal Helmholtz configuration. This produces the degradation in the uniformity of the field along the coaxial axis observed in Fig. 2.6. An ideal Helmholtz configuration would require a centre-to-centre distance equal to the radius of the coils, in our case 50 mm. The maximum field value at the centre was measured to be 84(1) G, with less than 1% deviation from the central value. The sufficiently high and approximately uniform field means that we can still explore the Feshbach resonances. However, it is possible that for the main experiment we are going to use a smaller chamber or design a new set of Feshbach coils. In Fig. 2.7, the magnetic field along the coaxial axis is shown for the anti-Helmholtz configuration, with the gradient at the area of interest, at 15 A, being 26.2(1) G/cm or 1.747(7) G/cm/A

for any current.

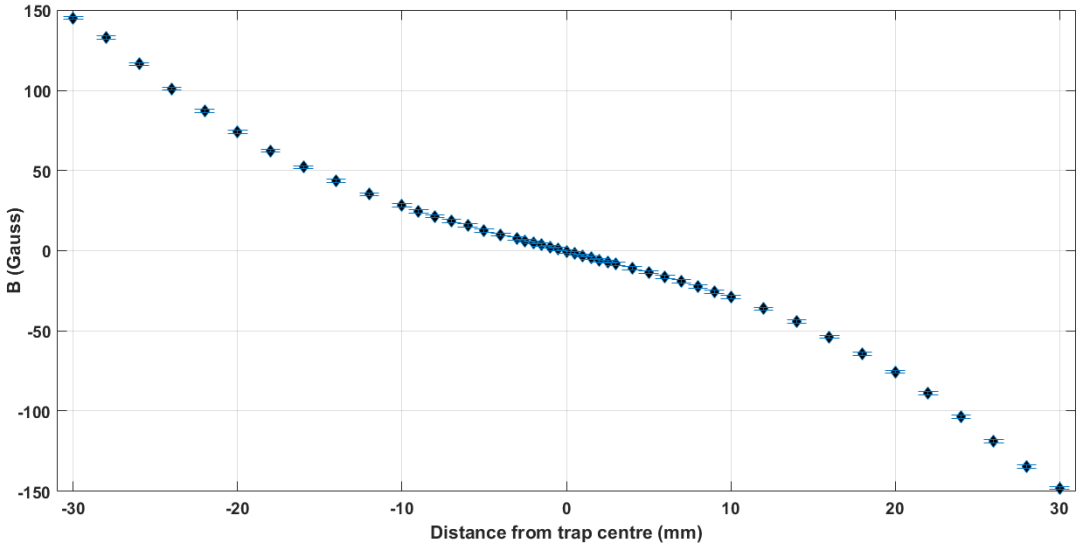

Figure 2.7: The magnetic field along the coaxial axis produced from the anti-Helmholtz coils for a centre-to-centre distance of 80 mm and supplied current of 15 A.

2.1.2.2 Preparation and realisation of the vacuum system

In this section, the preparation and realisation of a high-vacuum system for the purposes of the first preliminary experiment is reported. The vacuum system consists of CF40 and CF16 non-magnetic stainless steel parts, one CF40 and one CF16 manual operated valves, one Pyrex chamber (science chamber) and a Varian Starcell 20 l/s ion pump (see Fig. 2.8). The preparation was divided in three parts: cleaning, baking in the oven and baking with heating tapes after initial vacuum conditions had been established.

Following the cleaning and baking (in an evacuated oven), the system was assembled in the shape illustrated in Fig. 2.8. The pressure went down to 10^{-5} mbar using a combination of a turbo and a scroll pump, and then our Starcell 20 l/s ion pump was initiated. The system was pumped for 48 hours reaching a baseline pressure of 10^{-7} mbar. Having achieved the base pressure, the outgasing phase began. During the latter, the system was wrapped with heating tapes and baked for 3 days at 125 °C. Finally, the heating tapes were turned off, and the turbo pump was isolated by closing the connecting valve. The ion pump took over, and after approximately 15 hours, a baseline pressure of 2.3×10^{-10} mbar was achieved.

The next step was to break the Cs ampoule placed in the CF16 blank tube (see Fig. 2.8 bottom right). The ampoule is an Alfa Aesar breakseal ampoule, including 1 g of ^{133}Cs with 99.8% purity. Prior to the assembling of the system, a small disc magnet (1 cm diameter

and 0.5 cm width) was placed inside the tube together with the ampoule. The magnet was rapidly moved using an external strong magnet resulting in the breaking of the ampoule.

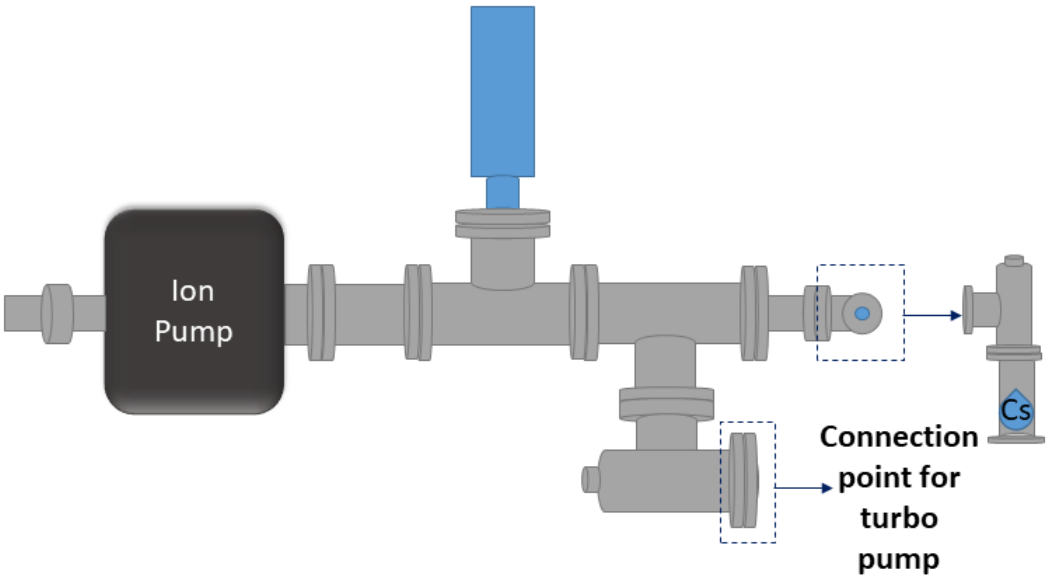

Figure 2.8: The top view of the vacuum system. Grey are the steel vacuum parts, and blue is the Pyrex science chamber.

2.2 Imaging system: absorption imaging

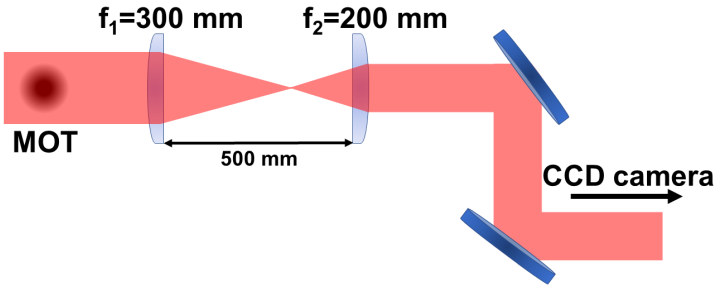

Figure 2.9: Basic schematic showing the main optics in the absorption imaging configuration. Two plano-convex lenses, with 300 mm and 200 mm focal length respectively, reduce the size of the imaging beam in order to match the sensors dimensions. The collimated beam is then directed to the Pixelfly USB CCD camera.

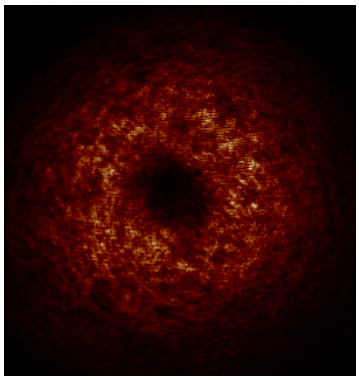

Figure 2.10: A probe beam of 10 mm diameter as detected by the CCD camera after passing through a MOT of ∼50 million atoms.

The imaging system is one of the most important parts of cold and ultracold atoms experiments, constituting the main way to characterise, optimise and analyse the atomic cloud. In this experimental phase, we have implemented absorption imaging, which relies

on a resonant (or slightly detuned) probe laser beam going through the atomic cloud and then into a CCD camera (see Fig. 2.9). The cold atoms absorb photons, therefore creating a position-dependent decrease of the beam intensity, which is mapped by the CCD camera. This can be qualitatively viewed as the atoms casting a "shadow", which is then imaged by the CCD (see Fig. 2.10). By measuring the variation of the probe beam intensities in the presence-absence of the atoms, one can extract the optical depth, which in turn can be used to calculate the number of atoms and the density distribution of the atomic cloud (see following sections).

The imaging system consists of a PixelFly USB 14 bit CCD camera, with resolution of 1392$\times$1040 pixels and sensor diagonal of 11.14 mm, controlled by a LabVIEW routine. The probe (imaging) beam is linearly polarised, and red-detuned from the $6^2\mathrm{S}_{1/2}$ $F=4$ to $6^2\mathrm{P}_{3/2}$ $F'=5$ transition by an amount ranging from 0Γ (resonance) to -0.75Γ, depending on the density of the cloud. For dense clouds, the detuning of the probe beam becomes essential for avoiding saturation effects. The detuning and the control of the imaging beam are achieved by an 80 MHz AOM (see Fig. 2.3a). Finally, the intensity of the beam is chosen to be $\sim$50 $\mu\mathrm{W/cm}^2$, which is well below the saturation level I_s =1.66 $\mathrm{mW/cm}^2$ for linearly polarized light resonant with the D_2 line [25].

2.2.1 MOT number of atoms

In order to determine the number of atoms in the MOT from an image analogous to the one in Fig. 2.10, the contribution of the atoms needs to be isolated. The latter can be achieved by recording three images under different conditions. The first one, in the next section referred to as MOT image, is similar to Fig. 2.10 and represents the atomic cloud as "seen" from the CCD camera. The second image (light image) is without the atomic cloud, acting as a laser light reference, and the third (dark image) is without any light nor atoms in order to establish the background of the measurement. The above procedure has to be repeated every time that information needs to be extracted.

The intensity profile of the first image (with the atoms) is represented in space as $I(x,y)$, the light reference image as $I_o(x,y)$ and the background image as $I_{bg}(x,y)$. By applying Beer's law the optical depth (OD) of the cloud can be calculated as:

$$OD(x,y) = \ln\left(\frac{I_o(x,y) - I_{bg}(x,y)}{I(x,y) - I_{bg}(x,y)}\right). \tag{2.1}$$

Using the value of the OD and for a probe beam with intensity below saturation, the atom

column density, $n(x, y)$, can be calculated as:

$$n(x, y) = \frac{OD(x, y)}{\sigma}, \tag{2.2}$$

where σ is the scattering cross-section expressed by:

$$\sigma = \frac{\sigma_o}{1 + 4\left(\frac{\Delta}{\Gamma}\right)^2 + \frac{I}{I_s}}, \tag{2.3}$$

with σ_o being the scattering cross-section for resonant light, Δ and I the detuning and intensity of the probe beam respectively and I_s the saturation intensity. We note that σ is strongly dependent on the trapped species and the detuning of the probe beam.

Finally, the total number of atoms, N, is calculated by integrating the atom column density over space (x, y):

$$N = \frac{1}{\sigma} \int_{x_1}^{x_2} \int_{y_1}^{y_2} OD(x, y)\, dxdy, \tag{2.4}$$

where x_1, x_2, y_1, y_2 are the dimensions of the area of interest. $OD(x, y)$ varies with the pixel position, and the spatial coordinates are calculated by calibrating the pixel size of the CCD sensor.

2.2.2 MOT temperature, spatial and phase-space density

Assuming that the MOT behaves as a Boltzmann gas, the optical depth of the cloud will be accurately described by a Gaussian curve of the form:

$$F(x) = OD_{max} \exp\left(\frac{-(x - \mu)}{2\sigma^2}\right), \tag{2.5}$$

where OD_{max} is the maximum optical depth, μ is the centre of the distribution/cloud and σ is the cloud's radius. By fitting the calculated optical depth with Eq. 2.5, the above properties can be extracted and used for calculating the temperature, the density and phase-space density of the MOT. Since Eq. 2.5 describes a 1-D Gaussian, it needs to be fitted twice along orthogonal directions in order to acquire information for both x and y directions. For the purpose of this discussion and to avoid confusion, we are considering the properties of the cloud in the x direction only. Extension to the y direction can be easily obtained by replacing x and related parameters with the y-variable and parameters.

The temperature is measured with the standard method of Time-of-Flight (TOF), where the atomic cloud is left to expand freely by turning off the MOT beams and the magnetic field gradient, and images are taken for different TOF times. Fitting Eq. 2.5 gives the cloud's radius for each TOF, and by measuring the slope of the cloud's evolution, the temperature

of the cloud in one direction (e.g. x direction) can be calculated. The ballistic expansion of the cloud at any time is given by [48]:

$$\sigma_x(t)^2 = \sigma_{0,x}^2 + \frac{k_B T}{m} t^2, \tag{2.6}$$

where $\sigma_{0,x}$ is the radius of the cloud along the x axis at the beginning of the expansion, k_B the Boltzmann constant, T the temperature of the cloud and m the mass of the trapped species. When the above equation is solved for different TOF values, the temperature is calculated as:

$$T = \frac{m}{k_B} \frac{\sigma_x^2 - \sigma_{0,x}^2}{t^2 - t_0^2}, \tag{2.7}$$

with $t_0, \sigma_{0,x}$ being the initial and t, σ_x the final conditions.

The evolution of the cloud's radius, i.e. the graph of σ_x versus time for this case, can be also used for extrapolation to the beginning of the expansion. The calculated volume of the cloud at TOF=0 can be then used to find the density of the cloud before the expansion as:

$$n_0 = \frac{N}{V_0}, \tag{2.8}$$

providing us with the density of the MOT at TOF=0, assuming uniformity. The MOT volume at TOF=0, for a cloud with a Gaussian density profile, is given by:

$$V_0 = \sigma_{0,x}\sigma_{0,y}\sigma_{0,z}\pi^{\frac{3}{2}}, \tag{2.9}$$

where $\sigma_{0,x}$ and $\sigma_{0,y}$ are the extrapolated values of the cloud's radius on the x and y axis respectively, and $\sigma_{0,z}$ is considered to be approximately equal to the average of the $\sigma_{0,x}$ and $\sigma_{0,y}$. The approximation for the value of $\sigma_{0,z}$ is considered valid for low magnetic field gradients, and it was verified in our case by placing the CCD camera at different angles and verifying the circularity of the MOT.

The final stage of our calculations is the phase-space density, ϱ, which can be defined as the number of trapped atoms per cubic De Broglie wavelength, λ_{db}, expressed as:

$$\varrho = n\lambda_{db}^3. \tag{2.10}$$

This relation reveals the dependence of ϱ on the density, n, and the temperature of the atomic cloud. The latter dependence becomes apparent if one expresses λ_{db} as:

$$\lambda_{db} = \frac{h}{\sqrt{2\pi m k_B T}}, \tag{2.11}$$

where h is Planck's constant and m, k_B, T as defined in Eq. 2.7.

2.3 Controlling the experiment

Having established the methodology to characterise the MOT, the next step is to build the hardware and software controls to realise it.

2.3.1 Hardware controls

The hardware controls used during the first and the second experimental phase are standard for cold atoms experiments. In the present case, the experimental controls consist of: AOMs, mechanical shutters, a PID controller, a MOSFET and a Data Acquisition (DAQ) system. Figure 2.11 illustrates the basic idea for controlling our experiment.

A desktop computer was used to run the acquisition software and control a National Instruments 6009 USB DAQ board. The DAQ controls a homemade mechanical shutter for switching on/off the MOT beams, a 3080-110 Crystal Technology AOM for the imaging beam, and an SRS SIM960 Analog Proportional–Integral–Derivative controller (PID) combined with a Metal-Oxide-Semiconductor Field-Effect Transistor (MOSFET) IXFN 120N20 based system to regulate the current of the trapping coils. The voltage to the water-cooled MOSFET was supplied by an Agilent 6572 100 A DC supply. Finally, the 6009 USB controls the Pixelfly USB camera via the Pixelfly trigger box.

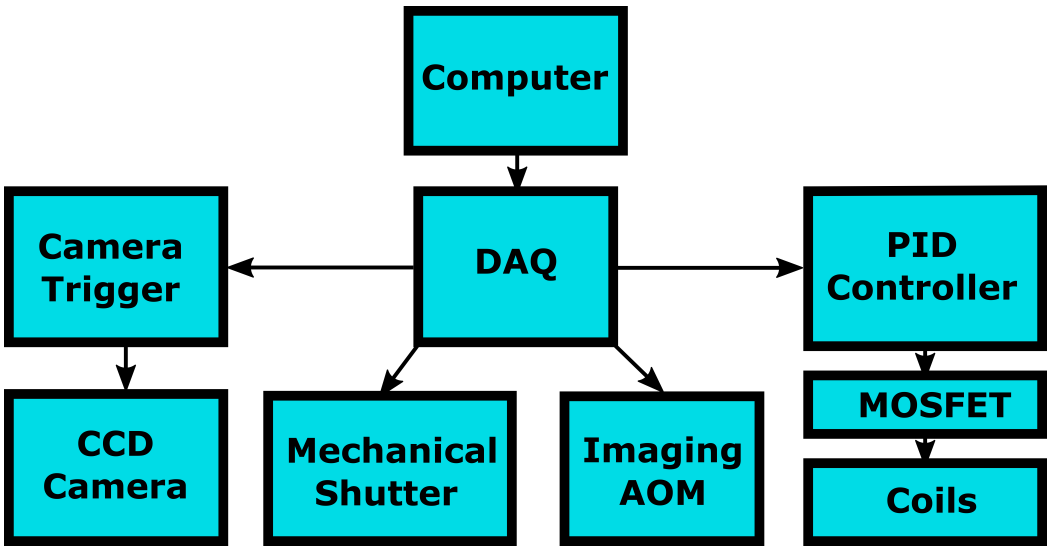

Figure 2.11: Schematic of the hardware controls.

2.3.2 Software controls

The programme for the experimental control was written in LabVIEW, which also allows an easy interface with different hardware. LabVIEW is used to realise the imaging se-

quence, control the hardware (camera, AOMs, shutters etc.), and to perform the numerical calculations needed to acquire the characteristic properties of the MOT (number of atoms, temperature, density and phase-space density).

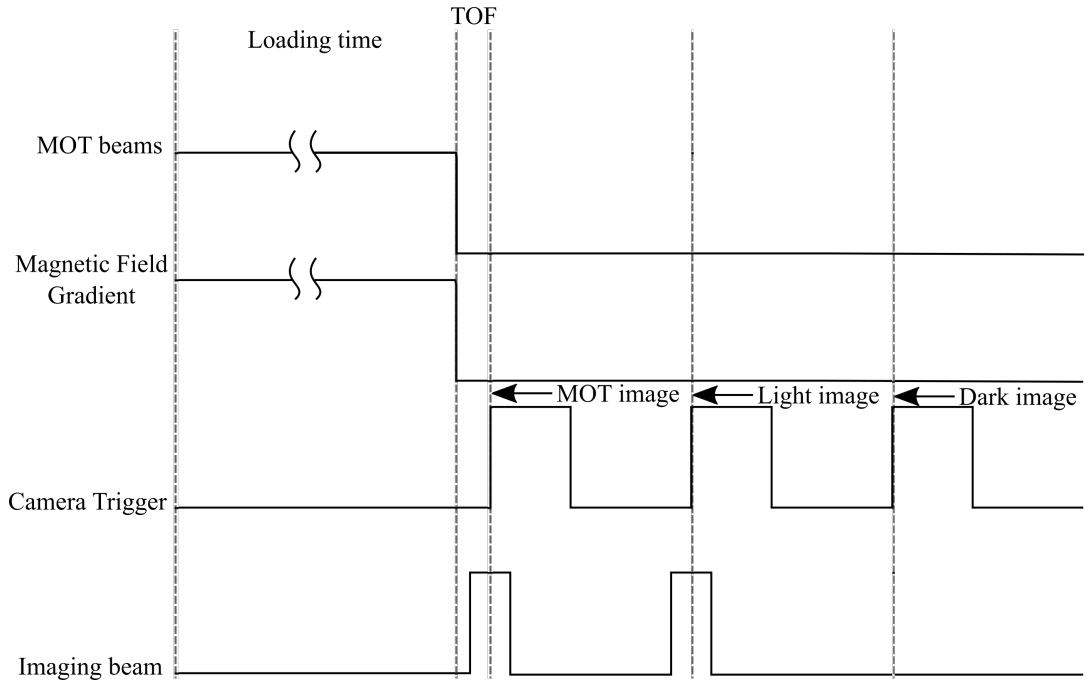

Figure 2.12: Timing sequence for imaging the MOT. The axes are not scaled.

Figure 2.12 shows the timing sequence used for acquiring the images needed for the characterisation of the MOT, starting from the loading phase. During the latter, the MOT beams together with the magnetic field gradient are on and atoms are loaded into the MOT. The loading time ranges between 1 to 10 seconds, depending on the measurement of interest. At the end of the loading time, the MOT beams and the magnetic field are turned off simultaneously, initiating the free expansion of the cloud (TOF). The TOF usually lasts from 1 to 10 ms, and at the end of it the CCD camera is triggered to record the MOT image. The camera has been set to acquire an image at the rising edge of the triggering squared pulse. The camera is triggered two more times for acquiring the light (laser light reference) and the dark (background) images. Before the MOT and light images are acquired, the imaging beam is turned on, while for the dark image everything is off (see section 2.2.1 for details on each imaging stage). Prior to the initiation of the data acquisition procedure, the synchronisation of the software was verified by directly comparing the timing of the generated signals.

While the hardware is initially synchronised through the software along the lines of Fig.

2.12, the final and most crucial synchronisation is the one done by observing directly the response of the hardware. For that purpose, two Thorlabs high-speed Si photodetectors (DET36A/M) were placed on the path of the MOT (cooling and repumper) and the imaging beams. The outputs of the two photodetectors were connected to an Agilent Technologies 4-channel oscilloscope (DSO-X 3104A, 1 GHz bandwidth). The other two input channels of the oscilloscope were connected to the output signal of the camera's trigger box and the output of the PID-MOSFET system. As result of this procedure, residual delays smaller than 50 μs were observed, and an overall synchronisation within 100 μs was obtained.

2.4 ^{133}Cs MOT characterisation

Following the realisation of a ^{133}Cs MOT and the development of the necessary controls, the next step is to fully characterise the atom trap. The characterisation of the MOT includes the measurement of the loading rate and lifetime for different experimental conditions. In addition, the temperature, the density and phase-space density of the MOT are calculated. The above properties are measured with absorption imaging as introduced in Section 2.2.

Analysis of the aforementioned dynamic properties is essential for optimising the trap and creating optimum conditions for the next steps (MOT from stable and radioactive ion beams, dipole trap and Bose-Einstein condensate) and future applications (high-precision spectroscopy, nuclear forensics, etc.).

2.4.1 Loading rate and lifetime

The number of atoms in a MOT changes dynamically, and it is determined by the balance between the loading rate (atoms loaded in the trap per unit time) and the loss rate (atoms escaping from the trap per unit time). The losses of the trap can be categorised as: single-body and two-body collision losses. Mathematically the rate of change of the number of trapped atoms can be described as:

$$\frac{\mathrm{d}N(t)}{\mathrm{d}t} = L - \gamma N(t) - \beta \int n(\mathbf{r},\mathbf{t})^2 \mathrm{d}^3 r, \tag{2.12}$$

where $N(t)$ (atoms) is the time-dependent number of trapped atoms, L (atoms·s^{-1}) is the loading rate of the trap with atoms from the background vapour, γ (s^{-1}) and β (cm^3/s) are the single-body and two-body collision loss rate coefficients respectively. Finally, $n(\mathbf{r},\mathbf{t})$ (cm^{-3}) is the MOT's density, which will be considered uniform and constant for each set of MOT parameters (intensity, detuning, magnetic field gradient) used in this work.

Loading rate, L: The loading or capture rate of a MOT can be defined as the number of atoms captured in the MOT per unit of time. The exact definition changes based on the source of atoms (e.g. dispenser, Zeeman slower, vapour etc.), but this work focuses on the loading rate of a Vapour Cell MOT (VCMOT). The parameters that affect L can be divided into: thermodynamic and atomic. The thermodynamic properties are the background density, the trapping volume and the average velocity of the untrapped atoms (background gas). The atomic properties are usually expressed via the capture velocity, u_c, and they are: the cooling intensity (I), the detuning (Δ) and the applied magnetic field gradient (B). The loading rate has been experimentally shown to increase with the capture velocity [49], where the latter is defined as the maximum velocity an atom can have and still be captured in a MOT.

Single-body collision rate coefficient, γ: is the loss rate due to collisions of the trapped cold atoms with the background (room temperature) gas atoms. The highly energetic atoms in the vicinity of the MOT are elastically colliding with the trapped cold atoms providing them with enough energy to escape the trap. Due to the nature of this loss process, variations in the density of the background gas (i.e. chamber pressure) have a strong impact. In addition, decreasing the trap's depth below a certain value also has a strong impact in the loss rate, since there will be a higher probability for the energy provided from elastic collisions to be sufficient for the atoms to overcome the trap's potential.

Two-body collision rate coefficient, β: is the loss rate due to collisions between cold trapped atoms, and it is dependent on the MOT density. The collisional processes that determine β are: Radiative Escape (RE), Fine-Structure changing (FS) and Hyperfine-Structure changing (HS) collisions [50] [51]. The last one can be ignored for our work because it becomes important only in very shallow traps, where the energy produced from hyperfine changes can be sufficient for the atoms to escape. The above collisional processes, involving ground state and excited atoms, are light-assisted and as expected, they present a strong dependence on the cooling intensity. Both processes have been described in [52].

There are three main regimes that a MOT can operate in: temperature-limited, constant density and "two component" [53], [54], [55], [56], [57]. The temperature-limited or constant-volume regime is usually present in traps with small number of atoms ($<10^4$), where inter-atoms interactions are essentially absent. The cloud's volume remains constant, and the density increases as more atoms are added. The regime is called temperature-limited because the volume depends only on the temperature of the MOT [57]. Sesko et

al. [58] showed that the maximum density of a MOT increases with the number of atoms until it enters a regime where it reaches a limit, and then remains constant while the cloud's volume increases. Such a regime is called density-limited and refers to traps with high number of atoms. Specifically for Cs, the density-limited regime has been observed for populations higher than 4-8$\times 10^4$ [59], 10^5 [55] and 10^6 atoms [57]. The existence of a maximum density is due to radiation trapping forces, defined as repulsive forces, $F \sim 1/r^2$, arising from photon multiple scattering involving excited and ground state atoms in the trap [50], [59]. For very large MOT populations ($\gg 10^6$ atoms [56]), the density becomes uniform. The last regime described here is the "two-component", where the density distribution has a very dense central region, and a low density surrounding ring extending to a large radius [57]. There is a fourth regime which concerns optically thick clouds, but it will not be discussed here.

In the context of this work, for loading times of up to 5 seconds and populations ranging between 10^7 to 10^8 atoms, it is considered that the constant density regime dominates. The above assumption is based on the number of atoms that we routinely trap and on the density of our cloud, which seems to remain around 1×10^{11} to 5×10^{11} atoms/cm^3 independently of the loading time.

Assuming a uniform density to simplify our calculations [60], [59], [61], Eq. 2.12 can be written as:

$$\frac{\mathrm{d}N(t)}{\mathrm{d}t} = L - (\gamma + \beta n_0)N(t). \tag{2.13}$$

By solving Eq. 2.13, we acquire an expression for the time-dependent MOT population:

$$N(t) = N_s(1 - e^{-(\gamma+\beta n_0)t}), \tag{2.14}$$

where $N_s = \frac{L}{\gamma+\beta n_0}$ is the steady state number of atoms in the MOT [62], which is achieved when the loading and loss rates are balanced. Eq. 2.14 can be used for calculating the loading rate and the lifetime of the MOT.

In the literature, the loss rate of MOTs of various alkali atoms is usually determined by saturating the MOT (i.e. reaching the steady state number), and then turning off the supply of atoms (examples: [62], [63], [64]). Looking at Eq. 2.13, one can see that for $L = 0$, the MOT population is described by:

$$N(t) = N_s e^{-(\gamma+\beta n_0)t}. \tag{2.15}$$

By fitting the exponential decay curve with Eq. 2.15, one can extract the loss coefficients when the MOT is operated in the constant density regime. Having extracted those coeffi-

cients, the lifetime of the trap is calculated as [65]:

$$\tau = \frac{1}{b} = \frac{1}{\gamma + \beta n_0}. \tag{2.16}$$

In our set-up, cutting-off the supply of atoms instantaneously is impossible since by using a reservoir as the atomic source, the cell is saturated with Cs vapour. In addition, the absence of anti-adsorption (or anti-relaxation) organic coating (e.g. PDMS), in this set-up, means that large number of atoms can be adsorbed in the Pyrex surface and operate as a continuous (although inefficient) supply of atoms by desorbing and contributing to the MOT population (a phenomenon observed in [65] as well). The above has been verified by keeping the reservoir isolated from the system for more than a month, while the MOT population remained in the order of 10^7 atoms. We note that this is a completely different phenomenon from what is observed during the presence of the PDMS coating (see Chapter 3, Section 3.3), where the majority of the atoms becomes immediately available for trapping, and adsorption/losses are minimised.

Nevertheless, various groups (examples: [66], [60], [67]) calculated the trap loss coefficients by using the loading curve of a MOT instead of its decay curve. By adopting a similar approach, one can calculate β and γ, and use them for calculating the trap's lifetime. In the following subsections, β and γ are calculated, while demonstrating the dependence of the two-body loss coefficient, β, on the cooling laser's intensity.

2.4.1.1 Loading rate and lifetime measurements

The experimental strategy for measuring the loading rate is as follows. As a first step, the MOT is loaded for different loading durations, and each time the number of trapped atoms is measured. The loading time is increased up to the point that saturation of the MOT is observed and the number of atoms stops increasing. After collecting the data, the number of atoms versus loading time is plotted (see Fig. 2.13).

The example in Fig. 2.13 is used to demonstrate the methodology behind the calculation of the loading rate. The information that can be extracted from the loading curve is the steady state number of trapped atoms, N_s, and the total loss rate $b = \gamma + \beta n_0$. The loading rate for this example then by definition can be calculated as: $L = N_s \cdot b$ =117(5)$\times 10^6$ atoms$\times$0.3(4) s^{-1} =3.5(5)$\times 10^7$ atoms$\cdot$s^{-1}. For the calculation of errors, the error propagation formula for independent variables is used. The dependence of the loading rate and the lifetime on the trapping parameters: magnetic field gradient, cooling intensity and detuning is demonstrated in the following paragraphs.

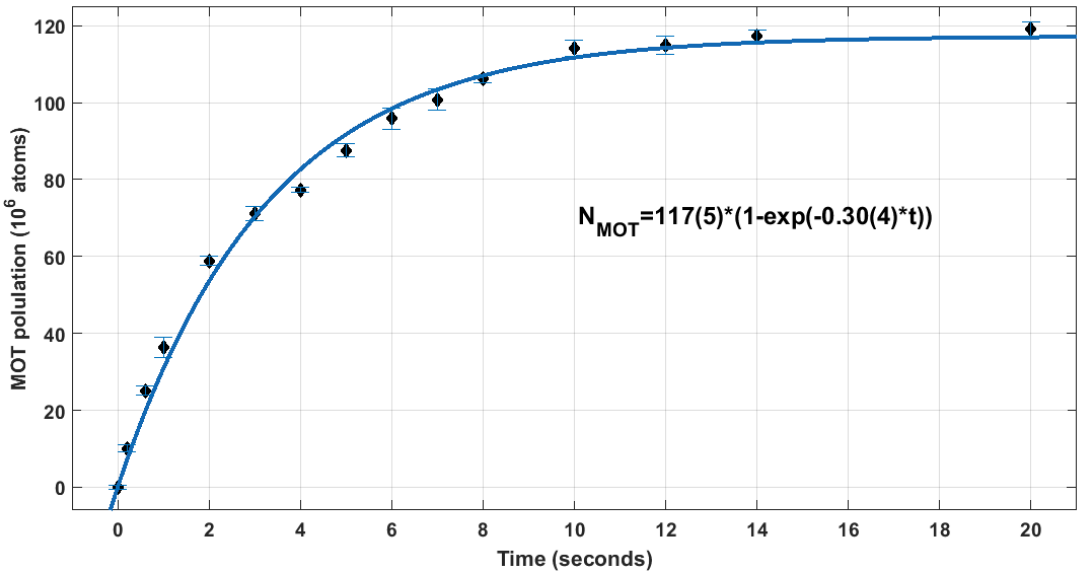

Figure 2.13: The measurements were performed at 32 mW/cm^2 total cooling intensity, 2 cm laser beam diameter, -1.7Γ (≈9 MHz) cooling laser's detuning and 14 G/cm magnetic field gradient. Using Eq. 2.14, we derive N_s =117(5)×10^6 atoms and the total loss rate $b = \gamma + \beta n_0$ =0.30(4) s^{-1}. Each data point is the average of three measurements and the error bars represent the standard deviation. The reduced χ^2 for this fit was calculated ≈11, potentially indicating that more data points or/and more measurements per data point were required for further improving the fit.

2.4.1.1.1 Loading rate and lifetime versus magnetic field gradient

The role of the magnetic field gradient, ($\frac{dB}{dz}$), in the magneto-optical trapping, has been the centre of many theoretical and experimental studies [49], [68], [69].

Figure 2.14 shows that the loading rate increases with the magnetic field gradient. This behaviour is explained by the dependence of the MOT's capture velocity on the applied gradient. By increasing the $\frac{dB}{dz}$, the Zeeman effect is enhanced resulting in more energetic atoms being on resonance with the cooling light. However, as shown in Fig. 2.14 and other works [49], [69], there is an upper limit for the capture velocity. When increasing the $\frac{dB}{dz}$, while keeping the rest of the MOT parameters constant, the resonant atomic speed will reach a level at which the trapping path (i.e. trapping region) is not sufficient to decelerate the atoms on time resulting in their escape. The above constraint can be circumvented by increasing the trapping area (i.e. diameter of laser beams) or the damping force. The latter can be achieved by increasing the detuning (increasing its absolute value, which in the context of this thesis means going to more negative detunings) or/and the intensity of the cooling light.

The higher loading rate comes at a cost of the lifetime. As Fig. 2.15 illustrates, the lifetime of the MOT decreases with the gradient, implying higher losses. The losses can be

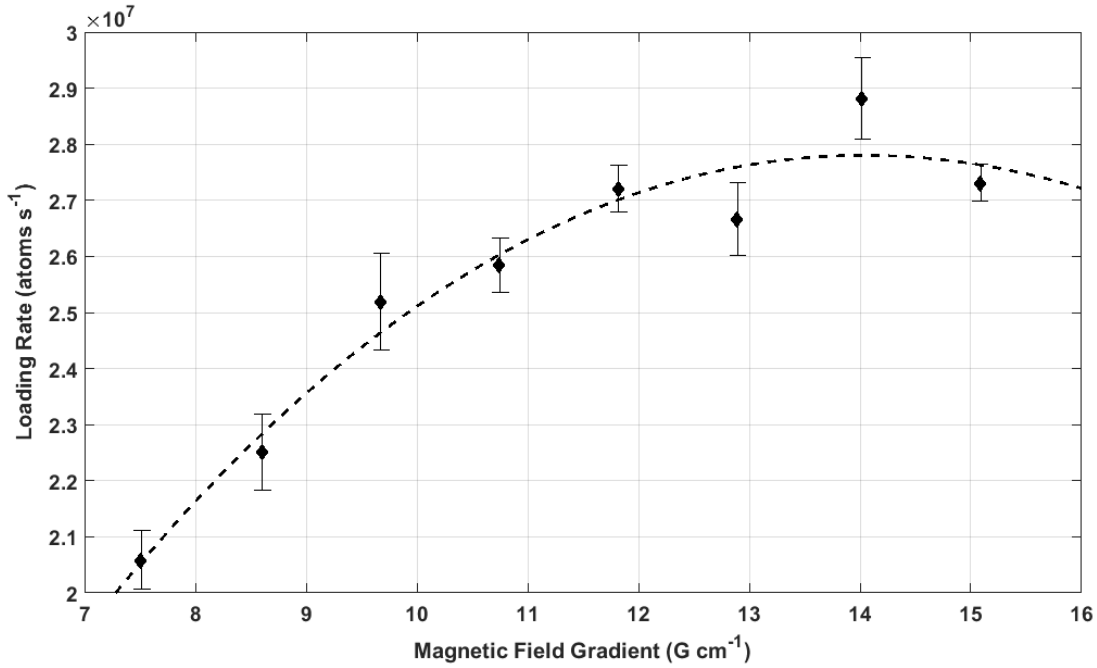

Figure 2.14: The loading rate's dependence on the magnetic field gradient. The total cooling intensity is $\sim$10 mW/cm^2 and the detuning -1.7Γ. The line is a guide for the eye.

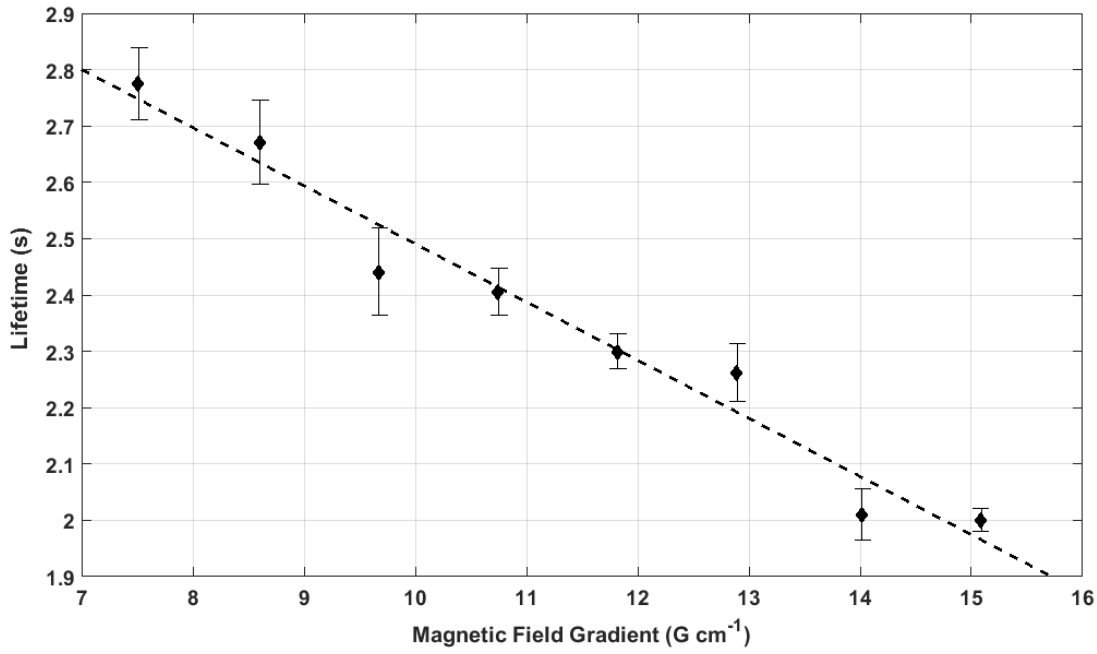

Figure 2.15: The lifetime's dependence on the magnetic field gradient. The total cooling intensity is $\sim$10 mW/cm^2 and the detuning -1.7Γ. The line is a guide for the eye.

attributed to enhanced collisions between cold atoms due to higher densities-temperatures in a "tighter" trap-confinement. This density-dependent behaviour of the two-body collisions is expressed mathematically by the term $\beta \cdot n_0$ in Eq. 2.13.

2.4.1.1.2 Loading rate and lifetime versus cooling intensity

The dependence of the MOT parameters, such as capture velocity [49] [70] [71] [72] and two-body loss rate coefficient [60] [73] [74] [75], on the total cooling intensity has been also investigated. Results are shown in Fig. 2.16 and 2.17.

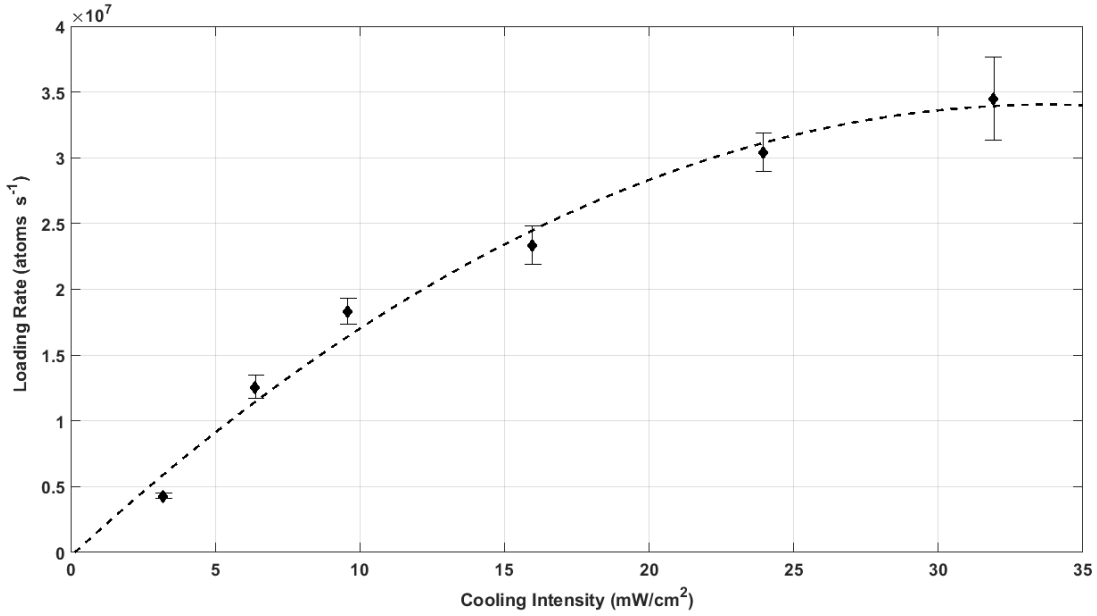

Figure 2.16: The loading rate's dependence on the total cooling intensity. The magnetic field gradient is $\sim$14 G/cm and the detuning -1.7Γ. The line is a guide for the eye.

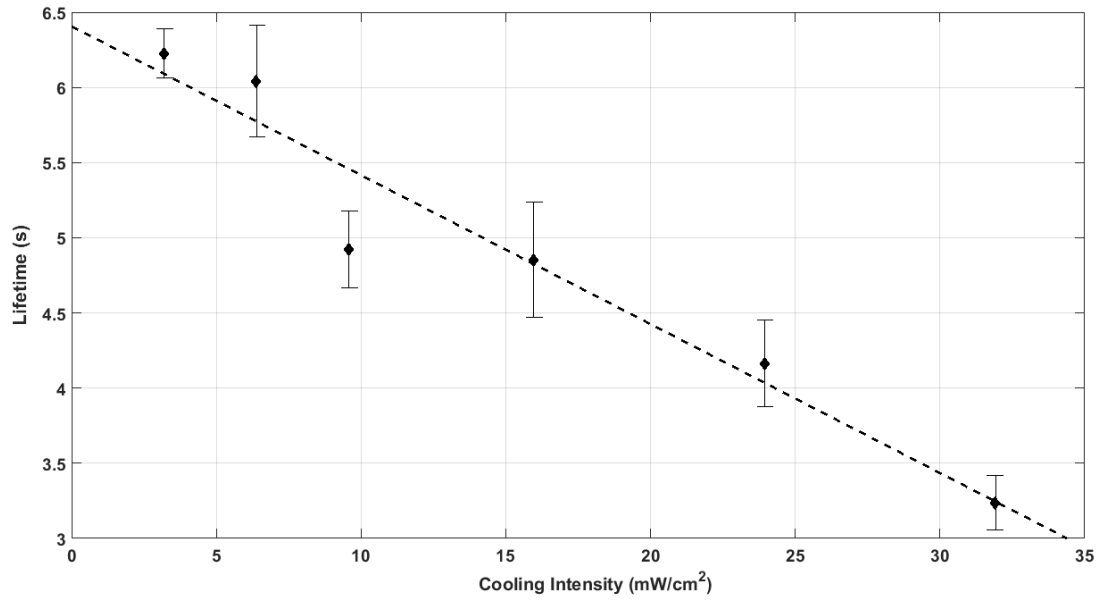

Figure 2.17: The lifetime's dependence on the total cooling intensity. The magnetic field gradient is $\sim$14 G/cm and the detuning -1.7Γ. The line is a guide for the eye.

Figure 2.16 shows the dependence of the loading rate on the cooling intensity. By

increasing the intensity, the damping force applied on the atoms is increased as well, resulting in a more efficient loading of the MOT. However, the loading rate starts to saturate above a certain intensity level. The above phenomenon can be explained by power broadening of the atomic levels (increase of the transitions' line-widths) at higher intensities, which results in the atoms not being able to distinguish between the counter-propagating beams, therefore the damping force (felt by the atoms) is decreased together with the efficiency of the cooling mechanism. While it is not demonstrated in this work due to laser-power constraints, at higher intensities, the capture velocity and subsequently the loading rate is expected to decrease [49] [71] [72].

Figure 2.17 shows the dependence of the lifetime on the cooling intensity. This behaviour can be understood by looking at Eq. 2.16. While the single-body rate coefficient, γ, is independent of the MOT parameters, β increases with intensity due to light-assisted collisions (RE and FS) (some examples: [52], [60], [50], [75]). Both RE and FS (introduced in Section 2.4.1) involve ground state and excited atoms, which explains their increase for higher intensities of the cooling beam. Specifically, we can see that the lifetime-total loss rate seem to show a linear decrease-increase with intensity, in a good agreement with theoretical predictions and experimental observations for the two-body loss rate coefficient, β. Finally, a small increase in density with the cooling intensity, affecting the density-dependent two-body loss rate, is expected and was experimentally observed during later experiments (see Section 2.4.2).

2.4.1.1.3 Loading rate and lifetime versus cooling detuning The detuning of the cooling light is crucial for both the loading rate and the lifetime of the MOT. The MOT operates for a small range of detunings, which depends on the other MOT parameters (intensity, magnetic field gradient, beams' diameter). Henceforth, increasing/decreasing the detuning will refer to the increase/decrease of the absolute value of the cooling light's detuning, e.g. low detunings will be values closer to 0 or resonance.

The loading rate, being proportional to the capture velocity, increases with the increase of the detuning, acquiring a maximum value, and then starts decreasing [68] [69], as shown in Fig. 2.18. Similar to the increase of the $\frac{dB}{dz}$, by increasing the detuning to high values, the light starts to interact with faster atoms. However, when increasing the detuning one needs to increase the $\frac{dB}{dz}$ at the same time, otherwise beyond a certain value the Zeeman shift will not be able to compensate for the detuning of the slow atoms, and the damping force will start decreasing.

With a similar approach to the one used for explaining the loading rate behaviour, the

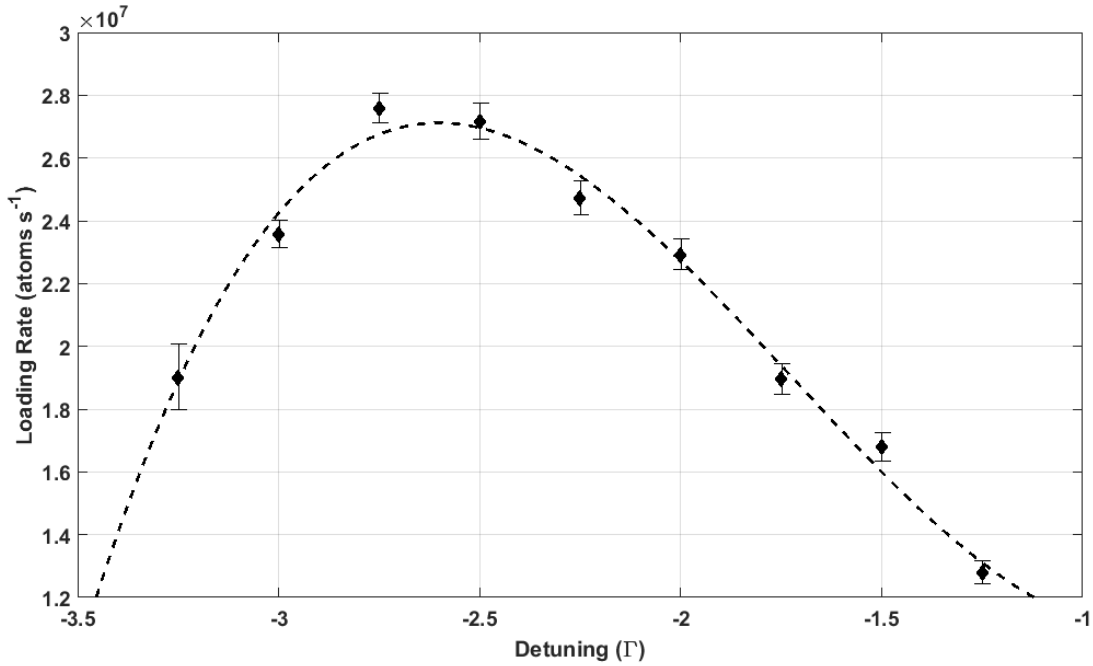

Figure 2.18: The loading rate's dependence on the cooling laser's detuning. The magnetic field gradient is $\sim$14 G/cm and the total cooling intensity $\sim$10 mW/cm^2. The line is a guide for the eye.

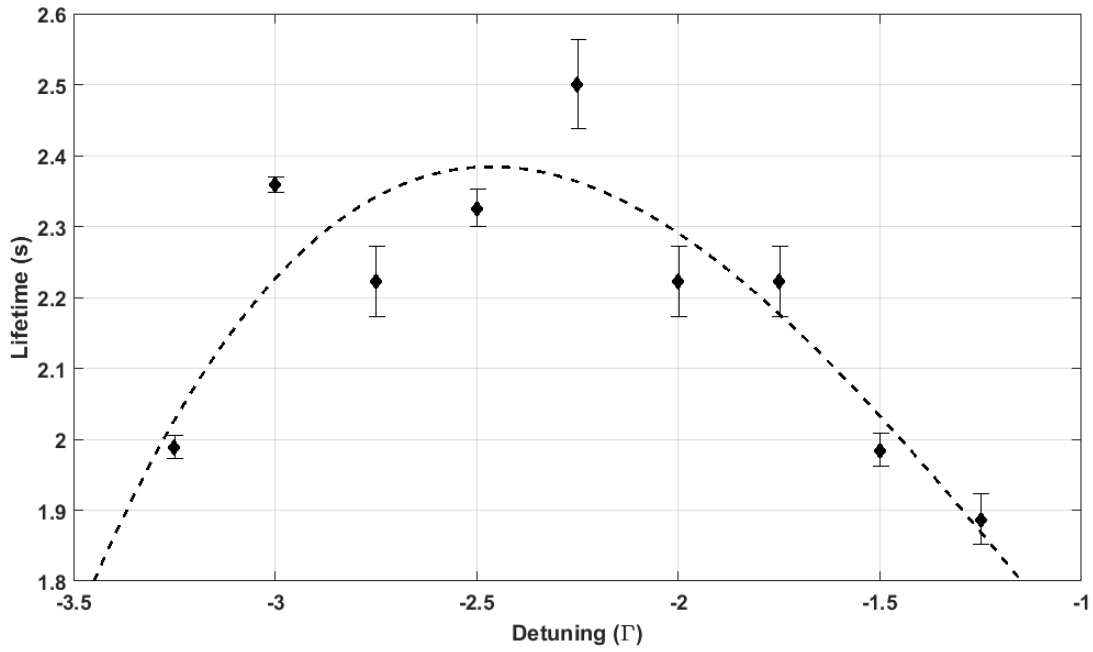

Figure 2.19: The lifetime's dependence on the cooling laser's detuning. The magnetic field gradient is $\sim$14 G/cm and the total cooling intensity $\sim$10 mW/cm^2. The line is a guide for the eye.

lifetime's trend can be analysed. While the $\frac{dB}{dz}$ alters the way the atoms interact with the light (hence the effect on the loading rate), the main process behind the decrease of the lifetime in Fig. 2.19 can be attributed to enhanced single-body losses. When the detuning

is increased above or decreased below certain values, it lowers the trap's depth, and the energy gained from collision between cold and hot background atoms becomes sufficient for the trapped atoms to escape.

2.4.1.1.4 Loss coefficients: β and γ The importance of the two-body, β, and the single-body, γ, loss rate coefficients, together with their different roles, have been already presented. While this tends to be out of the current thesis's purpose, one could try and estimate the order of magnitude of the aforementioned coefficients.

From Eq. 2.14, it becomes clear that for calculating β, γ has to be measured first. One way to measure γ, independently of β, is to operate the MOT at low densities, when the collisions between cold atoms start to be negligible. In Marcassa et al. [60], β is minimised by tuning the lasers with a different scheme for sodium and creating a weaker trap with densities $\sim 10^8$ atoms/cm^3. In the same paper is proposed that one can also measure γ, by measuring the total loss rate, b, for different cooling intensities, and then extrapolating to very small values. For the purpose of our work, the latter approach is considered the only solution capable of providing us with an estimation of both loss rate coefficients.

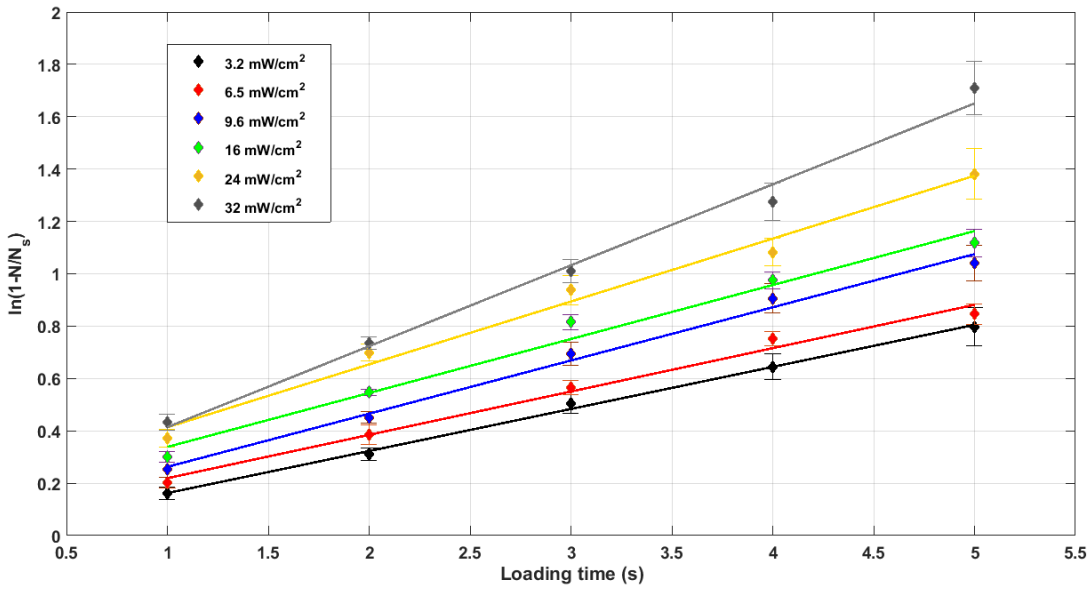

Figure 2.20: Logarithmic plots for the loading of the MOT at a different cooling intensities. The linearity of these plots confirms the presence of the constant density regime [60]. The very early loading times, when the constant density regime has not been achieved, have been ignored.

Figure 2.20 shows an alternative way to the usual curve fitting (see Fig. 2.13) for calculating the total loss and loading rates of a MOT for different cooling intensities (example [60]). For the y axis, the $ln(1 - N/N_s)$ is chosen (from Eq. 2.14), while the x axis reports the loading time. The linearity of these plots confirms that our MOT operates in

the constant density regime during each of the different cooling intensities. While one still needs to make a plot similar to Fig. 2.15 beforehand to calculate N_s, this approach has the advantage of being able to choose the range of loading times to be fitted. In our case, this was important because the very early times, during which the constant density regime was not present, should be left out.

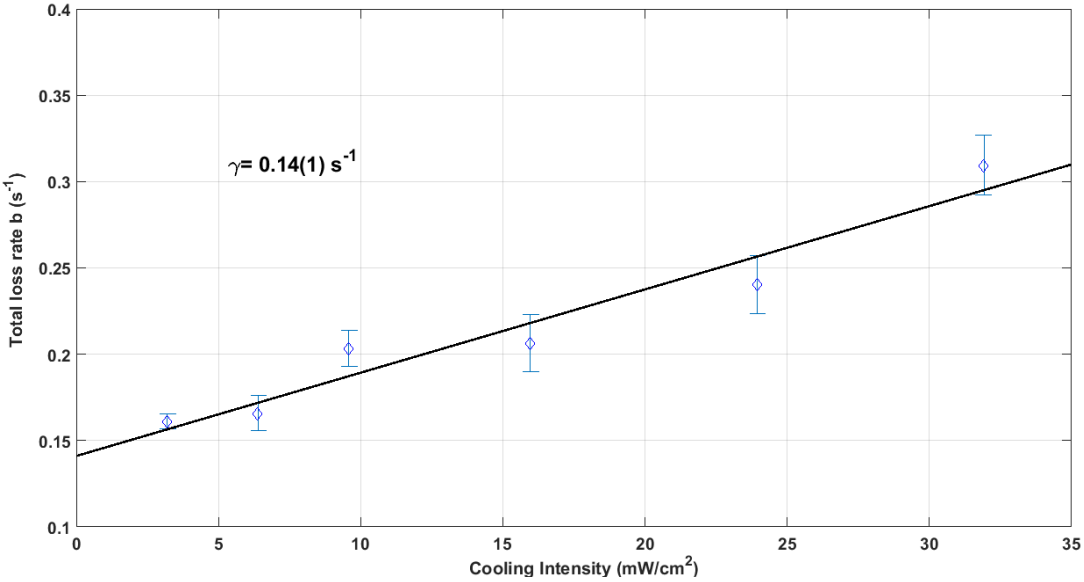

Figure 2.21: The total loss rate versus the total cooling intensity. By extrapolating to very low intensities, one can estimate the one-body loss coefficient. The data have been fitted with a linear fit of the form y=ax+b, where a= $0.005(2)$ and b= $0.14(1)$, and the reduced $\chi^2 = 1.5$. Therefore, for these experimental conditions γ =0.14(1) s^{-1}.

In Fig. 2.21, it is shown that the total loss rate decreases linearly with the decrease of the total cooling intensity, indicating the decrease of the two-body collisions loss rate ($\beta \cdot n_0$) and the gradual domination of γ. The single-body loss rate coefficient is independent of the cooling intensity. In particular, γ depends only on the background vapour density, which can be considered constant in this time-frame. By extrapolating to low cooling intensities, the data presented in Fig. 2.21 give γ =0.14(1) s^{-1}. As expected, the value above is higher that the single-body loss rate coefficient reported for MOTs loaded from atomic beams [50].

As an example, based on the calculated value of γ, for the case of 24 mW/cm^2 total cooling intensity at a density, n_0 =10^{11} atoms/cm^3, the two-body loss coefficient is: $\beta_{24} = (b_{24} - \gamma)/n_0$ =(0.24-0.14)/10^{11} $cm^3 \cdot s^{-1}$ =1×10^{-12} cm^3/s, which is smaller than the number reported in the literature by Sesko et al. [50] for Cs: 8×10^{-12} cm^3/s.

The value of γ can be also used for estimating the background gas pressure in cases where a direct measurement is not available or trustworthy. While we do have a direct trustworthy measurement of the gas pressure in our science chamber by our Agilent ion pump,

ranging from 10^{-9} to 10^{-8} mbar, we can still try to do an estimation of the pressure based on the theoretical model of Bali et. al. [76]. The latter can be applied to shallow optical or magneto-optical traps, operating at high densities and low temperatures. Considering that we are operating in the UHV region, it is safe to assume that the dominant background gas is hydrogen (H_2), which is very light and mobile, hence difficult to pump out. For cold Cs-H_2 collisions, it is reported that γ/n_p =5.3$\times10^{-9}$ cm^3/s. Here n_p refers to the density of atoms of the background gas (in this case H_2). By using the absolute pressure equation for ideal gases we get:

$$p = n_p \cdot k_B \cdot T = 1.1 \times 10^{-12} bar = 1.1 \times 10^{-9} mbar, \tag{2.17}$$

with k_B =1.38$\times10^{-23}$ J/K, T =293 K, n_p =2.64$\times10^7$ atoms/cm^3. The calculated background pressure lies within the low end part of our measured pressures for this experimental phase.

2.4.2 Temperature, density and phase-space density measurements

Measurements of the temperature, density and phase-space density are necessary for fully characterising a MOT, but more importantly, they are crucial for the preparation of the next phases, which would be optical molasses, dipole trap and eventually a Bose-Einstein Condensate of ^{135m}Cs isomers. The aforementioned properties were determined with the Time-Of-Flight (TOF) method using absorption imaging, which was extensively analysed in Section 2.2. Having demonstrated the ability for such measurements, the next step was to understand their dependence on the main MOT parameters: detuning Δ, cooling intensity I and magnetic field gradient $\frac{dB}{dz}$.

2.4.2.0.1 Temperature versus $I, \Delta, \frac{dB}{dz}$ It has been theoretically and experimentally shown that there are both Doppler and sub-Doppler cooling mechanisms present in a MOT (see Chapter 1, Section 1.2.3). The Doppler cooling mechanism is characterised by the viscous force applied on moving atoms due to the Doppler effect, and the achieved temperature, T, is mathematically described as [39]:

$$k_B T = \frac{h\Gamma}{8\pi} \frac{1 + (2\Delta/\Gamma)^2}{-2\Delta/\Gamma}, \tag{2.18}$$

where k_B, h are the Boltzmann and Planck constants, Γ the natural line-width and Δ the detuning of the cooling laser. The minimum temperature achieved based on the above equation for Cs is given for a red detuning of $\Delta = \Gamma/2$, T$_D$ =125 μK. Apart from the first

experiments with MOTs [34] [77], later experimental results (including the ones presented here) reveal much lower temperatures than the limit set by the Doppler cooling mechanism.

Dalibard and Cohen-Tannoudji [37] identified two cooling mechanisms, one for linear and one for circular polarised cooling lights, which explain the sub-Doppler temperatures in optical molasses-MOTs. While in the linear case, the atoms are further cooled via the Sisyphus effect, for circular polarisations the cloud's temperature is reduced due to unbalanced radiation pressures present in the central region of the trap. The difference in the radiation pressure felt by an atom is because of uneven population of the ground-state sublevels produced by the atomic motion, increasing the absorption of photons coming from a specific direction (depending on the movement of the atom), and it is not related to the Doppler effect. The above sub-Doppler mechanism is called polarisation gradient cooling, and it takes place for low laser powers, large detunings and it is only stronger than the Doppler cooling for low atomic speeds (i.e. they coincide but the two mechanisms work for different atomic speeds). The temperature of the trapped atoms can be described as [37]:

$$k_B T = \frac{h\Omega^2}{2\pi|\Delta|}\left(C_1 + C_2\frac{\Gamma^2/4}{\Delta^2+\Gamma^2/4}\right), \tag{2.19}$$

with k_B, h, Δ, Γ are defined as in Eq. 2.18, $C_{1,2}$ are numeric constants and Ω is the Rabi frequency. By looking at Eq. 2.19, we can notice that the temperature increases with Ω ($\sim$ laser intensity) and $1/|\Delta|$. Similar, but empirical, relations for the temperature, showing the analogous dependencies, were derived from Cooper et al. [54] and Drewsen et al. [55].

Results are presented in Fig. 2.22-2.24, and they are in line with the theory and the published data discussed here. Figures 2.22 and 2.23 show an increase of the temperature for higher intensities and a decrease for more negative detunings. While the latter is explained by the mathematical description of both cooling mechanisms, the former is the result of a combination of effects. For higher intensities, the sub-Doppler cooling mechanisms start to be less effective, while at the same time, the higher flux of photons causes increased scattering events therefore more energetic trapped atoms.

Figure 2.24 shows an increase of the temperature with the magnetic field gradient. This observation can be explained by taking into account that in high magnetic field gradients the sub-Doppler cooling mechanisms start to be ineffective, similar to the high laser intensities case, and that the MOT population will increase. The effect of the number of trapped atoms on the temperature of the cloud has been investigated, and experimentally demonstrated that the temperature scales with $N_{MOT}^{1/3}$ [54] [55]. The excess heating originates from the increase of multiple scattering events at higher atomic numbers (described in Section 2.4.1). Figure 2.25 demonstrates this linear dependence of the temperature on the $N_{MOT}^{1/3}$

based on our measurements. Finally, it has to be mentioned that the latter effect was also present in the cases shown in Fig. 2.22 and 2.23, since changes in the intensity and/or detuning affect the MOT population.

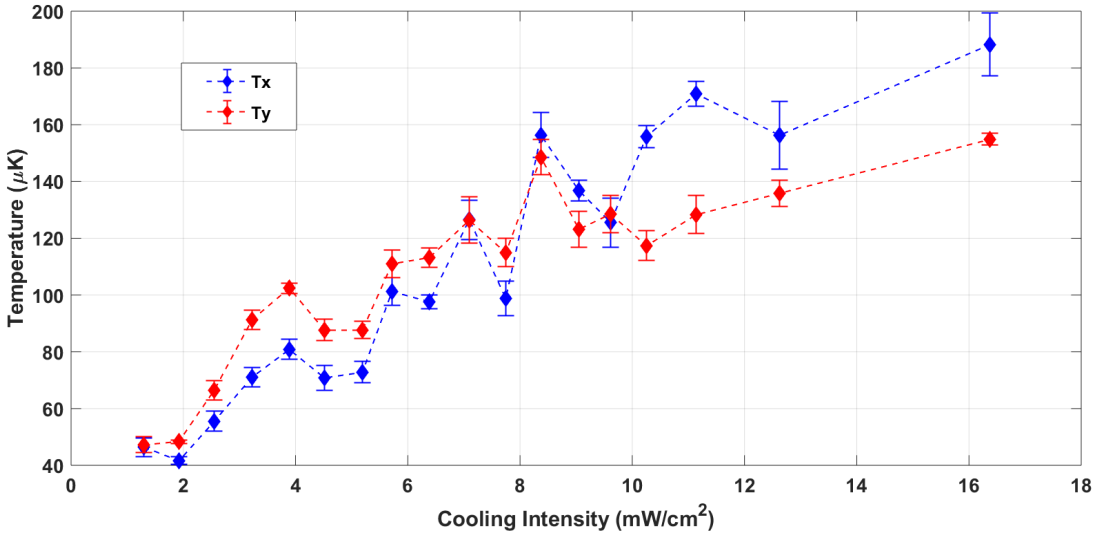

Figure 2.22: The temperature of the MOT in both x and y directions versus the total cooling intensity. The magnetic field gradient is $\sim$14 G/cm and the detuning -1.7Γ. The lines are guides for the eye.

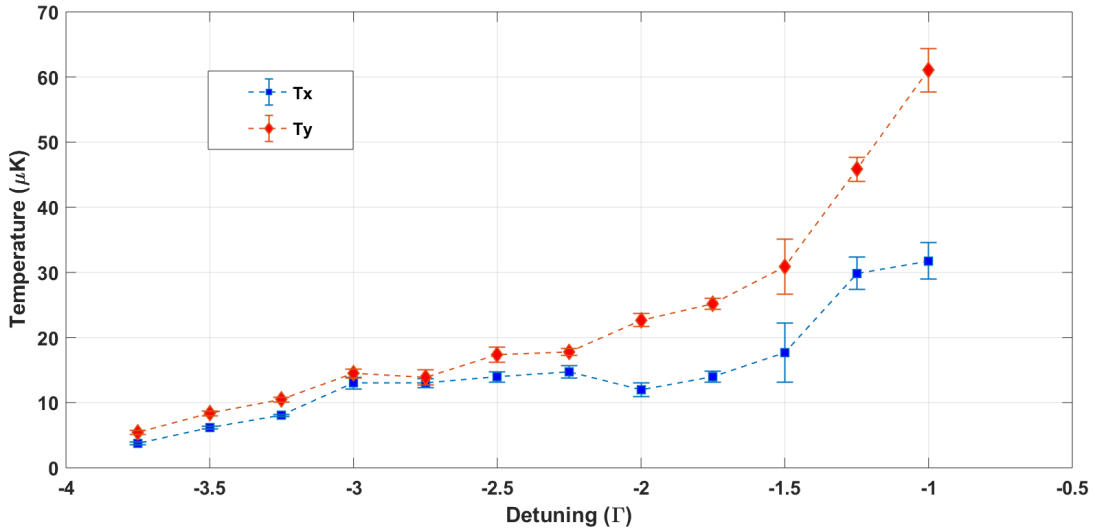

Figure 2.23: The temperature of the MOT in both x and y directions versus the detuning of the cooling beams. The magnetic field gradient is $\sim$14 G/cm and the total cooling intensity $\sim$10 mW/cm^2. The lines are guides for the eye.

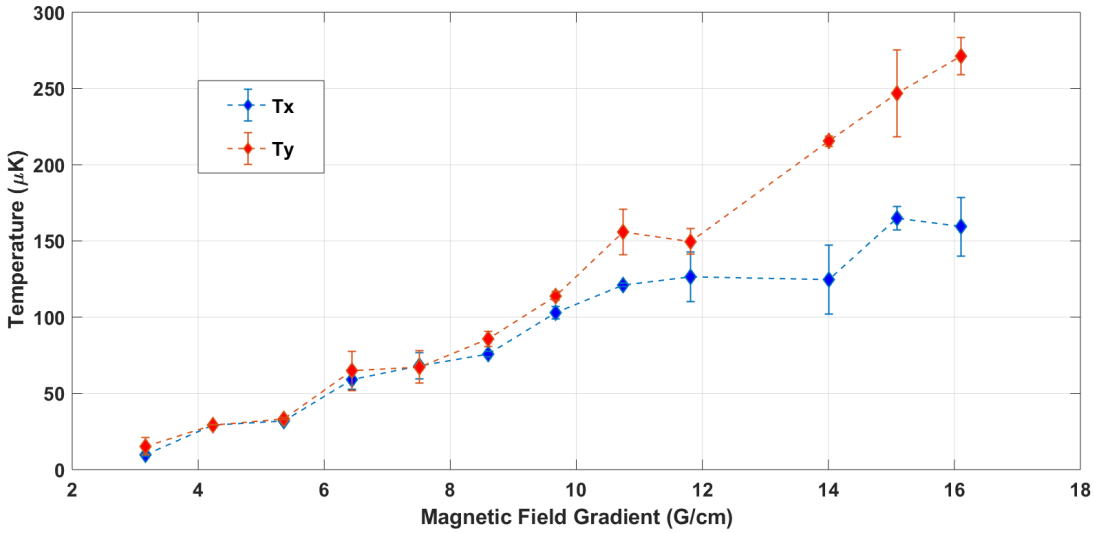

Figure 2.24: The temperature of the MOT in both x and y directions versus the magnetic field gradient. The total cooling intensity is $\sim$10 mW/cm^2 and the detuning -1.7Γ. The lines are guides for the eye.

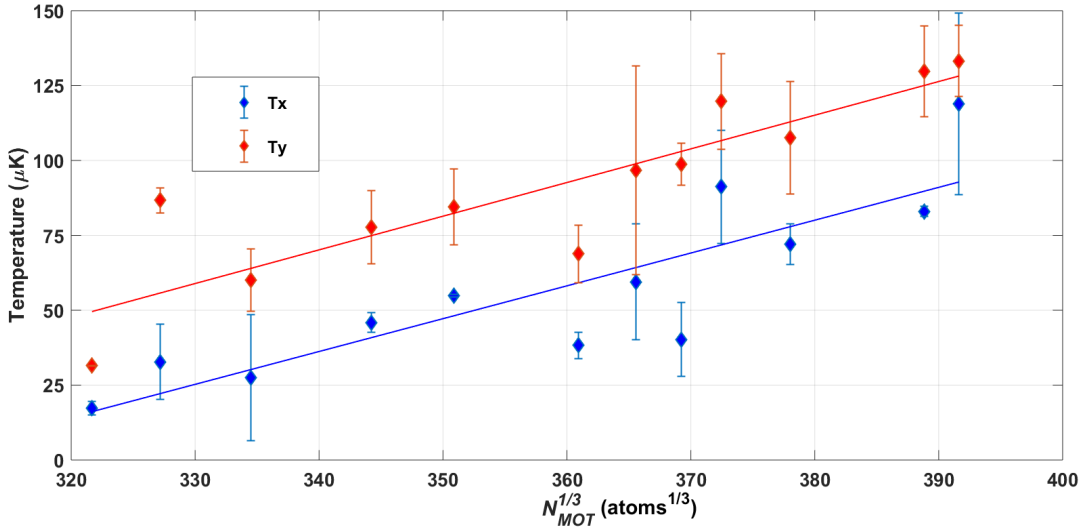

Figure 2.25: The temperature of the MOT in both x and y directions versus $N_{MOT}^{1/3}$, where N_{MOT} is the MOT population. The total cooling intensity is $\sim$10 mW/cm^2, the magnetic field gradient $\sim$14 G/cm and the detuning -1.7Γ.

2.4.2.0.2 Density and Phase-Space Density versus $I, \Delta, \frac{dB}{dz}$ The density and phase-space density were measured versus the detuning, magnetic field gradient and cooling intensity. It has to be noted that while our density measurements are in a good agreement with theoretical predictions and experimental observations, they are not as precise as the MOT population and temperature measurements. The latter is the result of the relatively low number of TOF points used for the extrapolation of the volume of the cloud to the beginning of the expansion (i.e. TOF=0 time). In the case that in the future it is decided to proceed with a more accurate determination of the absolute values of density and phase-space density, more points will be used (e.g. 3-5-7-9-11 ms TOF instead of the 5-6-8 ms we have been using during these measurements). Nevertheless, as mentioned above, the general behaviour of our measurements seem to agree well with the literature.

Townsend et al. [57] described the maximum density of the MOT achieved in the density-limited regime for $\Delta > 2\Gamma$ as:

$$n_{max} = \kappa_0 \frac{\Gamma}{\Delta} \frac{b}{b_0} \frac{1}{3\lambda h \Gamma} \frac{(4\Delta^2 + \Gamma^2 + 12\Omega^2)^2}{18\lambda\hbar\Gamma\Omega^4} \frac{\Delta^2 + 6\Omega^2}{\Delta^2 - 2\Gamma^2}, \tag{2.20}$$

where κ_0 is a constant of proportionality, b the magnetic field gradient ($\frac{dB}{dz}$), b_0 is considered 1 G/cm, and the rest have been defined in previous sections. Equation 2.20 expresses mathematically the dependencies of the maximum density, in the density-limited (or multi-scattering) regime, on the detuning, cooling intensity and magnetic field gradient.

Figures 2.26a and 2.27a show that the density increases with the intensity and the magnetic field gradient. The above observation agrees with Eq. 2.20, and it has been reported in the literature [78]. Figure 2.28a shows the density acquiring a maximum close to -3Γ and then decreasing with the detuning, with Townsend et al. [57] reporting similar observations. Analogous to the explanation behind the loading rate behaviour at Fig. 2.18, the trap starts to operate less efficiently in very large detunings, and the actual maximum detuning differs with the experimental conditions.

The phase-space density behaviour is quite complex, since it depends on both the density and temperature of the cloud. Figures 2.26b and 2.27b do not allow any conclusion since by comparing the behaviour of the temperature in Paragraph 2.4.2.0.1 to the behaviour of the density, it can be noticed that they have opposite dependencies on the intensity and the magnetic field gradient. Overall, the phase-space density increases with the detuning (see Fig. 2.28b), since the density increases, and the temperature decreases at the same time. Although not visible in Fig. 2.28b, one should expect that the phase-space density will acquire a maximum and then decrease, since the density will decrease rapidly for very large detunings.

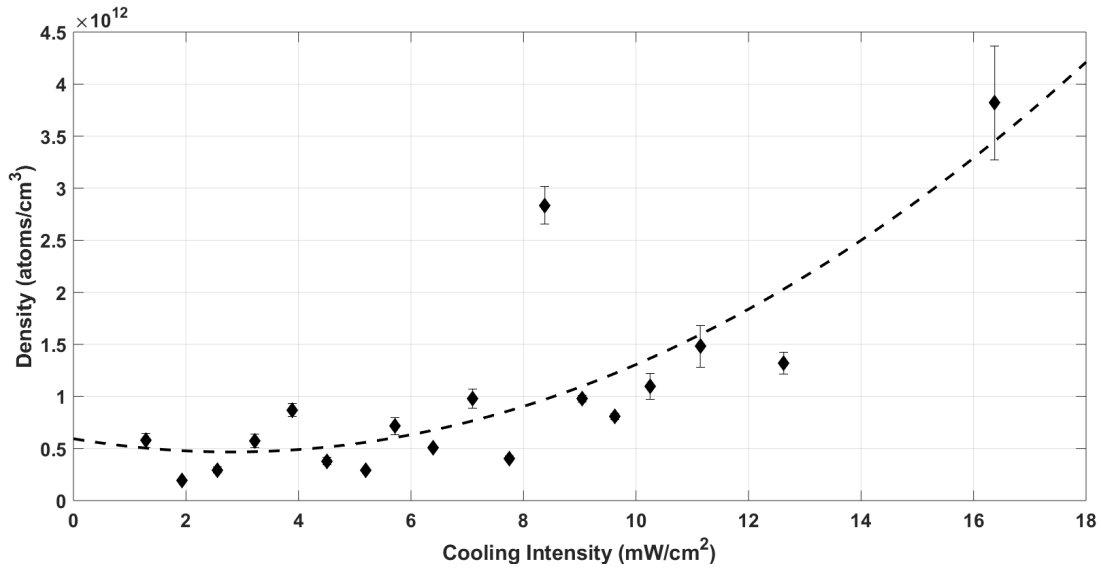

(a)

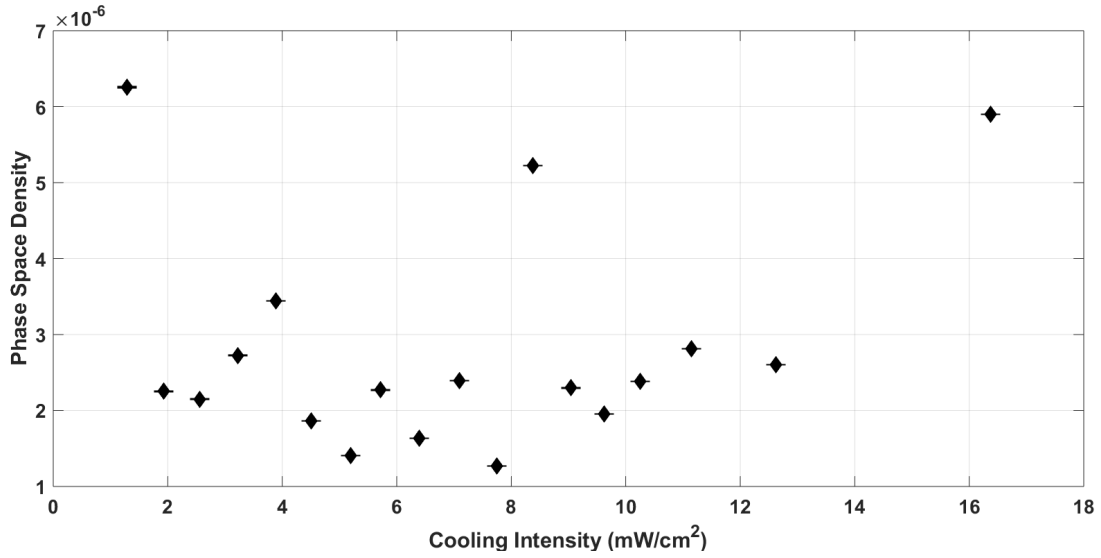

(b)

Figure 2.26: The density and phase-space density of the MOT versus the total cooling intensity. The magnetic field gradient $\sim$14 G/cm and the detuning -1.7Γ. The line is a guide for the eye.

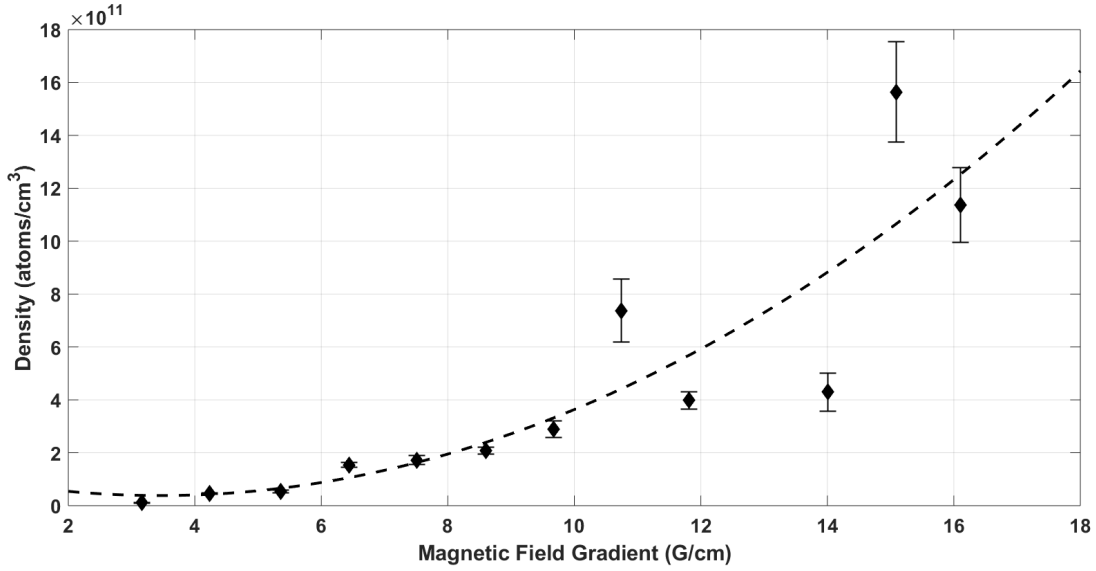

(a)

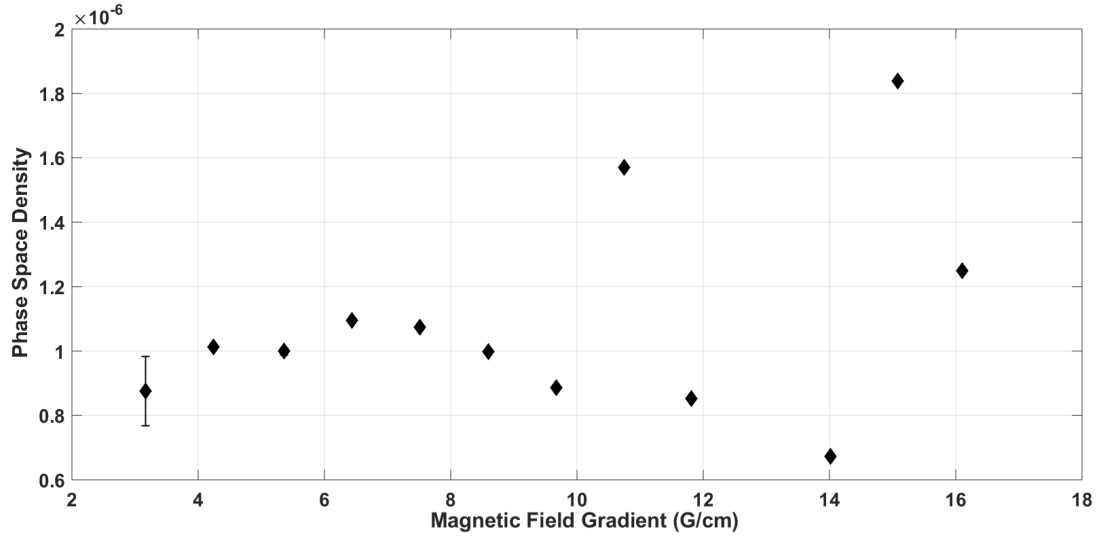

(b)

Figure 2.27: The density and phase-space density of the MOT versus the magnetic field gradient. The total cooling intensity is $\sim$10 mW/cm^2 and the detuning -1.7Γ. The line is a guide for the eye.

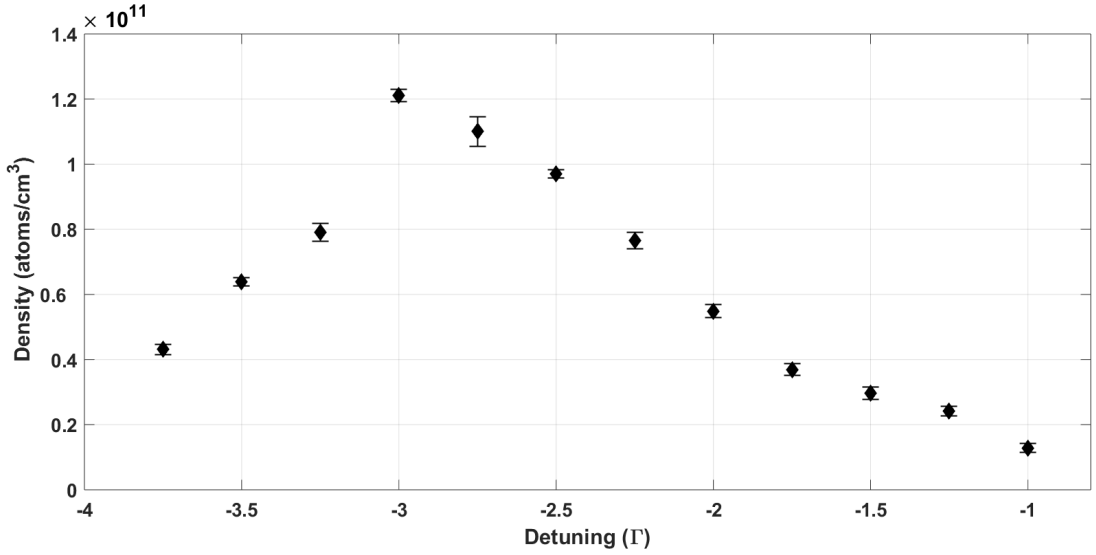

(a)

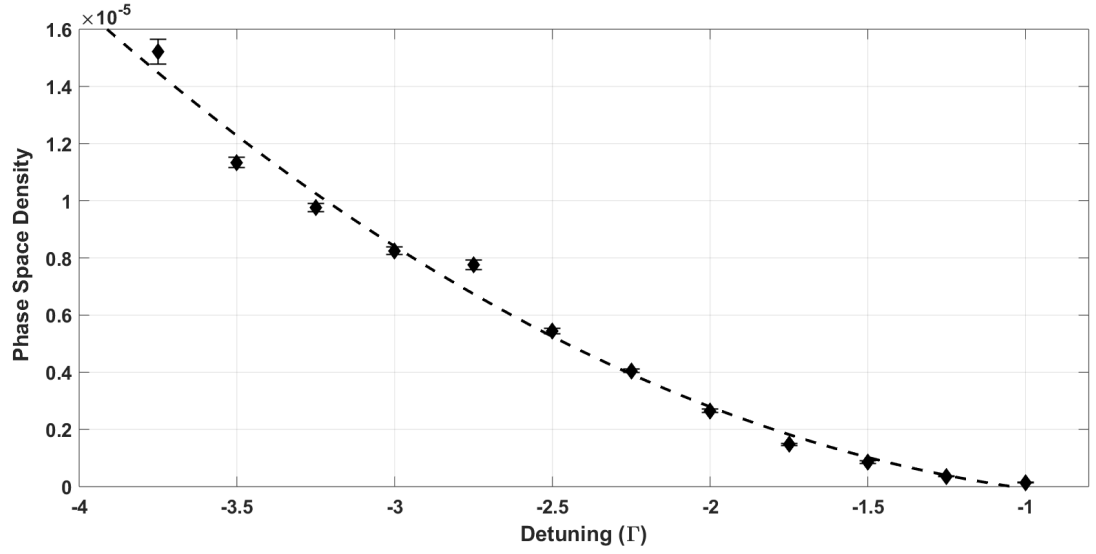

(b)

.

Figure 2.28: The density and phase-space density of the MOT versus the cooling detuning. The total cooling intensity is $\sim$10 mW/cm^2 and the magnetic field gradient $\sim$14 G/cm. The line is a guide for the eye.

Chapter 3

Second Phase: On-line set-up

The second experimental phase of my work was focussed on the building and testing of a facility for the production of ultra-cold atomic samples of Cs isotopes and isomers. The laser cooling facility was assembled at the Accelerator Laboratory of the University of Jyväskylä within the Ion Guide Isotope Separator On-Line (IGISOL)-4 facility (see Fig. 3.1). An important part of the information included in this chapter has been published in Giatzoglou et al. [2].

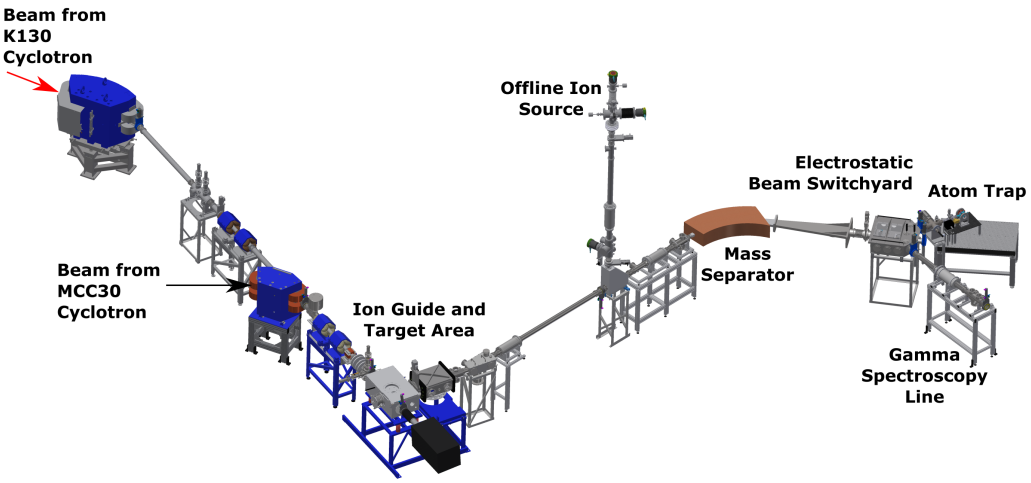

Figure 3.1: A 3D graphical illustration of the IGISOL IV facility. On the right, the atom trap is shown without the optics and laser system for clarity.

The facility's operation can be divided into two parts based on the involved energies: high-energy and low-energy. The high-energy part comprises the production, acceleration and mass separation of the ions. The low-energy part starts with the implantation of the ions into our yttrium thin foil, where they are thermalised (stopped), neutralised and thermally diffused to the science chamber as neutral atoms. Following their diffusion, the

atoms are laser cooled and eventually trapped in a magneto-optical trap (MOT). Within $\sim$5 seconds, the energy is reduced by 14 orders of magnitude, scaling from 10^{6} eV (primary beam's energy) down to 10^{-8} eV (MOT).

At the Accelerator Laboratory, stable and unstable ionic beams are routinely produced using light-ion primary beams from a K130 (130 MeV light- and heavy-ion) cyclotron or a new MCC30 (30 MeV light-ion) cyclotron via fission or fusion-evaporation nuclear reactions. In addition, a surface ionisation source (see Fig. 3.2) and a discharge ion source were recently developed and installed to provide IGISOL with stable beams, allowing tests prior to on-line runs and cooling periods, while they are also routinely used for development and research purposes [1].

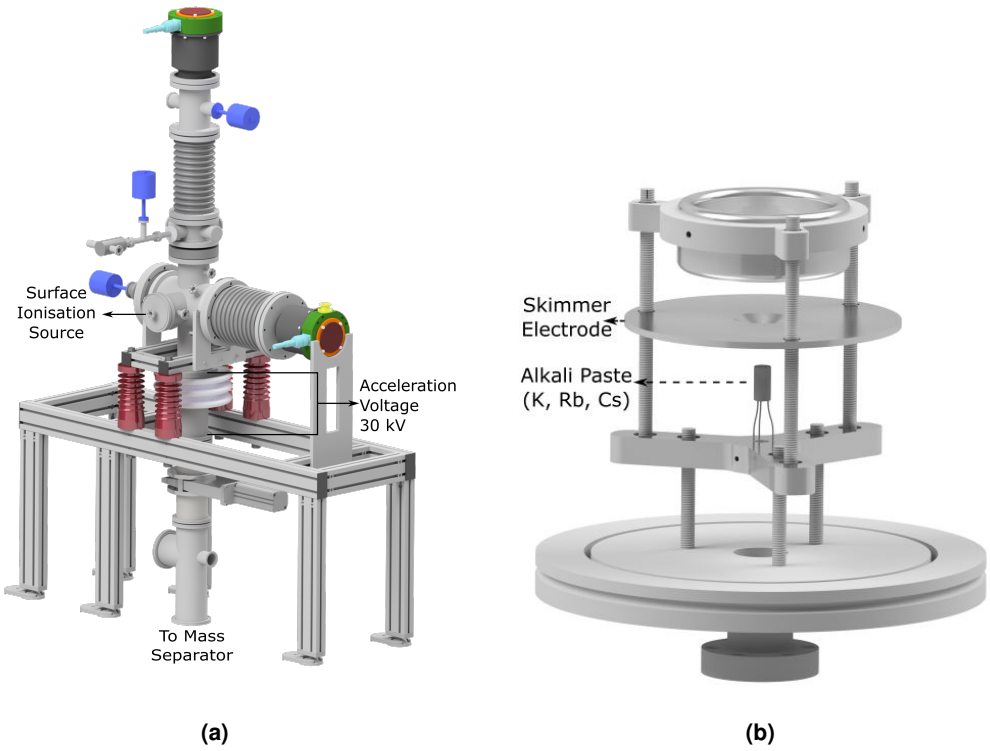

Figure 3.2: (a) The surface ionisation source station positioned on the second floor of IGISOL IV. The station, during our experiments, had been producing stable ions of K, Rb and Cs. The ion beam was then mass separated, and the Cs ions were routed to our science chamber. (b) The surface ionisation source. A metallic cylinder includes an alkali paste (K, Rb, Cs), which is heated up to 1000-1200 K. The high temperatures create an alkali plasma, which acts as a source of ions ready to be extracted using an electrode (skimmer). The sketches were retrieved from IGISOL's 3D library.

The stable ion beams produced at the off-line sources are accelerated to 30 keV and eventually merged into the main separator, from where they follow the same path with nuclear reaction products. The merging of the paths of the two beams is essential for testing and optimising an important part of the transport line, while using macroscopic

amounts of ions. The high intensity ion beams, such as those produced in off-line ion sources, are ideal because they can be detected by standard and relatively cheap beam diagnostic tools, e.g. Faraday cups, have a relatively low production cost, and there are no radiation related concerns.

Here, I report on the building and installation of the new facility, and present the results from the demonstration and characterisation of its operation using ionic beams of $^{133}Cs^{+}$. The $^{133}Cs^{+}$ ions were routinely produced at the off-line surface ionisation ion source (Fig. 3.2) on the second floor of IGISOL. Results from experiments involving radioactive beams will be reported in Chapter 4.

3.1 Experimental set-up

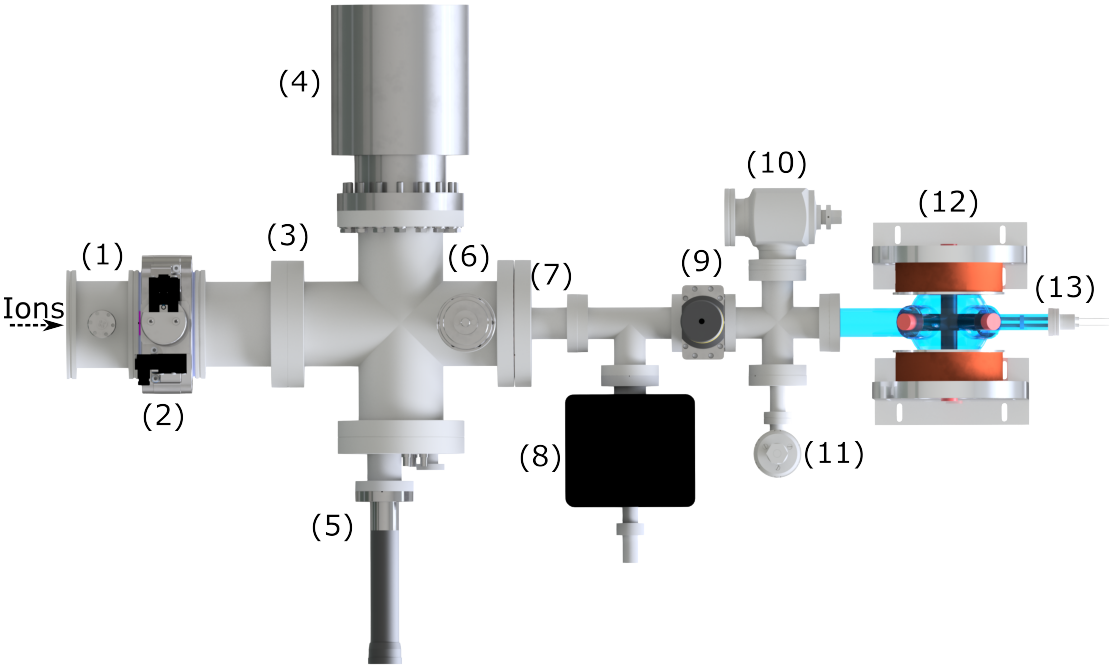

Figure 3.3: Cold atoms portion of the set-up. Starting from the left where the ions enter, the positions of the following components are shown: (1) X-Y plates, (2) CF100 Ultra-High Vacuum (UHV) pneumatic gate valve, (3) Einzel lens, (4) turbo-molecular pump (Leybold CE TURBOVAC 350i, capacity 350 l/s), (5) Faraday cup and actuator, (6) Penning gauge, (7) vacuum impedance, (8) 20 l/s ion pump (Agilent Varian VacIon Plus 20 StarCell), (9) CF40 UHV gate valve, (10) pre-evacuation CF40 valve, (11) ^{133}Cs ampoule's reservoir with a CF16 valve, (12) anti-Helmholtz coils and (13) yttrium thin foil holder.

Starting from the IGISOL's mass separator dipole magnet's exit, with a beam profile of radius R≈10 mm, the ion beam is directed to the electrostatic switchyard, where is further manipulated by a kicker plate, deflecting it either to the spectroscopy line or to the atom trap, and a deflector plate. The kicker plate deflects the beam by 10°, while the deflector

plate adds an extra 30° bending.

A new beam line was built and installed to deliver the mass separated 30 keV ions to the MOT set-up (atom trap), and it is equipped with ion optics, beam diagnostics and a turbo-molecular pump. The MOT set-up was built and connected to the new beam line, resulting in the completion of the facility for producing ultra-cold Cs samples (see Fig. 3.3). The laser system that was used during the stable and unstable atoms' laser cooling and trapping experiments is the same to the one used in the previous experimental phase and described in Chapter 2.

3.1.1 Ion-optics: X-Y plates and Einzel Lens

A set of four electrostatic parallel plates (X-Y plates) and a charged particles focussing lens (Einzel lens), placed in suitable CF chambers/casings, were installed in the new beam line, following a detailed simulation using the SIMION 8 package by Dr. Sami Rinta-Antila (University of Jyväskylä). X-Y plates and Einzel lenses are standard tools for ion beam related experiments, where the former are used for small angle deflection and the latter for focussing charged particle-ion beams. It has to be noted that in contrast to magnetic elements, electrostatic elements do not show any dependence on the mass-to-charge ratio (m/q) of the ions, and their trajectory is solely determined by the applied voltage. This, together with merging the off-line and on-line beams' paths, allowed us to optimise the transport efficiency of the beam line by using a stable beam producing macroscopic ("Faraday cup") amounts, and use the same settings for the online experiments involving radioactive beams and different masses.

High voltage is applied to each pair of electrodes-plates shown in Fig. 3.4a and 3.4b, supplied by a Spellman 1 kV DC source and regulated via the LabVIEW platform. By applying a voltage to any of the electrode pairs, electrostatic forces act on the highly-energetic ions going through the 30 mm wide opening of the X-Y plates, and alter their trajectory. During the on-line (radioactive beams) and off-line (stable beams) experiments, the X-Y plates were used for the fine tuning of the beam in order to maximise the transmission to the neutraliser.

Figures 3.4c and 3.4d show the Einzel lens installed. The three element Einzel lens comprises three co-axial cylindrical electrodes, where the side electrodes are grounded, and the central one is placed in high ($\sim$ kV) negative voltage (see Fig. 3.4c). The total length of the lens is 100 mm, the electrodes' separation 10 mm and its inner diameter 20 mm. The lens electric field is used for focussing the ion beam through the final vacuum

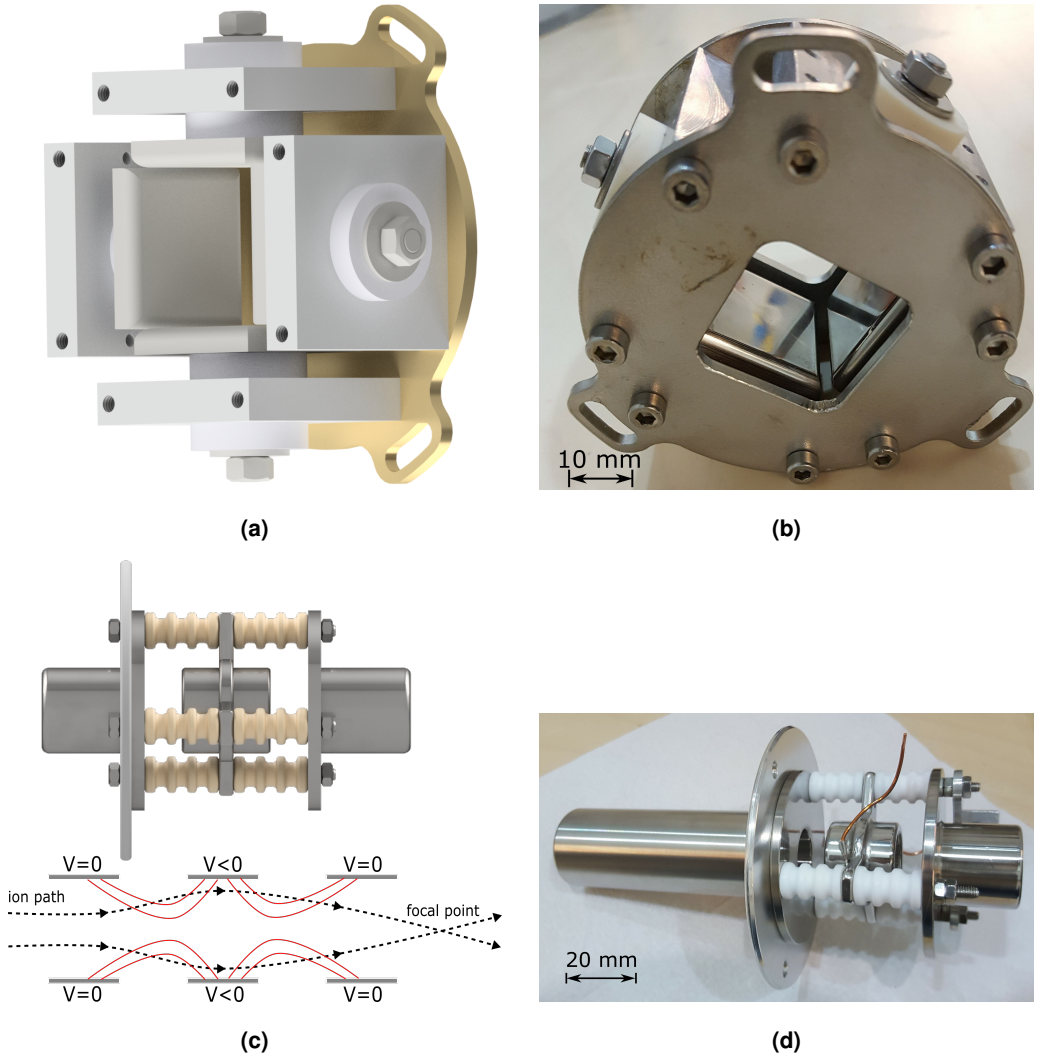

Figure 3.4: Pictures and 3D sketches of the ion optics installed in the dedicated, to our experiment, beam line. Figures a-b) show the X-Y plates and c-d) the Einzel lens. The original designs by Dr. Sami Rinta-Antila.

impedance ((7) in Fig. 3.3) onto the neutraliser. By increasing the applied voltage, the focal point is moving closer to the lens, while for lower voltages the beam is focussed further down the transport line. The control voltage was supplied by a Spellman 15 kV DC voltage source and regulated via LabVIEW. It worth mentioning that one of the lens's grounded electrode is a few centimetres longer than the one originally considered in the design (see Fig. 3.4d). This is due to the fact that the elongated electrode also acts as a vacuum impedance.

3.1.2 Dedicated beam line

The role of the new beam line can be better understood by looking at Fig. 3.5. The X-Y plates placed at the beginning of the line, in the position labelled as (1) in Fig. 3.5, are used to steer the ion beam, as described in Section 3.1.1, and to compensate for any

deviation from the optimum path. Their control voltage is supplied via the CF16 electrical feedthroughs placed on top of the plates. The next component shown is the CF100 pneumatic valve (2), which allows updates/changes to be performed in IGISOL's switchyard without affecting our system and vice versa. The Einzel lens (3), as described in the previous Section 3.1.1, is used to maximise the transmission through the last vacuum impedance (7) to the neutraliser foil, but it is also acting as a vacuum impedance itself. The lens's control voltage is provided via the CF40 high-voltage electrical feedthrough. Towards the end of the line, the CF63 cross-chamber is connected to a turbo-molecular pump (Leybold CE TURBOVAC 350i) (4), a Faraday cup (5), a Penning gauge (6) and a CF63/CF40 adaptor. The Faraday cup is the last beam diagnostic before the neutraliser. The foil acts also as a beam diagnostic (measures ion current), therefore allowing maximisation of the transport efficiency. The high pumping speed of the turbo-molecular pump (350 l/s for H_2) maintains the vacuum in the beam line $\leq 10^{-8}$ mbar (as measured by the Penning gauge), even during abrupt openings of the CF100 valve and exposure of the system to the $\sim 10^{-7}$ mbar switchyard pressure. The CF63/CF40 adaptor contains the last vacuum impedance (7) present in the beam line, which is crucial in maintaining an average pressure $\sim 1 \times 10^{-9}$ mbar in the MOT set-up, as measured by the ion pump. The lowest pressure that has been measured in our science chamber was high 10^{-10} mbar.

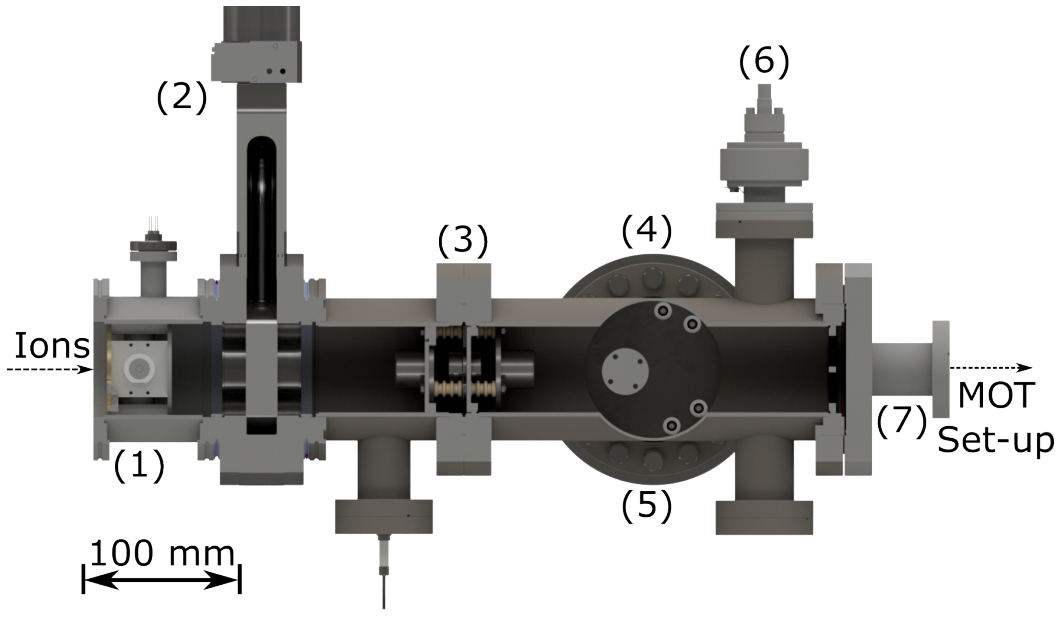

Figure 3.5: Cross-sectional view of the beam line. The labelling is the same as in Fig. 3.3: (1) X-Y plates, (2) CF100 Ultra-High Vacuum (UHV) pneumatic gate valve, (3) Einzel lens, (4) turbo-molecular pump (Leybold CE TURBOVAC 350i, capacity 350 l/s), (5) Faraday cup and actuator, (6) Penning gauge and (7) vacuum impedance. The original design by Dr. Sami Rinta-Antila.

3.1.3 MOT set-up

The MOT configuration, described in Chapter 2, was updated during the activity of the 3rd year of my PhD. The main updates can be summarised as: a new science chamber was introduced together with a new set of anti-Helmholtz coils, and a special anti-adsorption coating was produced and applied on the inner walls of the Pyrex chamber. Adjustments in the optical alignment were also necessary to account for the new optical paths set by the chamber's dimensions. An important update regarding our data acquisition hardware took place: the NI 6009 USB DAQ board was replaced with the NI 6353 USB DAQ, followed by the necessary hardware upgrades. The new DAQ offers significantly higher performance (such as $\sim$20 times higher sampling rate and 4 times better timing resolution) and many additional input/output channels (analogue and digital). The remaining of the hardware and software controls, excluding minor changes/updates, remained as described in Chapter 2.

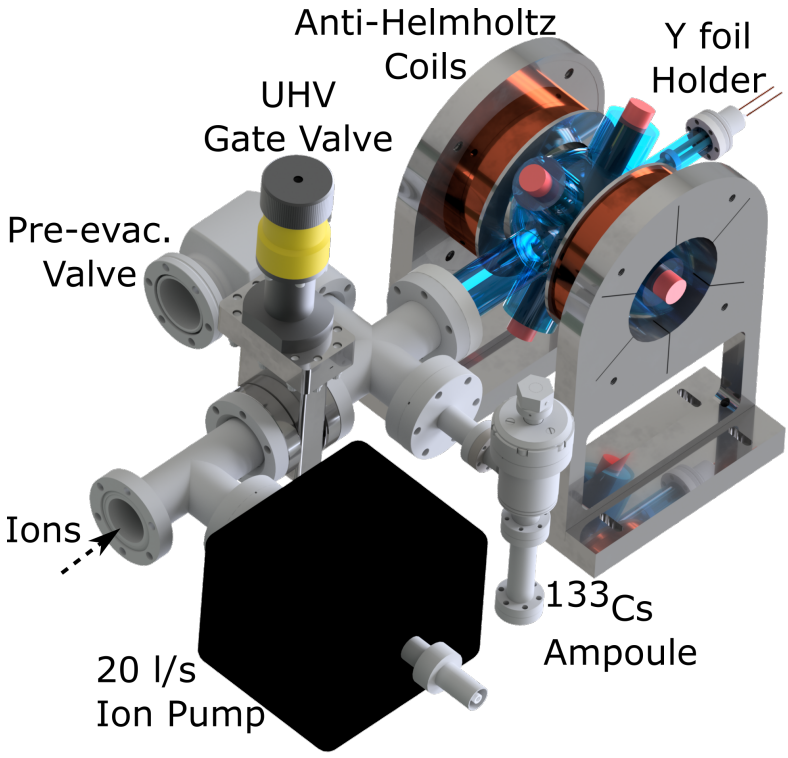

Figure 3.6: A 3D rendered image of the MOT set-up [2]. On the left, the 20 l/s ion pump (Agilent Varian VacIon Plus 20 StarCell) is shown. The next components are a CF40 UHV gate valve, a CF40 valve used for pre-evacuation of the system and a sealed CF16 cylinder containing a ^{133}Cs ampoule. The Cs is isolated from the rest of the system via a CF16 valve shown on the right hand side. Finally, the ions enter the science chamber, and they are implanted into the Y thin foil. The foil is placed 20 mm inside the chamber, and it is supported by a special holder mounted onto a CF16 flange with electrical feedthroughs (neutraliser holder). The coils are placed at both sides of the chamber in an anti-Helmholtz configuration. The red cylinders are marking the path of the laser beams.

The 30 keV ion beam enters the system through a CF40 T-piece, which is connected to a 20 l/s ion pump and a CF40 UHV gate valve. The ion pump is an Agilent Varian Vaclon Plus 20 StarCell, with a pumping speed 20 l/s for N_2, producing a residual pressure of 1×10^{-9} mbar during normal operation conditions. The pump's stray magnetic field, in the vicinity of the ion path (25 cm far from the pump's inlet flange), is considered comparable to the Earth's magnetic field, thus no mu-metal shield was installed. Our assumption was based in the published data included in the pump's manual [79], where already at a distance $\sim$16 cm, the field along its main axis was measured $\sim$700 mG. In addition, during the thorough ion beam alignment procedures, the ion pump had been continuously in operation, thus any potential influence was taken into account.

The CF40 UHV gate valve (see Fig. 3.6) is used to isolate the rest of the MOT set-up from the ion pump and the beam line, reducing drastically the time needed for emergency maintenance procedures. Characteristically, it has been observed that by isolating the chamber and initially exposing it to N_2 atmosphere, the system pressure can range from atmospheric to UHV (10^{-9} mbar) conditions within few hours instead of a few days. During maintenance, the system is pre-evacuated using a 50 l/s turbo-molecular pump temporally connected to the "pre-evac." CF 40 valve. The latter, combined with a leak valve, is used also for venting the system with N_2. A CF16 cylinder, containing 1 g of ^{133}Cs (99.95 % purity, Sigma Aldrich), was installed as an alternative atom supply for development purposes or during the unavailability of the $^{133}Cs^+$ beam. The roles of the science chamber and the anti-Helmholtz coils are described in the following section.

Finally, the cross-piece is connected to the science chamber via a CF40 metal-to-glass connector, which also acts as a support. Further support to the chamber is provided via foam segments placed under the cell's optical windows (the ones aligned along the coil's main axis) and rested on the inside of the mounts (not shown in Fig. 3.6).

3.1.3.1 Science chamber and anti-Helmholtz Coils

The new science chamber was designed by Dr. Luca Marmugi and built by the UCL glassblower. The main purpose of the new design was to account for the neutralisation assembly presented in Section 3.1.3.2 and to increase our trapping efficiency.

The science chamber has 3 pairs of 40 mm diameter optical windows of high quality (40-20 scratch-dig) supported by borosilicate glass tubes, and two metal-to-glass connectors (CF40 and CF16) aligned along the ion's path (see Fig. 3.7). The window-pairs were aligned so to create the optical paths of the counter-propagating laser beams, necessary

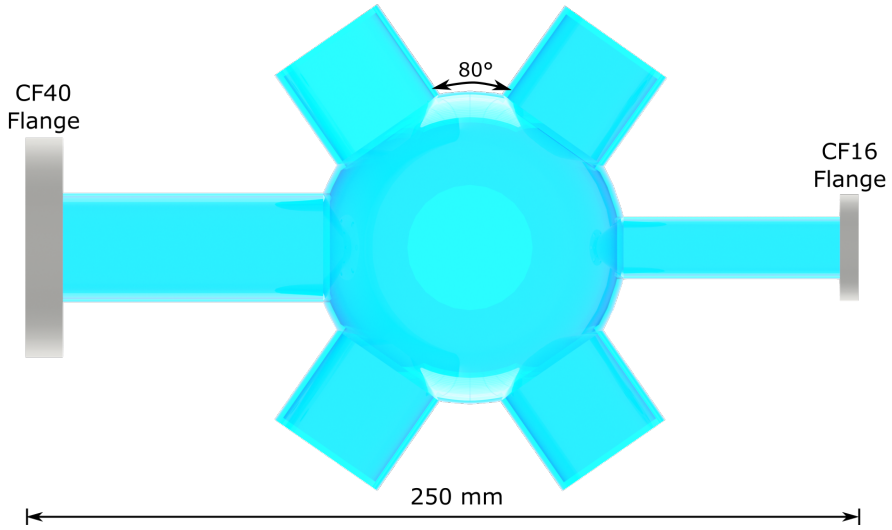

Figure 3.7: A rendered image of the borosilicate glass science chamber of a total length of 250 mm and a ≈100 mm internal diameter. The CF40 and CF16 flanges constitute the connection points to the rest of the beam line and the thin foil system respectively.

for the realisation of the MOT. One pair's axis was placed perpendicularly to the beam line (along the main axis of the trapping coils), while the rest of the two pairs were placed, at a 80° angle to each other, on a plane perpendicular to the axis of the first pair.

The main advantages of the new science chamber are the low attenuation optical windows and the minimisation of the metal surfaces. The former leads to small optical losses/scattering, which in turn increases the efficiency of the cooling mechanisms. In addition, the minimisation of the scattered light in the vicinity of the trapping area improves the sensitivity of our fluorescence imaging system. While a glass-only chamber increases the difficulty and the cost of the manufacturing process in comparison to a metal chamber with glass windows, there is a big advantage when is combined with an anti-adsorption coating. A metal chamber can be also coated, but the forming of coatings on metal surfaces has been experimentally shown to be relatively poor, and the permanent losses of atoms remain high [80]. A detailed analysis of the coating's role will be provided in the next Section 3.1.3.3.

A new system of air-cooled anti-Helmholtz coils was designed and built specifically to be used in combination with the new cell. The coil mounts were designed with 3D Inventor CAD software with specifications based on calculations performed with Wolfram Mathematica. The coils were specifically tailored to produce high magnetic field gradients for low applied currents, while avoiding the use of water-cooling systems. The produced linear magnetic field gradient is 10 G/cm/A in the vicinity of the trap.

The system consists of aluminium coil mounts with a diameter of 92 mm and 400

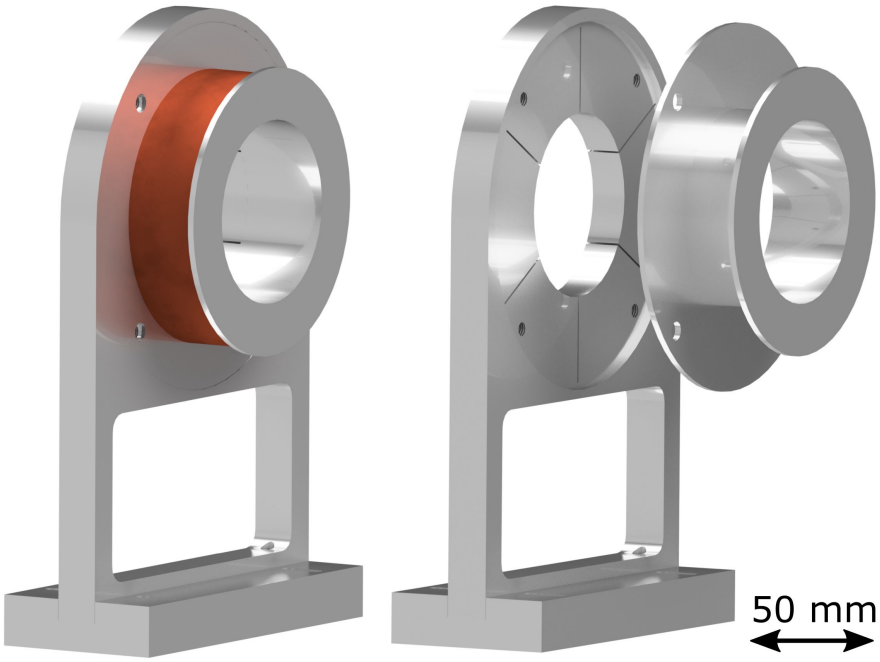

Figure 3.8: A rendered image of the new coil mount used for the trapping coils. The aluminium mount has a 92 mm diameter and supports 400 turns of 1 mm diameter copper wire. Another identical mount was built and installed to create the anti-Helmholtz configuration, producing a linear magnetic field gradient of 10 G/cm/A.

turns of 1 mm diameter copper wire (the 1 mm includes the insulation layer). As shown in Fig. 3.8, special "cuts" were made to the mounts in order to minimise eddy currents during abrupt changes of the magnetic field and to enhance the air-cooling mechanism. The current of the coils is controlled, as described in Chapter 2, by the SRS SIM960 PID combined with the water-cooled MOSFET (IXFN 120N20), and the desired value is set via LabVIEW. Finally, three pairs of mutually orthogonal squared compensation coils are employed to minimise the background magnetic field at the vicinity of the trap and, in case, move the position of the cloud for optimisation purposes.

3.1.3.2 Neutralisation set-up

This section reports on the neutralisation of ions, and specifically on a technique involving the implantation of electrostatically accelerated ions into a cold thin metallic foil, their neutralisation and enhanced, by resistive heating, thermal diffusion as neutral atoms. Representative experimental demonstrations of using thin foil implantation for magneto-optical trapping of radioactive species can be found in Di Rosa et al. [14] (^{135}Cs and ^{137}Cs) and Gwinner et al. [81] (^{79}Rb).

The above technique normally involves foil temperatures $\sim$1000 K, thus potentially creating the conditions for thermal ionisation of the atoms present in the lattice or on the sur-

face of the foil. Thermal ionisation events would result in diffusion of ions into the science chamber instead of neutral atoms. In order to favour the desorption of neutral (implanted) atoms, a metal with work function (the minimum energy required to extract an electron) smaller than the ionisation potential (the energy required to ionise an atom) of the implanted species is chosen. The Langmuir-Saha equation gives the relative concentration of neutral atoms and ions in the gas phase:

$$\frac{n_a}{n_+} = \frac{g_a}{g_+} \exp\left(\frac{I - \Phi}{k_B T}\right), \tag{3.1}$$

where n_a/n_+ is the ratio of ions and neutral atoms present in the metal, g_a/g_+ is the atom-ion statistical weights' ratio, I is the ionisation potential of the implanted species (eV), Φ the work function of the metal (eV), k_B the Boltzmann constant and T the temperature of the foil (K). In our experiment, the target material of choice is yttrium and the ions of interest Cs, hence $g_a/g_+ =$2 for alkali atoms, $I = I_{Cs} =$3.89 eV [82] and $\Phi = \Phi_Y =$3.1 eV [83] for a pure metal. Assuming a temperature of 1000 K for the Y foil (maximum value in operational conditions), only about 1 out of 10^4 diffused particles will be an ion, i.e. $n_a/n_+ \sim 10^4$. Taking into account that normally the foil operates at lower temperatures, $n_a/n_+ \geq 10^4$, corresponding to an amount of ions that can be considered negligible for this type of experiment.

At this point, it has to be noted that the estimation of the above ratio is strongly affected by the value of the work function of the metal, where the latter depends on numerous parameters, including the presence of impurities, surface's structure, mechanical stress levels, temperature etc. [84]. Extra caution is taken during the installation of the Y foil to minimise contamination. The Y foil is kept in the original package under Ar atmosphere for as long as possible, the installation takes place in a clean environment, and the installed foil is slowly baked to increase outgasing (i.e. cleaning from deposited contaminants) under vacuum conditions.

Another potential candidate to be used for neutralisation of Cs is zirconium (Zr), which has been reported to be more robust [85], presents higher extraction efficiency (more atoms being thermally diffused out per heating cycle), has significantly lower vapour pressure than yttrium and to cause less damage to a specific type of dry film (SC-77) [86]. While in our experiment we have not noticed any signs of damage on the PDMS, neither has it been reported from other groups using the same coating [87], systematic and long-term observations in the future will be necessary to make a solid conclusion.

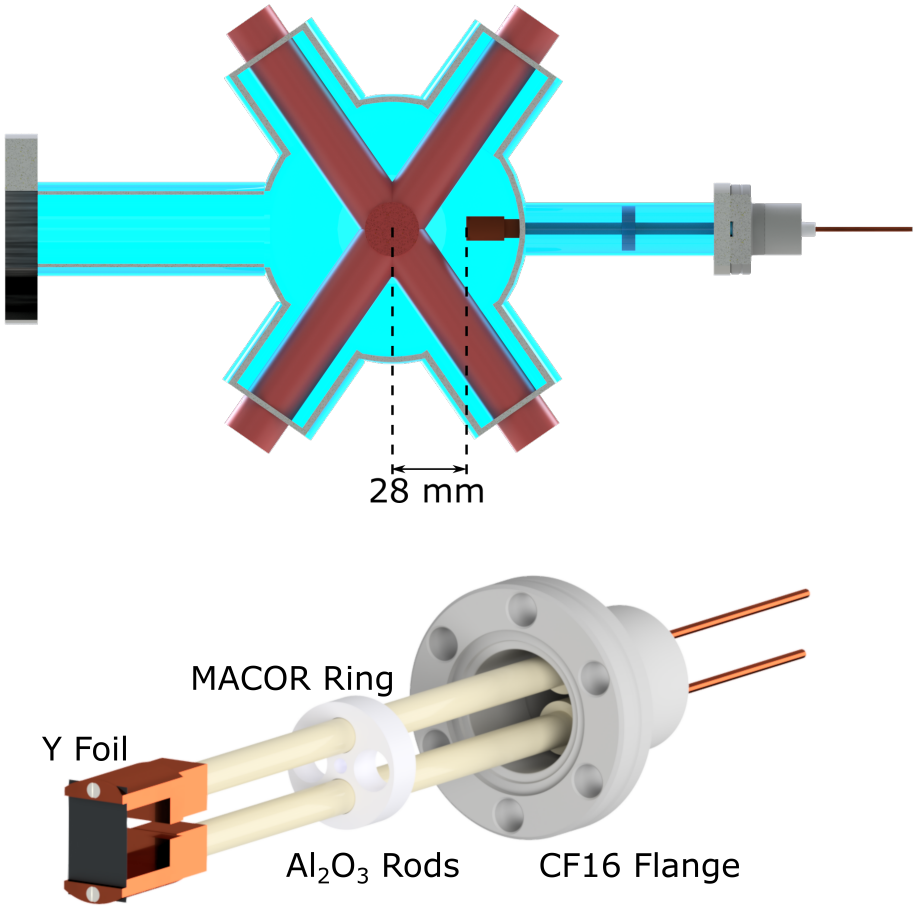

Figure 3.9: The 25 μm thin Y foil is mounted on two copper blocks, which in turn are connected to the CF16 flange's electrical feedthroughs. The aluminium oxide (Al_2O_3) tubes offer mechanical stability to the system, and the MACOR ring keeps the electrodes in place, while protecting the foil from extra stress. The foil is heated up to 1000 K by resistive heating, and its temperature is controlled by regulating the DC current flowing through the electrical feedthroughs. Top: a cross-sectional view of the science chamber revealing the relation of the thin Y foil to the centre of the MOT. Bottom: a detailed sketch of the neutraliser mount. The original design is from Dr. Luca Marmugi.

The accelerated ions are focussed onto a 25 μm thick Y (Alfa Aesar, 99.9 % (REO)) foil, with a surface area of 16$\times$9 mm^2, placed approximately 20 mm inside the science chamber (see Fig. 3.9). The foil is mounted on two Cu blocks, which are electrically connected to the CF16 flange's electrical feedthroughs' (rated up to 20 A) 1.5 mm diameter Cu wires. Two ceramic (Al_2O_3) rods (105.6 mm long), with an embedded hollow Cu core, offer the electrical connection between the foil and the feedthroughs, while ensuring the mechanical stability of the system. The circuit's resistance, as measured immediately after installation, is 1.2(1) Ω, with 0.1 Ω being the statistical uncertainty of the measurements. The 16.5 mm diameter MACOR ring is positioned approximately at the middle of the rods, acting as a centring ring, and minimising potentially catastrophic tensions (e.g. originating from the

thermal movement of the feedthroughs) to be applied to the foil. However, any variations in the foil's length due to temperature changes can be compensated by the mechanical tolerance of the system.

The Y foil, being a metal, could also act as a Faraday cup for the implanted ion beam, and ion current was measured indirectly using a pico-ammeter (same method applied for detecting the signal from standard Faraday cups). During the bombardment with positive ions ($^{133}Cs^{+}$), the interacting Y surface was temporarily positively charged, resulting in the movement of negative charges (electrons) towards the positive region to compensate for the charge difference. By connecting a pico-ammeter to the foil's electrodes (the same used for resistive heating and thermal diffusion), the current could be measured, and it was directly proportional to the ion current impinging on the surface.

3.1.3.2.1 Implantation Depth: simulations with SRIM The SRIM (Stopping and Range of Ions in Matter) software package [88] was used to simulate the implantation depth of $^{133}Cs^{+}$ into the Y foil. The simulations have shown that the 30 keV Cs ions are implanted in the first 500 Å of the metal, and the peak of their distribution appears to be at 150 Å (see Fig. 3.10).

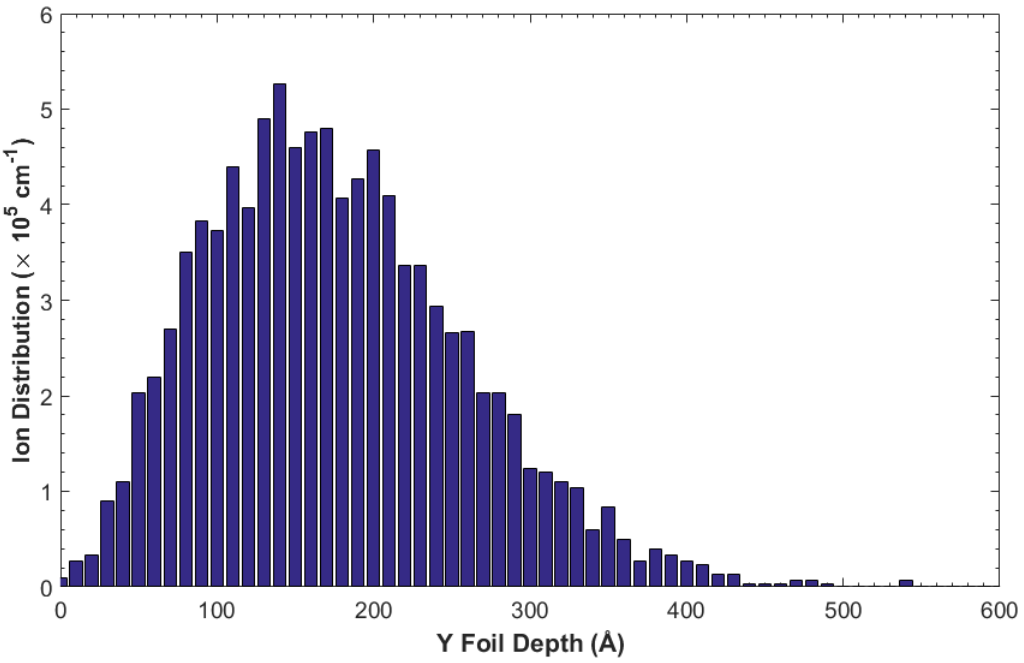

Figure 3.10: Ion distribution in the 25 μm thick Y foil, as it was simulated with SRIM software package, for a 30 keV beam of 10^{4} $^{133}Cs+$ ions implanted into a 100 nm width Y layer. Simulation by Dr. Sami Rinta-Antila.

The ions' acceleration energy and implantation depth, reported here, are significantly larger than the ones included in literature: [87] 3 keV $^{209/210}Fr^{+}$ beam, 5 keV $^{210}Fr^{+}$ beam

and 50 Å implantation depth, while their energy can be considered comparable only in the case of the 20 keV $^{135/137}Cs^{+}$ beam of Di Rosa et al. [14]. The relatively large implantation depth implies a significant participation of the foil's bulk during thermal diffusion, which will become clearer during the following MOT dynamics' analysis.

3.1.3.2.2 Thermal Diffusion: resistive heating The next step, after the implantation and neutralisation of the ions, is their thermal diffusion in the science chamber as neutral atoms. In order to increase the efficiency of the atoms extraction, the foil goes through a series of controlled heating cycles with temperatures, T_Y, up to 10^3 K by applying a DC current, I_{DC}. The kinetic energy transferred from the Y lattice to the adsorbed atoms increases with T_Y, therefore at higher temperatures more atoms are thermally diffused (and eventually trapped) from the surface and the bulk of the foil.

A standard bench DC power supply (AIM TTI EX1810R 10 A) is used to provide I_{DC}, and the T_Y is measured with an optical pyrometer (SensorTherm METIS M3). A large variation (factor 2) of T_Y has been observed for a given I_{DC}, which was attributed to the presence of contaminants acting as barriers (or scattering centres) for the flow of charges, i.e. increasing the resistance of the foil. A hand-held X-ray fluorescence (XRF) system was used to determine the composition of two foils of different origin tested during the development experiments. XRF is a non-destructive analytical technique, where element-specific fluorescent X-rays are recorded and analysed, following the bombardment of a sample of interest with X-rays produced from a primary X-ray source (in this case incorporated in the hand-held XRF system). The first foil, Y_1, was found 96.3 % pure and the second, Y_2, 82.2 %. In fact, I_{DC} =12 A was needed to achieve T_Y ∼1000 K with Y_1, while only I_{DC} =6 A with Y_2 to reach the same temperature.

Atoms being thermally diffused out of the foil at normal operational temperatures (600 K≤T_Y≤1000 K) are too energetic to be captured in a MOT. The use of an organic coating, in our case Polydimethylsiloxane (PDMS) [87], reduces drastically the atomic losses at the cell's walls, allowing the atoms to thermalise without being permanently lost. The desorbed (from the coating) atoms are characterised by a thermal velocity distribution similar to Cs vapour at room temperature, therefore a larger atomic population falls within the MOT's capture velocity range (the low-speed tail of a Maxwell-Boltzmann distribution).

3.1.3.3 Anti-adsorption organic coating: PDMS

The loading rate of a MOT, as defined in Chapter 2, depends on various parameters including the background density and the average velocity of the atomic species of interest

(untrapped atoms). The background density is determined by the competition between the atoms entering and the ones lost from the system. Atoms entering the science chamber are removed via three ways: pumping, chemisorption, and physisorption at the system's walls. Pumping refers to the removing of untrapped atoms by the installed pump (i.e. ion pump), together with other atoms/molecules present in the vacuum system as a background gas. Chemisorption describes the permanent loss of an adatom (adsorbed atom) by chemically reacting with the walls (steel-vacuum components or Pyrex chamber). The adsorption energies involved in chemisorption processes are in the range of a few eV [89]. Physisorption is the non-permanent "sticking" of an atom on a surface, held by weak van der Waals forces, and can be quantified by the time, τ_s, spent by the atom on the surface:

$$\tau_s = \tau_{el} \exp\left(\frac{E_a}{k_B T}\right), \tag{3.2}$$

where τ_{el} ($\approx 10^{-12}$ s^{-1}) [90] the interaction time for a pure elastic collision, E_a the kinetic energy required for an atom to diffuse out from the surface, k_B the Boltzmann constant and T the temperature of the surface in K. The E_a ranges from 10^{-2} eV [91] for coated surfaces to 10^{-1} eV [80] for glass and a few eV [92] for metals. In experiments with stable species, atoms are produced in large numbers and losses can be easily compensated. In stark contrast, radioactive atoms are available in finite amounts, and the system's efficiency needs to be maximised.

Efforts on reducing pumping related losses focus on designing relatively small-aperture cells or/and on blocking the exit holes (apertures) during the trapping process as demonstrated by Aubin et al. [93]. The complete isolation of the pump from the rest of the system during trapping could be a potential solution (e.g. by the rapid activation of a pneumatic valve) [94], but interrupting the continuous pumping is followed by accumulation of background gas (e.g. originating from outgassing of the inner surfaces) that would increase the background collisions and eventually decrease the capture efficiency of the MOT. An approach based on the above technique would need to carefully consider the timing between the opening and closing of the pumping aperture in order to retain a high trapping efficiency.

Coating the walls with chemically inert substances (organic coatings) is a widely implemented technique. The organic coating deposited on the Pyrex walls lowers the average adsorption energy, E_a, from some eV to a fraction of an eV. This ensures that the likelihood of chemisorption - and therefore permanent loss of atoms - is significantly reduced. As a consequence, the efficiency of the cell is enhanced. In addition, thanks to the small yet finite sticking time τ_s that an atom spends on average in the coating, thermalisation of the

high-energy atoms diffused from Y foil is obtained. In detail, atoms at high temperature (roughly, T_Y =1000 K) interact with the PDMS coating (kept at room temperature) for an average time τ_s before being released in the vapour phase. During this process, they dissipate a large fraction of their residual kinetic energy, ultimately producing a vapour with a velocity distribution compatible with room temperature. We note that this is a fundamental step to achieve efficient trapping in the MOT, given its typical capture velocity of $\sim$30 m/s. A chain of atom-PDMS interactions can be described as the atom bouncing inside the cell. Following Monte Carlo simulations and experimental observations, Aubin et al. [93] report that the number of bounces, N_b, for an uncoated surface is $N_b \approx 1$ (i.e. the atoms are almost certainly permanently adsorbed), while for a coated cell $N_b \approx 100$ depending on the coating's quality, chemical composition and the cell's geometry (i.e. the size of the pumping/exit apertures). This proves that atoms have time to dissipate their energy and can interact many times with the laser beams. This increases the probability of a given atom to be trapped.

The most common coatings in the literature, used for atom trapping, are paraffins (alkanes) (e.g. Paraflint) and siloxanes (e.g. PDMS). Siloxanes and paraffins are also characterised by low outgassing rates, i.e. the rate atoms/molecules are leaving the surface in a gaseous phase, making them ideal for UHV conditions. An extensive study on wall coatings, including a detailed report on their adsorption energies and outgassing rates, is provided from Stephens et al. [80].

The coating of our choice is PDMS - $CH_3[Si(CH_3)_2O]_nSi(CH_3)_3$, a siloxane widely used in atomic physics and other fields. The particular coating was chosen due to its small adsorption energy ($\sim$0.1 eV [95]), small outgassing and reaction rates [80] (reporting values for similar coatings), and the possibility to be used in combination with LIAD (Light-Induced Atoms Desorption [96]), a technique that can increase the loading rate of a MOT by desorbing atoms weakly bound on the coatings surface. Specifically, PDMS has been previously successfully used to directly increase the efficiency of experiments involved in laser cooling and trapping of ^{209,210}Fr [87], ^{85}Rb [97] and here for ^{133}Cs [2].

3.1.3.3.1 The application of PDMS: deposition procedure A detailed description of the PDMS deposition procedure in the science chamber, followed in our experiment, has been published in Giatzoglou et al. [2]. The procedure presented here and in [2] is a modified version of Agustsson et al. [87]. The PDMS with viscosity of 65 cSt was purchased from Sigma-Aldrich. The procedure can be divided in three stages: cleaning, coating's deposition and curing.

Cleaning: A solution of CH_3OH, C_2H_5OH, and KOH in a volume of 0.45:0.45:0.10 is prepared for cleaning the inner surface of the Pyrex science chamber. During the preparation, and specifically at the introduction of the KOH, extra caution is taken due to the strong exothermic reaction to keep the temperature of the solution below $\sim$40 °C. The above is realised by stirring continuously and gently the solution, while introducing KOH in small intervals. The liquid is then poured into the chamber, and a prolonged cleaning is performed. The next step is the removal of the solution together with any contaminants by rinsing the chamber five times with de-ionised water, a standard procedure followed for the preparation of UHV components. The chamber is left to dry in a fume hood for 30 minutes. The residuals of the cleaning solution are further removed by evacuating the chamber with a turbo-molecular pump (50 l/s), reaching a base pressure of 10^{-6} mbar and then baking. The system is baked with resistive heating tapes to enhance outgassing. In detail, the chamber is thoroughly covered with tapes and three Al layers to ensure homogeneous heating, and to thermally isolate the chamber-tapes system from the environment. A final temperature of 120 °C is acquired by increasing 10 °C per 20 minutes. The heating continues until the base pressure, 1×10^{-7} mbar, is achieved. The tapes are then turned off, and the chamber is allowed to cool down under vacuum conditions via spontaneous thermalisation with the environment.

Coating's deposition: A solution of 5% PDMS and 95% $(C_2H_5)_2O$ (ether) is deposited on the inner surface of the chamber by spin-coating (0.1 rps). The spinning continues for $\sim$5 minutes, and then the excess solution is removed. As next step, the chamber is baked to remove the solution and allow the thin film (thickness $\sim\mu$m [96], [98], [99]) of PDMS to correctly adhere on the Pyrex surface. The same baking procedure as described above is followed, with the difference that the temperature goes up to 100 °C in order to avoid damages of the coating. Subsequently, the coated chamber is installed in the vacuum line and another baking (up to 100 °C) is performed, this time to remove adsorbed particles (potentially introduced during the installation procedure). A baseline pressure of 1×10^{-9} mbar is obtained in around 24 hours.

Curing: The curing or passivation is considered one of the most critical parts of the whole process, and can be defined as the saturation of the coating's surface with Cs (or other alkali) atoms. Even with the low reacting rates of the PDMS, chemisorption is still present, and the coating needs to be exposed to stable (readily available in large quantities) Cs and allowed to react/passivate. Passivation describes the filling of the majority of chemisorption sites with stable alkali atoms, thus minimising the future losses of radioactive

species. Following the passivation, mainly physisorption effects are present with energies $\sim 10^{-1}$ eV. We passivate the coating by inserting stable Cs vapour (^{133}Cs) and monitoring the progress of the MOT population. When the number of trapped atoms is maximum and stable, the coating is considered cured. The need for re-curing after some time of operation due to coating's degradation from hot particles [100] (e.g. coming from a hot neutraliser or an oven) has been reported.

3.2 MOT characterisation: fluorescence imaging

In the first experimental phase (see Chapter 2), the MOT is fully characterised using absorption imaging. For the current stage, we implemented an additional method relying on real-time detection of the fluorescence signal produced from the MOT during excitation/de-excitation cycles. The above method, namely *fluorescence imaging*, offers a reliable and direct measurement of the MOT population, and it can be also utilised to calculate the density distribution, the temperature of the cloud and for spectroscopic studies [6]. Fluorescence imaging has been our main detection tool during the facility's development and characterisation experiments. The real-time fluorescence imaging is advantageous in comparison to the absorption technique, and in particular for tuning/optimisation procedures and investigation of the MOT dynamics.

A PixelFly USB camera, combined with a commercial objective lens (PENTAX C2514-5M 25mm 1:1.4), collects the light coming from the MOT. An 852 nm interference filter, with full width at half maximum (FWHM)$=$10 nm, is installed immediately after the objective to reduce the background light, without affecting the fluorescence light emitted from the trapped atoms. A pinhole of 1.6 mm diameter is placed in front of the interference filter to further reduce the background and increase the imaging sensitivity. The system is placed on top of the science chamber, and the cloud is imaged through the Pyrex glass.

A LabVIEW programme equipped with all the necessary controls is used for controlling the experiment and live monitoring of the MOT population, N_{MOT}, the cloud's size and the intensity of the trapping light. The programme actively subtracts the background, decoupling in that way the laser power fluctuations from changes in the N_{MOT} and compensating for the former. During long monitoring ($\sim$1 hour) measurements, an average background level $\sim$20 atoms was measured, with 3 % fluctuations.

3.2.1 Fluorescence signal calibration

The MOT population, N_{MOT}, is given by:

$$N_{MOT} = \frac{N_c}{\eta T_c \Omega \Gamma_{sc} t_{exp}}, \tag{3.3}$$

where N_c is the number of the counts detected at the CCD camera, η the sensor's quantum efficiency, T_c is the transmission coefficient for the current imaging configuration, Ω the solid angle, Γ_{sc} the scattering rate and t_{exp} the exposure time of the sensor.

The scattering rate is calculated as:

$$\Gamma_{sc} = \frac{\Gamma}{2} \frac{\frac{6I}{I_s}}{1 + \frac{6I}{I_s} + 4\left(\frac{\Delta}{\Gamma}\right)^2}, \tag{3.4}$$

where Γ is the natural line width for the $6^2S_{1/2}$ to $6^2P_{3/2}$ transition, I the intensity for each of the MOT beams, I_s =2.7 mW/cm^2 the saturation intensity for unpolarized light resonant with the F =4 to F' =5 transition [25] and Δ the detuning of the cooling beams.

The solid angle of our imaging system is calculated as:

$$\Omega = \frac{\pi}{4}\left(\frac{F}{D f_n}\right)^2, \tag{3.5}$$

where F is the focal length of our objective, f_n is the f-number given by the focal length divided by the diameter of our aperture, d, and D the distance MOT-aperture. The solid angle of our system with F =25.4 mm, D =72 mm and d =1.6 mm is: Ω =3.878$\times$10^{-4} sRad.

Parameter	Symbol	Value	Unit
Natural line width	Γ	3.282$\times$10^7	Hz
Detuning	Δ	$-$8.7$\times$10^7	Hz
Solid angle	Ω	3.878$\times$10^{-4}	sRad
Cooling intensity per beam	I	4.67	mW/cm^2
Transmission coefficient	T_c	0.915	arb.
Sensor's quantum efficiency	η	35.5	%

Table 3.1: Parameters used for calculating the number of atoms via fluorescence imaging.

The quantum efficiency, η, of the CCD sensor is given by the ratio of the CCD counts, N_c, to the number of photons, $N_{photons}$, arriving at the sensor: $\eta = N_c/N_{photons}$. In order to measure η for our PixelFly, the camera's CCD sensor was exposed to laser light of known wavelength and power for different exposure times t_{exp}. The data were linearly fitted, and

the fit was used to extrapolate the CCD counts to 1 second exposure. By converting the laser power to number of photons per second, and dividing this with the CCD counts per second, the quantum efficiency of our camera was calculated as: η =35.5%.

The parameters included in Table 3.1 have been inserted in the LabVIEW imaging programme, and by using Eq. 3.3, the MOT population was actively calculated.

3.3 Characterisation of the facility: MOT from $^{133}Cs^{+}$ beam

The building of the facility and the development of the necessary tools for characterising its operation were followed by performing off-line tests. $^{133}Cs^{+}$ ions were routinely produced in the surface ionisation source, described at the beginning of the chapter (see Fig. 3.2), accelerated and routed to our set-up. The ions were implanted into the Y foil, thermally diffused to the science chamber, thermalised at the organic coating and successfully trapped in a MOT. The $^{133}Cs^{+}$ current impinging onto the foil ranged between 10^{-9} to 10^{-12} A. The ion current was measured at many points along the beam line using Faraday cups (lower detection limit $\sim 10^{-12}$ A), with the last two beam diagnostics being the Faraday cup shown in Fig. 3.5 and the neutraliser foil.

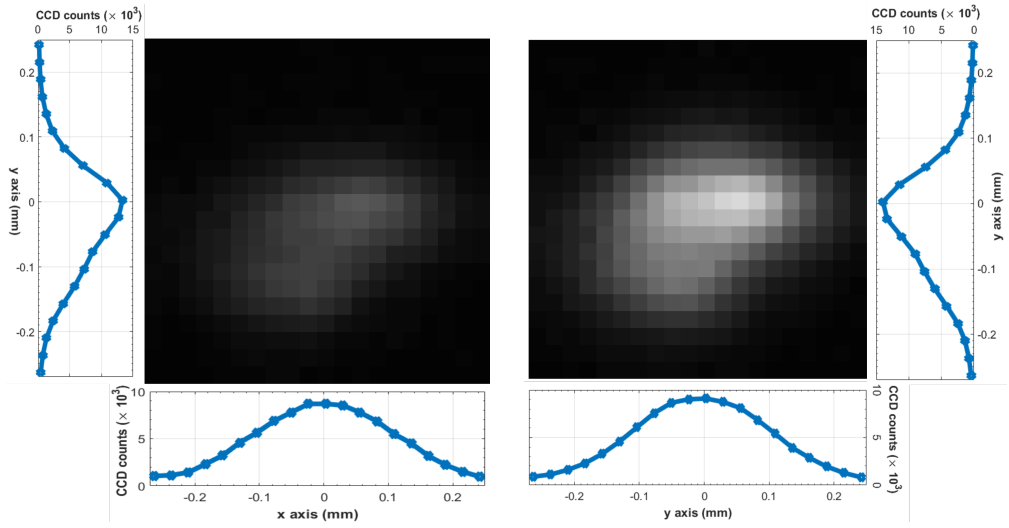

Figure 3.11: Fluorescence images of the MOT, in grey scale, indirectly loaded from the $^{133}Cs^{+}$ beam. The ions were previously implanted into the foil with an average current I≈10^{-10} A, and neutral atoms were thermally diffused at a later stage by heating the foil. The exposure time of the CCD camera was 2 seconds. (a) N_{MOT} =(675 ±20 atoms) at T_Y =908 K. (b) N_{MOT} =(1672 ±20 atoms) atoms and T_Y =931 K. Inset: the CCD counts distribution in space, i.e. MOT profiles on the x and y axes.

The laser cooling and trapping approach for the ^{133}Cs remained as described in Chapter 2, i.e. the transition $6^2S_{1/2}F$ =4 to the $6^2P_{3/2}F'$ =5 was used for cooling, and the $6^2S_{1/2}F$ =3 to the $6^2P_{3/2}F'$ =4 for locking the repumper laser. The average cooling

intensity per beam was 4.67 mW/cm^2, and the optimum detuning for this configuration was found to be at -2.65Γ. The average intensity for each beam of the repumper was 1.1 mW/cm^2. Two possible MOT loading mechanisms were observed during the second experimental phase: loading from freshly or previously implanted ^{133}Cs$^+$ and the conventional loading from ^{133}Cs vapour. The vapour was available when necessary by opening the CF16 valve, as it was described in Section 3.1.3. During operational conditions, when the foil was at room temperature (negligible thermal diffusion), the ion beam blocked and the CF16 valve closed, no trapped atoms were detected. In Fig. 3.11, fluorescence images of the MOT loaded from previously implanted ^{133}Cs$^+$ are shown at different yttrium temperatures, T_Y. In this example, increasing T_Y by 23 K (or °C) increases the MOT population by 997 atoms. An average temperature of 150 $\pm$10 μK and 10^{10} cm^3 density was typically measured via absorption imaging in a separate experiment, however the above numbers can show significant variations depending on the experimental conditions.

At this point it has to be noted that the high currents produced in the off-line source, I_{max} =10^{-9} A, are orders of magnitude higher than the common production rates of unstable beams from fission ($\sim 10^{-15}$ A which roughly corresponds to 10^4 ions/s). Nevertheless, the physics behind the neutralisation, thermalisation and trapping processes remain unchanged for both stable and unstable species, and one can estimate (by scaling down) the response of the facility in the case of radioactive Cs produced from fission. Before proceeding with the on-line tests and the implantation of unstable Cs, a full characterisation of the facility's operation using the ^{133}Cs$^+$ beam was achieved, and it is presented in the following sections.

3.3.1 Diffusion and trapping: slow and fast dynamics

The loading of the MOT from implanted ^{133}Cs$^+$ was realised by increasing the temperature of the Y thin foil. Normally, temperatures above 700 K ($T_Y \geq$700 K) were necessary in order for the thermal diffusion process to start having an effect on the real-time N_{MOT}. For a given temperature, the gain in N_{MOT} was found to be strongly dependent on the implantation "history" of the foil. As expected, foils that have been through multiple heating cycles are depleted, and the number of diffused atoms can be significantly lower in comparison to the case of a freshly implanted foil. Depletion, in this context, refers to the removal of adatoms from the surface and the bulk of the metallic foil.

Two processes/mechanisms can be identified behind the loading of the MOT from the hot Y: a process characterised by fast dynamics consistent with diffusion of atoms previ-

ously adsorbed and neutralised on the surface of the foil (or/and in the first atomic layers), and a slow dynamics process consistent with the dominant contribution from atoms in the metal's bulk. The dynamics of the above two mechanisms are illustrated in Fig. 3.12.

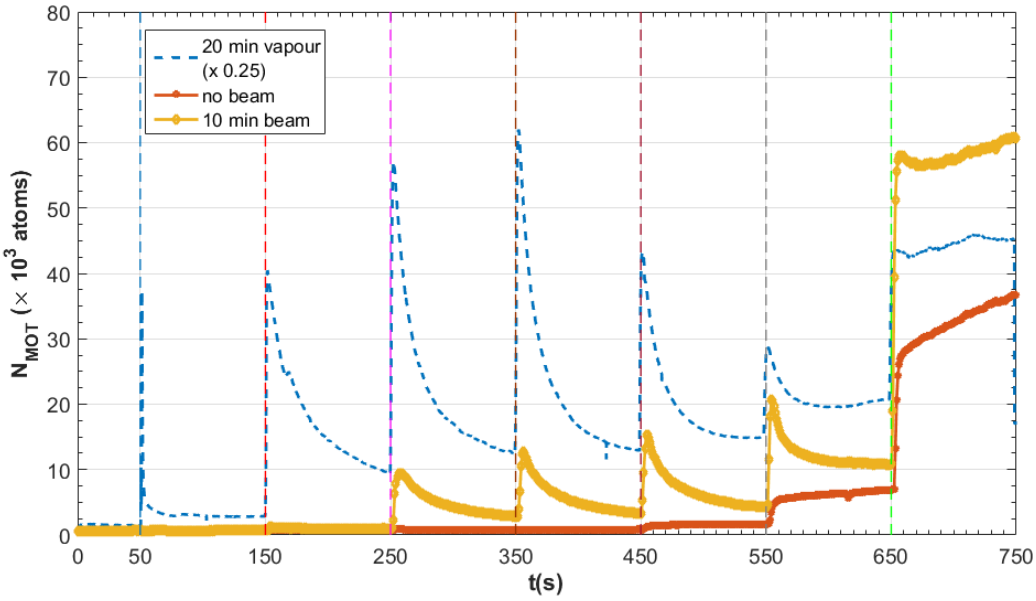

Figure 3.12: The comparison of the MOT's loading from Cs vapour (dashed line) and from the Y foil (solid lines) reveals some important differences. The measured values from the vapour loading were scaled down by a factor 4 for clarity purposes. Differences appear also between loading from a freshly implanted foil (yellow continuous line) and from a partially depleted foil (red continuous line). The current of the foil, I_{DC}, was increased in steps of 0.5 A every 100 s, starting from t=50 s and I_{DC} =3.5 A (691 K) resulting in T_Y (from the left): 691, 767, 832, 887, 931, 972 and 1010 K.

In the first dataset (dashed line) shown in Fig. 3.12, the Y foil has been exposed to Cs vapour at a density $\sim 10^{10}$ cm^{-3} for 20 minutes, while being kept at room temperature prior to the increase of the T_Y. The fluorescence signal measured during the heating of the vapour-prepared foil is characterised by fast dynamics, and specifically a spike in the MOT population takes place in the first seconds after each heating step, which consistently decays to a N_{MOT} value higher than the starting level. The abrupt increase (spike) of the MOT population is consistent with the release of atoms adsorbed on the surface of the foil [101]. The higher N_{MOT} level is a direct indication of the PDMS's effectiveness, since the presence of an organic coating, as discussed in Section 3.1.3.3, increases the average number of bounces of an atom in the science chamber prior to its permanent removal (e.g. due to pumping or chemisorption losses). With the increase of the time that a diffused atom spends in the chamber, the probability to be trapped in the MOT increases (i.e. higher N_{MOT}). Moreover, with the increase of the temperature, the surface atoms are depleted, and eventually no fast dynamics are observed (for T$\geq$1010 K in this example).

At t≈600 s, the slow increase in the MOT population (slow dynamics) can be attributed to deeper layers (bulk) of the foil participating in the diffusion process. Specifically, at high temperatures, the previously implanted and neutralised $^{133}Cs^{+}$ in the bulk of the foil are more energetic (due to energy transfer from the "hot" lattice) in comparison with atoms in the bulk at low temperatures, hence they have higher probability to diffuse out. The diffusion rate of atoms from a solid and its dependence on the temperature are well expressed by the Arrhenius equation:

$$D = D_0 \exp\left(-\frac{E_a}{k_B T_s}\right), \tag{3.6}$$

where D (m^2/s) is the diffusion coefficient, D_0 (m^2/s) the maximum value, E_a the desorption energy or the energy required for the atoms to diffuse out, k_B the Boltzmann constant and T_s the temperature of the solid in K.

When the chamber is isolated from the vapour and only the ion beam acts as an atom supply, the loading behaviour shows remarkable differences. In the case of a pre-implanted foil (red continuous line in Fig. 3.12), which has already gone through heating cycles and has not been exposed to vapour, there is no presence of fast dynamics, which is consistent with the depletion of surface adatoms. In contrast, the slow dynamics dominate, and already at $T_Y \geq 931$ K the contribution to the MOT population can be observed.

As shown in Fig. 3.10, a portion of the 30 keV $^{133}Cs^{+}$ beam is implanted into the first layers of the foil, while the peak of the ions seems to appear at ∼150 Å. Indeed, fast dynamics (consistent with surface adatoms) are also present in the case of a freshly implanted foil (yellow continuous line in Fig. 3.12), but orders of magnitude lower compared to the fluorescence signal in the vapour case. On the other hand, the slow dynamics appear again, and they result in a MOT population almost double in comparison to the "no beam" case. The dataset produced with the freshly implanted foil at an average ion current I≈1×10^{-10} A and shown in Fig. 3.12, constitutes a clear example of the $^{133}Cs^{+}$ beam contribution to the MOT population, both via the surface and the bulk implanted atoms.

3.3.2 Loading from pre-implanted foil

The amount of atoms diffused out from a previously implanted foil depends on two main parameters: the temperature of the foil and the concentration levels of the implanted and neutralised ions, with the latter increasing with the implantation duration (see Fig. 3.14). By heating and therefore depleting the foil for long enough time to enhance diffusion, the effects of the implantation "history" can be minimised, hence the contribution of the freshly implanted ions can be quantified.

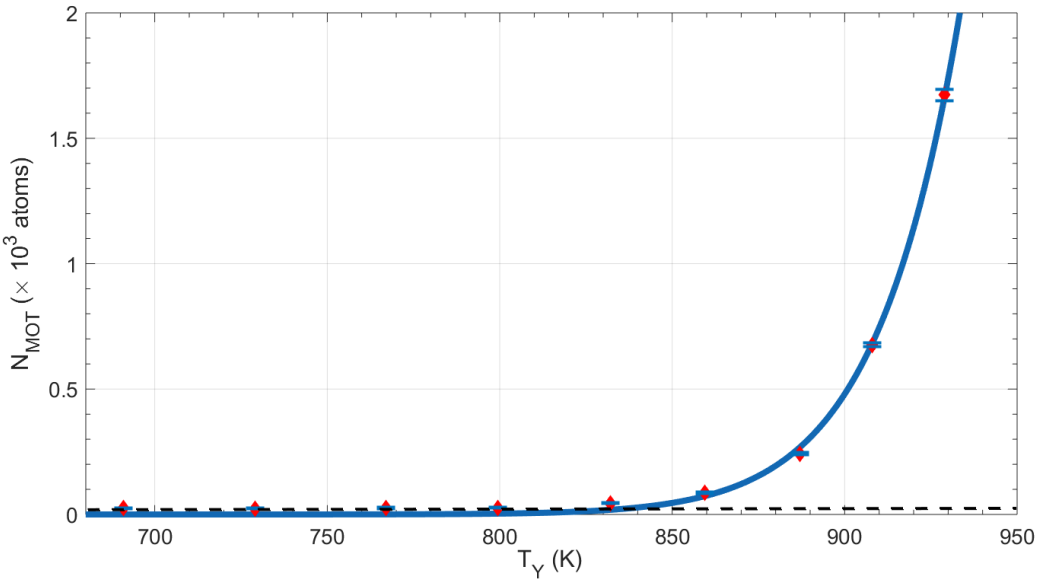

Figure 3.13: The MOT population, N_{MOT}, for different Y temperatures, T_Y. The Y foil was previously implanted with $^{133}Cs^+$. For $T_Y \leq$800 K (4.25 A), no MOT can be detected and the measured signal is comparable to the background. The blue line is a fit based on Arrhenius equation (Eq. 3.6) for desorption. The dashed black line represents the background noise level during the measurements.

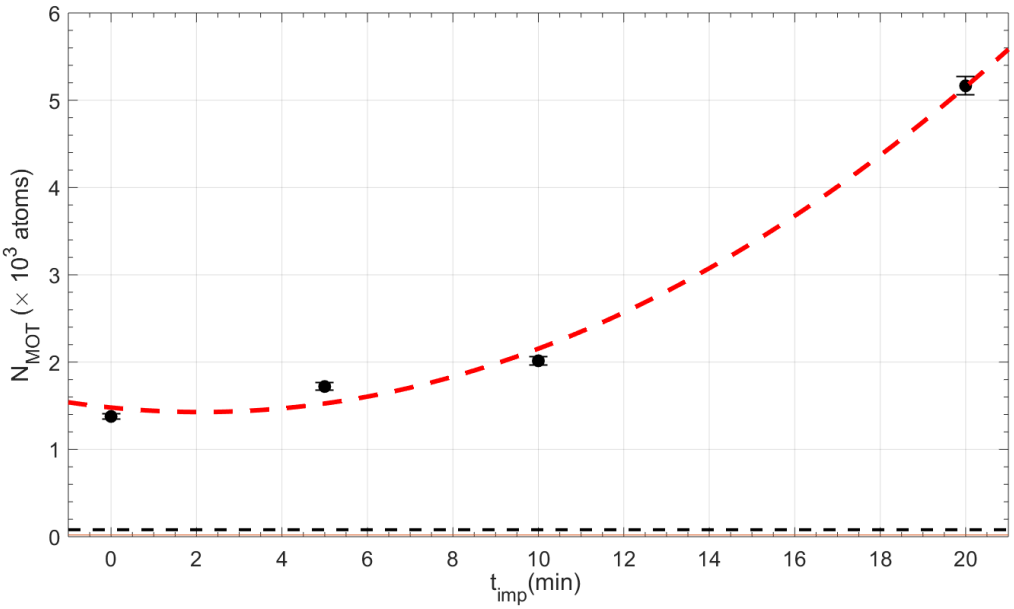

Figure 3.14: The N_{MOT} versus different implantation times for T_Y =930 K. At t_{imp} =0, the trapped atoms originate from previous implantation runs performed using the same foil. The quadratic fit (red dashed line) is there to guide the eye. The dashed black line represents the background noise level during the measurements.

In Fig. 3.13, the N_{MOT} versus T_Y is plotted for a previously implanted foil with $^{133}Cs^+$. One can notice the complete absence of vapour contribution and the slow exponential increase of the MOT population. The data seems to be in a good agreement with the Arrhenius equation (Eq. 3.6), describing the desorption of atoms across a solid [102].

In order to investigate the dependence of the MOT population on the number of the atoms in the foil, $^{133}Cs^{+}$ were implanted with different durations, t_{imp}, at an average current of 10^{-10} A and the results are plotted in Fig. 3.14. The increase of the N_{MOT} with the implantation duration, for a given temperature T_Y =930 K, is clearly illustrated. The above observation implies that the number of diffused atoms depends also on the concentration of atoms in the foil and subsequently on the duration of the implantation.

3.3.3 Direct loading from the $^{133}Cs^{+}$ beam

Loading the MOT from a pre-implanted foil can be considered efficient when it involves stable or long-lived species. In Chapter 4, the use of a pre-implanted foil towards the trapping of ^{135}Cs, with half-life $T_{1/2}$ =2.3×10^6 years, is reported. In stark contrast, when short-lived species are involved, for example the ^{140}Cs with $T_{1/2}$ =63.7 s, the acceleration of the whole procedure is necessary. In this section, I report on results from the direct loading of the MOT from freshly implanted ions. The following results constitute further validation of the facility's operation and the compatibility of the 30 keV beam.

A representative example of the effect of freshly implanted ions at a rate of 10^{-10}A on the MOT population is provided in Fig. 3.15a. For this measurement, the Y foil is heated up to a chosen temperature, the MOT mechanism is activated (magnetic field gradient is turned on), and after the N_{MOT} from previously implanted ions becomes stable, the $^{133}Cs^{+}$ beam is turned on for 300 s. During this time, the N_{MOT} increases (with a delay ∼5 s), and following the blocking of the ion beam, decays to an N_{MOT} value higher than the starting level (again, indication of PDMS's effectiveness). The contribution of the ion beam is significant, not only, when the MOT population is below the detection threshold (no MOT is detected), but also when a MOT of ∼3000 atoms is present (from pre-implanted ions). It is worth noting that the MOT's population during implantation at low T_Y (691 K) remains almost steady, while at higher temperatures (≥832 K) there is a constant increase. A threshold ∼800 K (e.g. in Fig. 3.13) was indeed identified, after which contribution from the bulk is observed. This becomes clearer in Fig. 3.15b, where a larger range of Y temperatures is shown. The contribution to N_{MOT} increases with temperature, which is consistent with atoms being thermally diffused out from the foil.

The results presented in Fig. 3.16 are the outcome of a separate experimental approach to decouple the contribution of freshly implanted from pre-implanted ions. In this approach, before the start of the implantation, the MOT (when present) is subtracted as a background (easily achievable via the LabVIEW imaging programme), thus in principle any

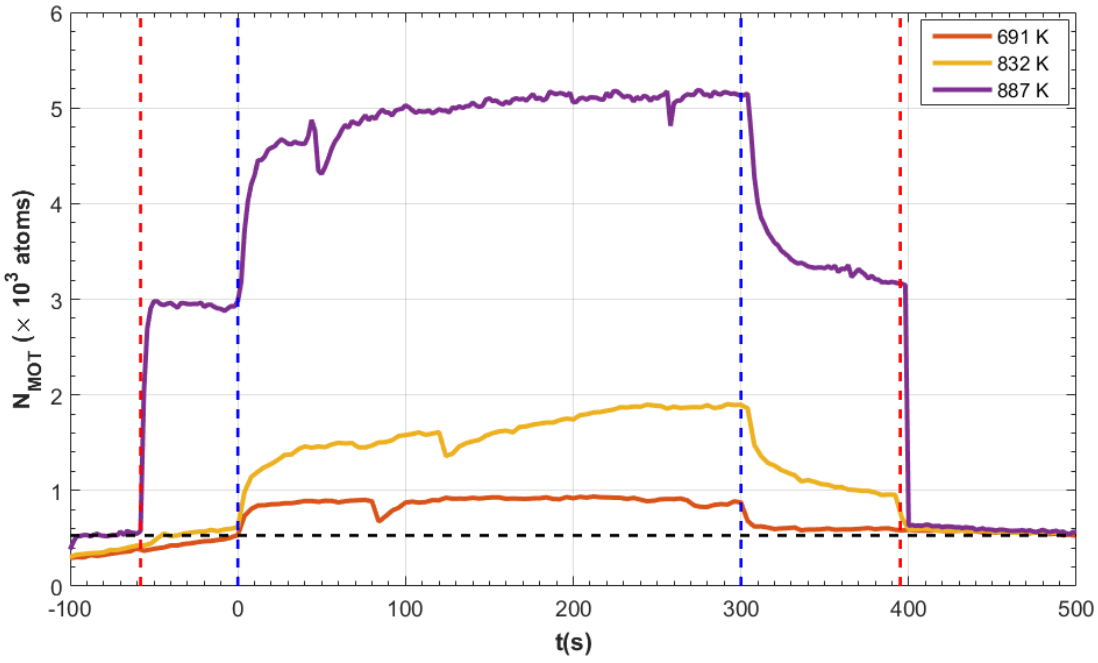

(a)

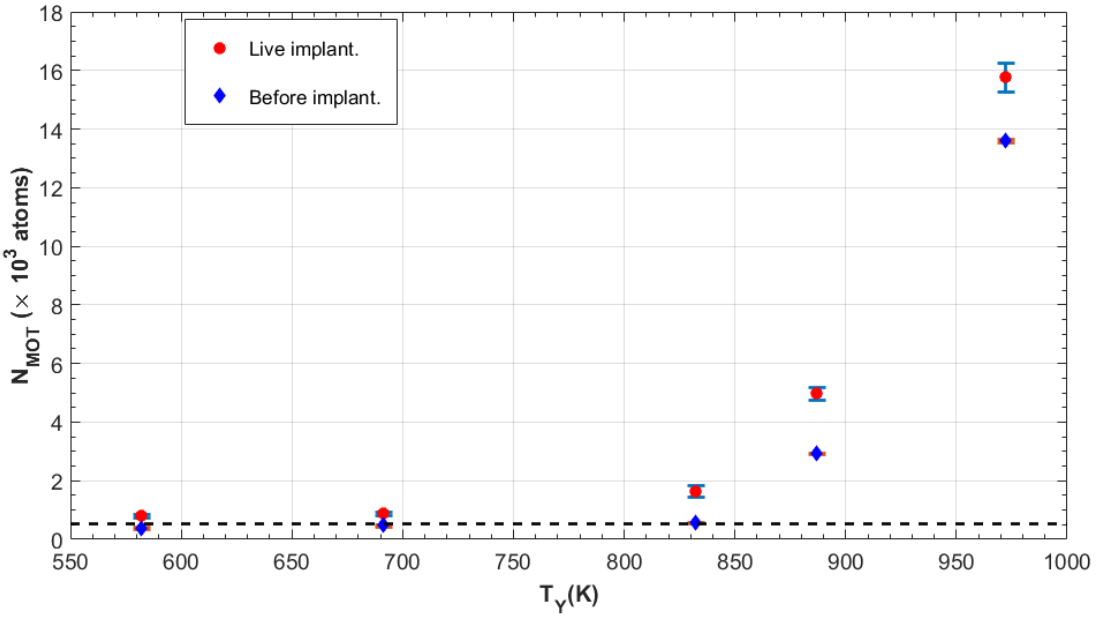

(b)

Figure 3.15: Evidence of the direct loading from the $^{133}Cs^{+}$ beam at an average current I≈10^{-10}A. (a) The red dashed lines represent the time that the magnetic field is turned on and off (i.e. initiation/end of trapping). In the case of T_Y =887 K, a MOT of approximately 3000 atoms is achieved from pre-implanted ions. The blue dashed lines (t=0 s and t=300 s) indicate the ion beam implantation's start and end respectively. The effect of the freshly implanted ions to the MOT population is clear in low, 691 K, and high, 887 K, temperatures. The dips in the MOT population are believed to be oscillations in the incoming ion current. The presence of those oscillations has been independently verified by performing long-term measurements of the ion current produced by the off-line ion source and efforts have been made to minimise them. The horizontal dashed line represents the detection level during this set of measurements. (b) The contribution of the ion beam to the N_{MOT} increases with temperature for $T_Y \geq$ 832 K.

signal detected after starting the implantation is due to freshly implanted ions. Similarly to the data presented in Fig. 3.15, the thermal diffusion seems to start for T_Y =767 K and increase with the temperature. The decrease in N_{MOT} for T_Y =972 K is attributed to higher background pressure (i.e. increased one-body collisions) due to the high temperature of the neutraliser, thus the enhanced outgassing from the foil and its surrounding surfaces.

It is worth commenting that for T_Y ≤691 K the contribution from the ion beam is constant, even when the foil is at room temperature. The aforementioned behaviour is consistent with sputtering [103] (also present in Fig. 3.15), where pre-implanted atoms (neutralised ions) are ejected from the surface of the foil due to the 30 keV ion-bombardment. Sputtering phenomena have not been reported before during cold-atom experiments involving thin foil implantation, potentially due to the lower ion energies used in those studies.

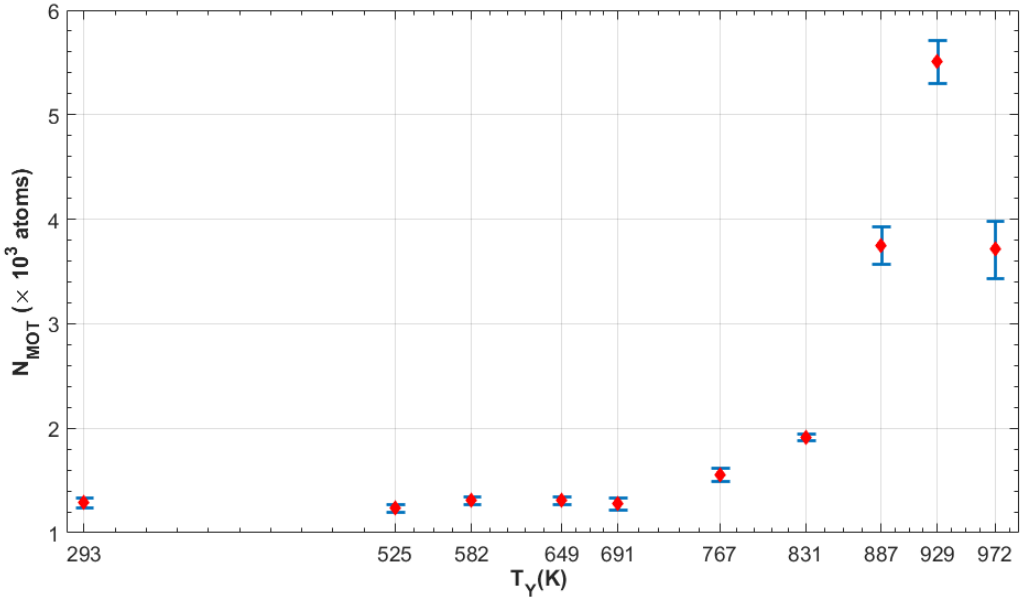

Figure 3.16: Evidence of the direct contribution of the $^{133}Cs^+$ ions at an average current I≈10^{-10}A starting from N_{MOT} =0. The figure is similar to Fig. 3.15b, with the difference that the background MOT from previously implanted ions is removed, using LabVIEW, before each measurement (thus the starting N_{MOT} =0). For T_Y ≤ 691 K, the MOT population is believed to originate mainly from sputtering phenomena.

The data presented in Fig. 3.16 can be used to estimate a lower bound to our system's trapping efficiency. In particular, for T_Y =929 K and an average ion current, I≈10^{-10} A corresponding to 6×10^8 atoms, the gain in the N_{MOT} from the ion beam is approximately ΔN =5500 atoms. We consider an average MOT lifetime, τ =2.85 s, measured in a different experiment, and a loading rate R =6×10^8 atoms assuming diffusion and neutralisation efficiencies equal to 1 (unlikely, thus the calculated value is considered a lower bound).

The estimation of our trapping efficiency's lower bound is calculated as follows:

$$\eta \geq \frac{\Delta N}{R}\frac{1}{\tau} \approx 3 \times 10^{-6}. \tag{3.7}$$

It has to be noted, that this number constitutes only an estimation, and more accurate calculations will be performed after the installation of preciser beam diagnostics in the near future.

Chapter 4

Towards ^{134,135}Cs trapping

In this chapter, I report on the preparation work for trapping radioactive ^{134,134m,135,135m}Cs, as well as on preliminary results obtained before the completion of this thesis. In detail, the hyperfine splitting (hfs) of ^{134,135}Cs were calculated based on published spectroscopic data, the laser system was tuned in order to match the frequencies needed for laser cooling each isotope, and on-line tests with fusion-evaporation products with mass 134 (A=134) and fission fragments with A=135 took place. Gamma-ray spectra from implantation runs with A=135 are shown (see also Giatzoglou et al. [2]) together with some preliminary results of a ^{135}Cs MOT.

4.1 Hyperfine splitting and isotope shifts of unstable Cs

The hfs frequency shifts were calculated for ^{133,134,135}Cs (Table 4.1) to prepare our laser system for trapping of the corresponding species. Eq. 1.5, described in Chapter 1, was used for calculating the total frequency shifts for each of the three Cs isotopes, based on published spectroscopic data of the magnetic dipole constant, A_{hfs} and electric dipole constant, B_{hfs}. For an overview on determining the atomic hyperfine structure, one can see [26]. The table also includes the updated values of the D_2 optical transition frequencies, ν, where the isotope shifts, $\delta\nu$, for ^{134}Cs and ^{135}Cs have been taken into account.

Fig. 4.1 shows the frequency shifts reported in the Table 4.1 on the Cs D_2 hyperfine structure, for clarity, and to demonstrate the dependence of the laser frequencies needed for trapping (ν_c and ν_r in Fig. 4.1) on the hfs frequency shifts. The hyperfine structure of the D_2 line of ^{133}Cs was previously published in [25] and of ^{135}Cs in [14], and their values are in a complete agreement with the ones reported here.

The hfs of ^{134,135}Cs were calculated, and subsequently the laser frequencies needed for trapping them, based on published values for the A_{hfs}, B_{hfs} and $\delta\nu$. Specifically:

	^{133}Cs	^{134}Cs	^{135}Cs
ν (MHz)	351725718.50(11)	351725751.6(2.5)	351725682.1(2.0)
	[104]	[104] [105]	[104] [105]
$\delta\nu$ (MHz)	0	33.1(2.5)	$-$36.4(2.0)
		[105]	[105]
ν_1 (MHz)	$-$5170.8554(exact)	$-$5818.68(1)	$-$5469.764(9)
	[26]	[105] [106]	[107] [108]
ν_2 (MHz)	4021.7764(exact)	4654.944(8)	4254.260(7)
	[26]	[105] [106]	[107] [108]
ν_3 (MHz)	$-$339.7128(18)	$-$354.5(1.1)	$-$354.90(32)
	[27]	[107]	[107] [108]
ν_4 (MHz)	$-$188.4885(11)	$-$215.12(56)	$-$200.66(16)
	[27]	[107]	[107] [108]
ν_5 (MHz)	12.7985(86)	0.645(49)	9.88(15)
	[27]	[107]	[107] [108]
ν_6 (MHz)	263.8906(12)	320.14(83)	280.92(22)
	[27]	[107]	[107] [108]

Table 4.1: The D_2 optical transition frequencies, ν, the isotope shifts, $\delta\nu$, and the hfs frequency intervals, $\nu_{1,2,3,4,5,6}$, for ^{133,134,135}Cs. The uncertainties in the frequency shifts were calculated using the standard error propagation formula for independent parameters taking into account the uncertainties in A_{hfs}, B_{hfs} and C_{hfs} (only for the ^{133}Cs case).

1. A_{hfs} and B_{hfs} for the $S_{1/2}$, as they were calculated and reported in Thibault et al. [105], based on the data published in the Fuller et al. review [106]. In Fuller et al. [106], the gyromagnetic ratio (g/g^{133}) of the $S_{1/2}$ for the ^{134,135}Cs (among others) is reported, based on measurements by the atomic-beam magnetic-resonance method in Stroke et al. [109]. The gyromagnetic ratio is then used for calculating the A_{hfs} and B_{hfs} of the radioactive species.

2. The A_{hfs} and B_{hfs} for the $P_{3/2}$ from Ackermann et al. [107]. Ackermann et al. measured the $P_{3/2}$ hyperfine constants for ^{131,132,134,136}Cs by the level crossing method, and reported the work of Svanberg et al. [108] using the same method for ^{133,135,137}Cs. The values reported in Ackermann et al. are updated in comparison to [108], since they include a more accurate g_j-factor [110].

3. Finally, the isotope shifts, $\delta\nu$, as they were published in Thibault et al. [105]. Thibault et al. [105] measured the isotope shifts and the hyperfine interaction constants for a chain of Cs isotopes ($^{118-145}$Cs) by collinear high-resolution laser spectroscopy on a

fast beam.

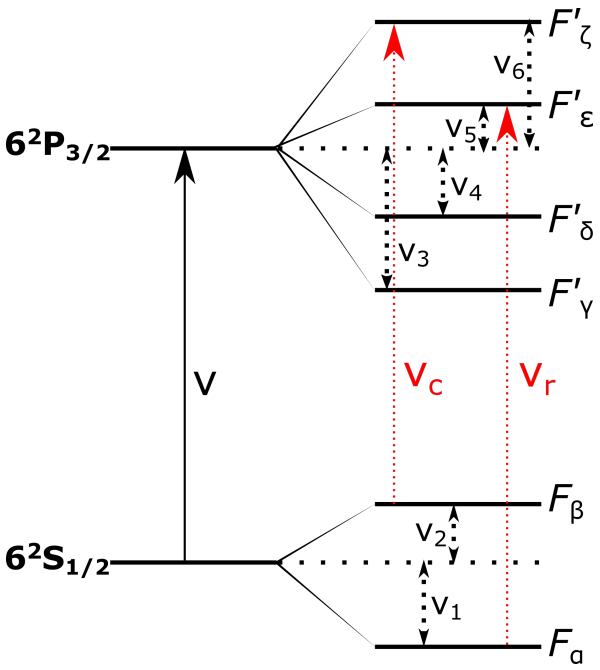

Figure 4.1: Cs D_2 hyperfine transition. The hfs frequency intervals, $\nu_{1,2,3,4,5,6}$, are shown, and their representative values for each Cs isotope are included in Table 4.1. The ν_c and ν_r indicate the cooling and repumper transitions, while ν is the D_2 optical transition frequency for each isotope (taking into account $\delta\nu$). The values of the total angular momentum, F, for ^{133,135}Cs with I =7/2 are: α =3, β =4, γ =2, δ =3, ϵ =4 and ζ =5. For the ^{134}Cs with I =4: α =7/2, β =9/2, γ =5/2, δ =7/2, ϵ =9/2 and ζ =11/2. The diagram is -not- to scale (i.e. the distance ratio between levels does not represent the ratio of their frequency intervals).

The measured values of the A_{hfs} and B_{hfs} for the ^{134,135}Cs from [105] are similar to what is reported in [107], [106], but they come with a higher uncertainty. Characteristically, for the hyperfine level $6^2P_{3/2}F'$ =4, the frequency shift is 11.7(1.6) MHz when A_{hfs} and B_{hfs} are taken from Thibault et al. [105], and 9.88(15) MHz when the data come from Ackermann et al. [107].

Di Rosa et al. [14] successfully trapped ^{135}Cs and ^{137}Cs by tuning their lasers according to spectroscopic data published in Ackerman et al. [107], Fuller et al. [106] and Thibault et al. [105]. The differences between our data included in Table 4.1 and data reported in Di Rosa et al. [14], are the updated numbers for the ^{133}Cs based on the precise measurements in [27] (published after [14]) and the hfs frequency shifts of the ^{134}Cs. The former results in very small differences in the ^{135}Cs hfs, while the latter to the best of our knowledge, have not been reported before.

It is worth noticing that in Di Rosa et al. [14], there was no attempt for more accurate spectroscopy on the D_2 line of the ^{135,137}Cs, and only sub-megahertz differences were reported from the calculated frequency values. To date, the published spectroscopic data

for Cs have been verified only for the ^{135}Cs and ^{137}Cs, while the rest of radioactive isotopes still need to be trapped.

4.1.1 Preparing the laser system for Cs isotopes

Using the frequency and isotope shifts included in Table 4.1, our laser system was re-designed in order to match the needed frequencies for the trapping of ^{134}Cs and ^{135}Cs. The following general formula was used:

$$\nu_{c/r} = (\nu_F^{133} - \nu_F^A) - (\nu_{F'}^{133} - \nu_{F'}^A) + \delta\nu, \tag{4.1}$$

where $\nu_{c/r}$ is the cooling/repumper's laser frequency shift with respect to the frequency used for trapping ^{133}Cs, ν_F the frequency shift of the ground state hyperfine level, $\nu_{F'}$ the shift of the excited state and $\delta\nu$ the isotope shift. The above formula was used for both, ^{134}Cs and ^{135}Cs (i.e. A=134/135 in Eq. 4.1), and can be applied for any Cs isotope. In the case of ^{135}Cs, Eq. 4.1 gives $\nu_c = -252$ MHz and $\nu_r = +263$ MHz, and for the ^{134}Cs, $\nu_c = -544$ MHz and $\nu_r = +669$ MHz. The above values, since they are relative to the frequencies used for the trapping of ^{133}Cs, have the same nominal detuning, Δ, from the cooling transition: -13.6 MHz or -2.65Γ (Γ is the natural line-width of the D_2 line).

With an approach similar to the experimental arrangement presented in Chapter 2, Section 2.1, a series of AOMs was introduced in order to tune the cooling laser for each isotope. In terms of hardware, the main difference with respect to the first experimental phase is the addition of a double-pass AOM (AOM2) in the cooling laser's spectroscopy branch. The repumper laser was tuned with a MOGLabs MWM wavemeter, with a relative frequency accuracy of 10 MHz. The repumper laser system did not include an amplification part (e.g. MOPA) during the measurements, therefore the AOM-related power losses were avoided.

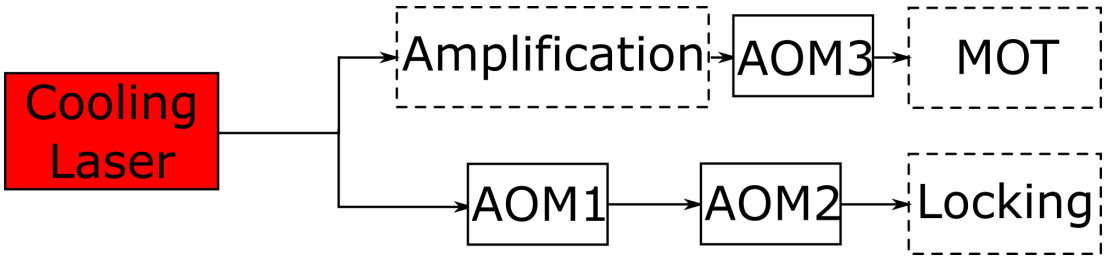

Figure 4.2: Diagram showing the steps followed for the detuning of the cooling beam. The AOM1 and AOM2 are 110 MHz and 80 MHz AOMs in a double-pass configuration, while AOM3 is an 80 MHz AOM used as a single-pass. The locking part uses DAVLL system, and the amplification section is a MOPA, as described in Section 2.1. By the use of a combination of polarising beam splitters (PBS), the AOM2 could be bypassed when necessary.

In Fig. 4.2, the steps followed for the tuning of the cooling laser are shown. By selecting the right AOM set-points and locking the laser on the ^{133}Cs D_2 line hyperfine transition of our choice, the frequencies calculated using Eq. 4.1 and data from Table 4.1 are matched. In the following Table 4.2, the AOMs' frequencies (set-points), the locking positions and the total relative shift in the cooling laser's frequency used for each isotope are included.

Steps	^{133}Cs	^{134}Cs	^{135}Cs
AOM1 DP(MHz)	(-1) 95.9	$(+1)$ 113.4	$(+1)$ 110
AOM2 DP(MHz)	$(+1)$ 79.9	$(+1)$ 79.9	bypassed
Locking point	4 $\rightarrow$ 4,5	4 $\rightarrow$ 4	4 $\rightarrow$ 4,5
AOM3 SP(MHz)	$(+1)$ 79.9	$(+1)$ 79.9	$(+1)$ 79.9
Total shift(MHz)	0	-544.1	-252

Table 4.2: The locking points and the AOMs' set-points used for each isotope. The total shift refers to the cooling laser's relative frequency shift, ν_c, with respect to the ^{133}Cs case (thus for ^{133}Cs the total shift is 0). The values of the total relative shifts match nicely with the calculated relative shifts in the cooling frequency, ν_c, needed for each isotope. The order of the AOM's diffraction pattern is indicated in brackets. This also serves as a multiplier for the frequency shift.

The AOM1 and AOM2 are in a double-pass (DP) configuration, thus to calculate the actual frequency shift, the reported value included in the Table 4.2 needs to be multiplied by a factor 2. The AOM3 is in a single-pass (SP) configuration and the reported value is the actual frequency shift. Another key point to mention is that the frequency shifts, as a result of the contribution of AOMs in the spectroscopy branch (AOM1 and AOM2), which is the lower branch shown in Fig. 4.2, have the same amplitude but of the opposite sign impact on the laser's frequency of the upper branch, which goes to the MOT. To elaborate further, we can think of an example in which the cooling laser beam is detuned by $+400$ MHz (total contribution of AOM1 and AOM2) and then is locked on the $F = 4 \rightarrow F' = 5$ transition. In that case, and since the two branches are separated before the two AOMs, the light that is going to the amplification part (upper branch) will be -400 MHz far from the $F = 4 \rightarrow F' = 5$ transition. After the amplification part, the cooling laser's frequency of the upper branch is further shifted by the AOM3 prior to its arrival to the MOT area.

The total relative shift in the cooling laser's frequency is matched with the calculated values, included in Table 4.2, for both ^{134}Cs and ^{135}Cs. The effect of the combination of the AOMs and the different locking points on the cooling laser's frequency for the trapping of ^{133,134,135}Cs is shown in Fig. 4.3. The zero of the y-axis (in Fig. 4.3) is the cooling laser's frequency when is resonant with the $F = 4 \rightarrow F' = 5$ transition of the ^{133}Cs D_2 line. We

can notice that the endpoint frequency of the ^{133}Cs is -13.6 MHz or -2.65Γ detuned from the aforementioned transition, as it was anticipated before. In addition, we label the laser's relative frequency shifts for the trapping of ^{134,135}Cs with respect to the endpoint frequency of the ^{133}Cs.

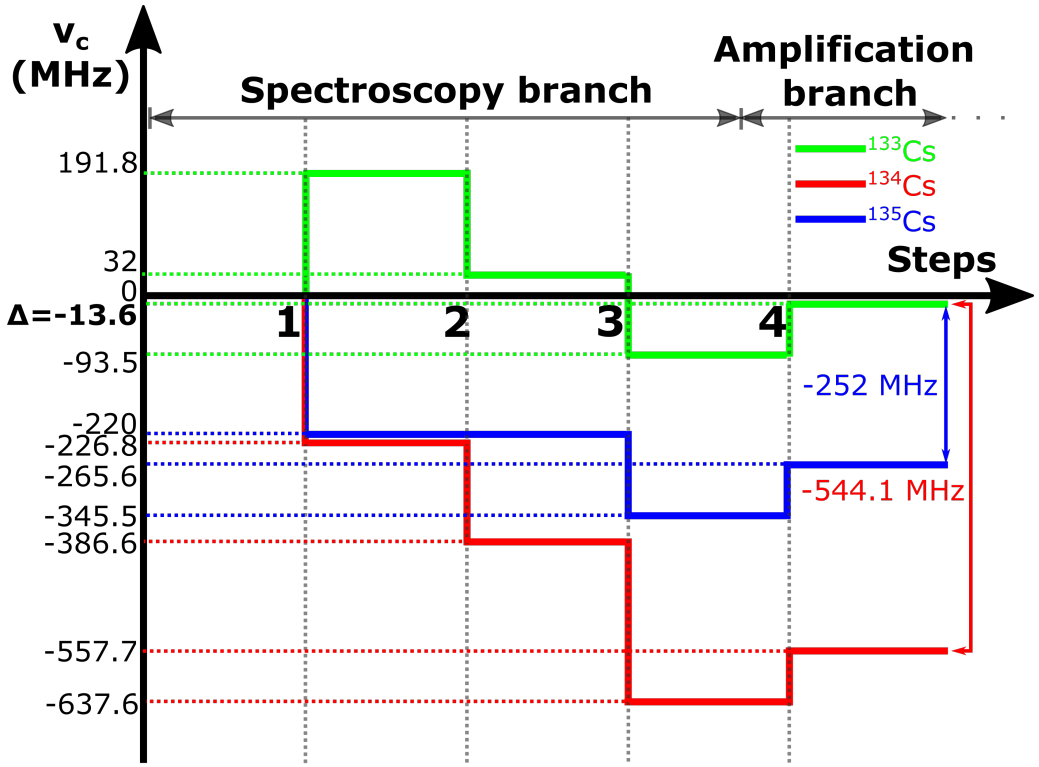

Figure 4.3: The sketch shows the cooling laser's frequency (ν_c) with respect to the $F = 4 \rightarrow F' = 5$ hyperfine transition (i.e. the zero of y-axis) of the ^{133}Cs D_2 line versus the tuning steps. The steps 1, 2, 3 and 4 are: AOM1 DP, AOM2 DP, locking point and AOM3 SP, respectively. The sketch is based on the numbers reported in Table 4.2. The ^{133}Cs endpoint frequency is shown to be -13.6 MHz or -2.65Γ detuned from the $F = 4 \rightarrow F' = 5$ transition. The ^{134}Cs and ^{135}Cs endpoint frequencies are -544.1 MHz and -252 MHz, respectively, far from the ^{133}Cs endpoint frequency.

4.2 On-line tests: production and implantation of radioactive beams

Neutron-rich Cs isotopes were produced via light-ion fusion-evaporation and fission reactions, during separate experimental phases, induced by a primary proton beam from the K130 cyclotron. The proton beam impinged upon a suitable target in the IGISOL target area, and the proton-induced nuclear reactions' fragments were accelerated, mass-separated and routed to our science chamber. The nuclear reaction (fission or fusion-evaporation), target material, primary proton beam's energy and intensity were chosen

based on the Cs isotope of interest. Reaction products with A=134 and A=135 were implanted into our Y foil.

4.2.1 ^{134}Cs

The ground state, ^{134}Cs, with a nuclear spin J^{π} =4^{+}, has a half-life $T_{1/2}$ =2.0652(4) years, and the isomeric state, ^{134m}Cs, has J^{π} =8^{-} and $T_{1/2}$ =2.912(2) hours [111]. As discussed in Section 1.1, ^{134}Cs is an important tool in nuclear forensics (although not present in weapon fallouts), while high-precision spectroscopy on its ground and isomeric states will provide preciser spectroscopic data, and potentially shed light on effects such as charge radii anomalies. The ^{134g,m}Cs are produced via thermal neutron capture reactions of ^{133}Cs with a relatively high cross-section (30.3(1.1) barn for the ground and 2.6(1) barn for the isomeric state [112]), fission and fusion-evaporation reactions. The fission yield is known to decrease close to stability, and specifically for Cs, the peak of the yield appears for N=139 (^{139}Cs), while for ^{134}Cs it's almost negligible (see for example [113]). In addition, ^{134}Cs cannot be populated by any other fission product via beta decay because ^{134}Xe is stable (hence beta decay stops there). At this stage, during which our facility depends exclusively on the accelerator for the supply of radioactive Cs, the fusion-evaporation reaction becomes the only candidate. ^{134}Cs from thermal neutron capture could be a potential solution in the future.

Proton bombardment of a natural Barium, ^{nat}Ba, target can produce ^{134}Cs via a:

$$^{137}Ba + p \rightarrow ^{134g,m}\ Cs + \alpha$$

fusion-evaporation reaction (or equivalently ^{137}Ba(p,α)^{134g,m}Cs). Natural Ba targets have the following isotopic composition: ^{138}Ba (72%), ^{137}Ba (11%), ^{136}Ba (8%), ^{135}Ba (7%), ^{134}Ba (2%) and ^{133,132}Ba ($<$1%) [114]. Cross-section simulations with the Talys simulation software by Dr. Tommi Eronen (University of Jyväskylä) for a ^{nat}Ba target gave approximate cross-section values of 3 mbarn for the ground state and 1.5 mbarn for the isomeric state. The simulations showed that the cross-sections gain their maximum value and then stabilise for primary beam energies $\geq$ 30 MeV. It is worth mentioning that both cross-sections would increase by a factor $\sim$3 for an enriched ^{137}Ba target. However, difficulties in acquiring the enriched samples prevented this approach from reaching the testing stage. Alternative solutions are being investigated.

4.2.1.1 Towards the ^{134}Cs MOT

A barium fluoride, $^{nat}BaF_2$, target was bombarded at an average primary beam intensity of 10 μA with 30 MeV protons, and the reaction products were accelerated to IGISOL's mass separator magnet. Prior to the implantation of the mass-separated reaction products with A=134, the transport efficiency was optimised using a stable isotope Xe beam (^{129}Xe or ^{134}Xe). The Xe beam was produced by bleeding natural Xe into the He buffer gas, where the primary beam ionised it, and the ions were extracted, accelerated and mass-separated. The Xe ion beam current was measured with Faraday cups at multiple positions along its path and at the Y foil. A maximum transport efficiency ≈30% from the electrostatic beam switchyard to the Y foil was deduced. We note that the Y foil acts as a Faraday cup, thus the 30% constitutes an approximation and not a precise calculation.

The yield of ^{134}Cs was indirectly measured by measuring the beta-decay from ^{134}La and ^{17}F with a silicon (Si) detector positioned in the switchyard region. Si detectors are semiconductor devices detecting incident charged particles (e.g. electrons/positrons) by measuring the electron-hole pairs created. The ^{134}La, with $T_{1/2}$ =6.45(16) min, decays with an intensity of 100% by electron capture (and emission of β^+) to ^{134}Ba [111]. The ^{17}F, with $T_{1/2}$ =69.49(16) s, decays via β^+ decay (100% intensity) to ^{17}O [115]. The ratios ^{134}Cs/^{134}La and ^{134}Cs/^{17}F were estimated with Talys cross-section simulations. Based on the Si detector measurements in the switchyard -which is currently the last radiation detector towards the Y foil, and by taking into account the 30% transport efficiency, an average of 50 $^{134}Cs^+$/s implantation rate was estimated for the ground state. The rate for the isomer was smaller approximately by a factor 2 (also in this case based on Talys simulations).

The cooling and repumper lasers were initially tuned according to the frequency shifts relative to the ^{133}Cs reported in Section 4.1.1: cooling laser's shift, $\nu_c = -544$ MHz, which already includes the -2.65Γ detuning from resonance, and repumper laser's shift, $\nu_r = +669$ MHz. The cooling laser was scanned $\pm$10 MHz or ≈2Γ from the starting ν_c value and the repumper $\pm$50 MHz (around the $\nu_r = +669$ MHz) in order to account for any potential deviations from the calculations. The majority of the measurements took place for high Y foil temperatures, T_Y >800 K, to enhance thermal diffusion. The total cooling power was 120 mW and the repumper's 13 mW. There was no detection of MOT fluorescence. Our conclusion is that for the current system, the *calculated* 50 $^{134}Cs^+$/s implantation rate (without any direct instrumental confirmation) was too small to allow any trapping. In the future, other supply alternatives are investigated aiming to maximise the number of ^{134}Cs

in the science chamber. For the ^{134m}Cs, no alternative to fusion-evaporation has been identified yet (due to its short half-life), therefore it is possible that a similar experiment will be repeated in the near future after upgrading the facility. Upgrades that could lead to the achievement and detection of a ^{134m}Cs (or/and ^{134}Cs) MOT are: addition of beam diagnostics/radiation detectors (e.g. Si detectors) further down the transport line and closer to the science chamber, improved trapping efficiency and increased imaging sensitivity.

4.2.2 ^{135}Cs

The ground state, ^{135}Cs, with a nuclear spin J^{π} =7/2^{+}, has a half-life $T_{1/2}$ =2.3(3)$\times$10^{6} years, and the isomeric state, ^{135m}Cs, has J^{π} =19/2^{-} and $T_{1/2}$ =53(2) min. The ground state decays via beta decay (100% intensity) to ^{135}Ba, and the high-spin isomer decays, either via internal conversion (α $\approx$4% [116]) or via emission of two gamma photons. In detail, the isomer first decays to an intermediate level (J^{π} =11/2^{+}) via an M4 transition emitting an 846.1 keV γ-photon with 95.6% intensity and to the ground state (^{135}Cs) via an E2 transition and emission of 786.8 keV γ-photon (99.7% intensity) [116]. In Section 1.1, it was described that the ^{135g,m}Cs are of a particular scientific interest: the isomeric state could be the key for coherent gamma-ray generation, while the ground state is already an important tool in nuclear forensics. Similar to the case of the ^{134g,m}Cs pair, high-precision spectroscopy on both the ground and isomeric states will extend our spectroscopic knowledge, and potentially aid in the exploration of interesting phenomena like charge radii anomalies.

The isomer and the ground state are produced via fission and fusion-evaporation reactions and with thermal neutron capture. The possibility of producing ^{135g,m}Cs via a ^{138}Ba(p,α) ^{135g,m}Cs fusion-evaporation reaction was evaluated, and Talys simulations by Dr. Tommi Eronen gave the following maximum values for the cross-sections: $\approx$7 mbarn for ^{135}Cs and 2 mbarn for ^{135m}Cs, at 23 MeV proton beam energy. In this particular case, no enrichment of the Ba target would be necessary since the ^{138}Ba is the most abundant (72%). Typical yields in IGISOL for (p,n) reactions are of the order of 50 ions/s/mbarn/μA, which would give around 350 ^{135}Cs^{+}/s/μA and 100 ^{135m}Cs^{+}/s/μA. On the other hand, the estimated number from fission of a natural Uranium (^{nat}U) target, bombarded with 25 MeV protons, is 2500 ^{135g,m}Cs^{+}/s/μA. The latter is significantly larger than the calculated value for the fusion-evaporation case. Additionally, the ^{135m}Cs fission yields had been previously measured in IGISOL by gamma-ray spectroscopy, and a rate of 9000 ^{135m}Cs/s for a 10 μA proton beam was measured. Therefore, it was concluded that the production of

^{135g,m}Cs via proton-induced fission of an ^{nat}U target is the best approach.

To verify the previous reported yields of ^{135m}Cs, a ^{nat}U target was bombarded with a 30 MeV proton beam at intensities up to 6 μA, and implantation test runs with the proton-induced fission fragments of mass A=135 took place. The tests were also important to validate the production, transport, mass separation and implantation processes with one of the species of interest. Gamma-spectroscopy was used to identify and quantify the composition of the ion beam.

4.2.2.1 Gamma-ray spectra: "live" beam

Proton primary beam with 30 MeV energy impinged upon a ^{nat}U target, and the fission products with mass A=135 were routed to the electrostatic switchyard's focal plane. The radioactivity in the ion beam can be monitored via the Si detector (mentioned in the ^{134}Cs implantation test), which, in this case, measures the β radiation or it can be deflected to the spectroscopy line for γ-spectroscopy. In this implantation test run, due to the IT decay of the ^{135m}Cs, the ion beam was deflected and implanted into a thin foil placed at the end of the spectroscopy line for direct detection of the gamma signature.

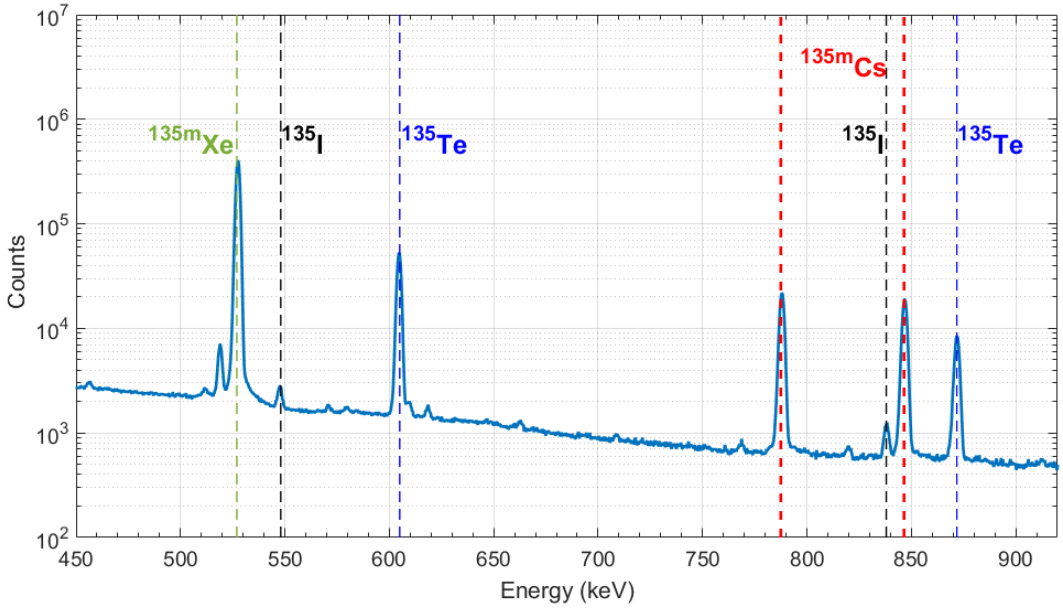

Figure 4.4: Gamma-ray energy spectrum from the 30-min implantation test of the ion beam with A=135 into the thin foil placed in front of a Canberra GC7020 Ge detector. For this measurement, the primary beam's intensity was set to 5 μA. The presence of the isotopes: ^{135}I, ^{135}Te and isomers: ^{135m}Xe and ^{135m}Cs was verified by matching the count-peaks with the characteristic γ-lines published in the literature.

The implantation lasted for 30 minutes, and the γ-rays from the gamma emitters with A=135 were recorded by a Canberra GC7020 Ge detector (energy range: 40 keV - 10

MeV) positioned right behind the foil. The spectrum, being the sum of all the γ-photons collected from the detector during the 30-min implantation, is shown in Fig. 4.4. Following a thorough analysis, the presence of the ^{135m}Cs was identified (see red dashed lines in Fig. 4.4) by its two characteristic γ-photons at 846.1 keV (M4) and 786.8 keV (E2). In addition, as it was expected, further gamma emitters with A=135 were present: ^{135m}Xe ($T_{1/2}$ =15.29(5) min) decaying to its ground state, ^{135}Xe ($T_{1/2}$ =9.14(2) h) -not shown above- decaying to ^{135}Cs, ^{135}I ($T_{1/2}$ =6.58(3) h) decaying to ^{135}Xe, and ^{135}Te ($T_{1/2}$ =19.0(2) s) decaying to ^{135}I [116]. For the calculation of the ^{135m}Cs implantation rate, the ion beam was blocked and two 30-min decay spectra were acquired consecutively. Then, by analysing the three spectra, the counts in the areas defined by the two characteristic γ-peaks of ^{135m}Cs, 846.1 and 786.8 keV, were calculated for each spectrum. Knowing that the number of isomers would exponentially decay with half-life $T_{1/2}$ =53 min, and taking into account the solid angle and efficiency of the Ge detector, an implantation rate 2$\times$10^4 ^{135m}Cs/s was measured for 5 μA primary beam intensity. The above number is a record for IGISOL, since as it was reported in Section 4.2.2, previous measurements at IGISOL's spectroscopy line had shown a rate of $\sim$9000 ^{135m}Cs/s for 10 μA of primary beam intensity.

In order to link the above rate to the implantation rate into the Y foil, the transmission efficiencies from the switchyard to the spectroscopy line and from the switchyard to the Y foil were calculated. For that purpose, ^{112}Rh ($T_{1/2}$ =3.6(3) s) was implanted in front of Si detectors in the spectroscopy line and in the switchyard, and the switchyard-spectroscopy line transmission efficiency was measured to be $\approx$70%. The half-life of ^{112}Rh is ideal for fast optimisation. Similarly to the procedure described in Section 4.2.1.1, the transmission efficiency to the Y foil was also calculated. In this case, we used ^{136}Xe(stable) and measured: 95 nA at the switchyard's Faraday cup and 38 nA at the Y foil, thus calculating an $\approx$40% switchyard-foil transmission efficiency. By comparing the two efficiencies and taking into account the measurements of the Ge detector, the implantation rate into the Y foil was calculated $\approx$1.2$\times$10^4 ^{135m}Cs$^+$/s.

To confirm the successful implantation of ^{135m}Cs into the neutraliser, γ-spectroscopy was also performed directly at the Y foil.

4.2.2.2 Gamma-ray spectra: implanted ions

The ion beam's implantation into the Y foil, lasted for two days, during which several γ-spectroscopy measurements showed an average implantation rate of approximately 1.9$\times$10^4

^{135m}Cs^{+}/s or $\sim 10^{-15}$ A. At the end of the implantation, the foil was allowed to "cool down" for 7 hours until it was safe to be handled. The "cool down" period is important to allow the short-lived species (e.g. ^{135}Sb, $T_{1/2}$ =1.679(15) s [116]) to decay, thus minimising the radiation dose delivered to the people handling the foil. The neutraliser was then placed in a low-background gamma-ray station and several γ-spectra were acquired in fixed time intervals for approximately 6 hours. The station consists of a Canberra BE3825 detector (energy range: 3 keV$-$3 MeV), and it is called "low-background" due to the lead castle with N_2 atmosphere that houses the detector's head and effectively reduces the background counts. Characteristic spectra of the γ-radiation emitted from the Y foil and recorded in the low-background station are shown in Fig. 4.5 for the energy range 780-860 keV.

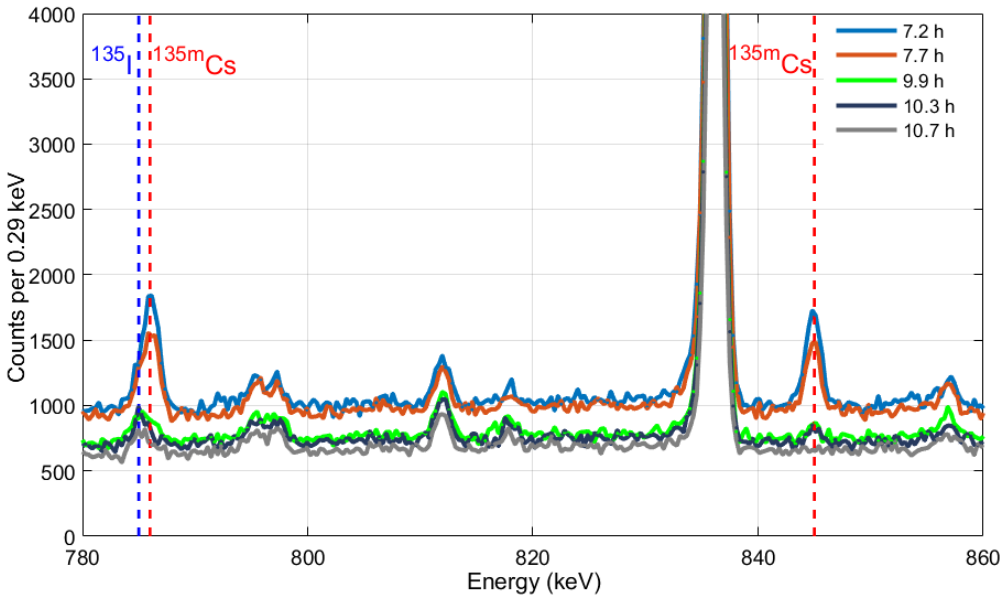

Figure 4.5: Gamma-ray energy spectra of the Y foil for energies 780 to 860 keV as they were recorded in the low-background station, for 7.2 (i.e. 432 min), 7.7, 9.9, 10.3 and 10.7 hours after the end of the implantation. The energy range was chosen in order to emphasize on the two ^{135m}Cs characteristic peaks: 846.1 keV (M4 transition) and 786.8 keV (E2 transition). In addition, the 785.48(5) keV ^{135}I peak ($T_{1/2}$ =6.58(3) h [116]) is also clearly observed in the last three spectra (9.9, 10.3 and at 10.7 h). The big peak on the left of the ^{135m}Cs 846.1 keV peak is the 836.8 keV ^{135}I peak (6.73% intensity).

In Fig. 4.5, the two characteristic peaks of ^{135m}Cs (846.1 and 786.8 keV) are present, which is consistent with the approximately 8 half-lives between the end of the implantation and the start of the spectrum's acquisition. In addition, this particular Y foil had been through heating cycles prior to the measurements, during development tests, thus an important portion of the implanted isomers, probably, was removed (thermal diffusion-depletion). In the first two spectra (7.2 and 7.7 h after implantation), both characteristic peaks can be identified, in the third and fourth spectra (9.9 and 10.3 h) only the 846.1 keV

peak, and in the last spectrum (10.7 h) none of the peaks seems to be present. The reason that in the third and fourth spectra only the 846.1 keV peak is clearly observed is due to the presence of an "interference" peak at ≈785 keV. The "interference" peak is the signature of the ^{135}I 785.48(5) keV γ-photon, which is produced by the fast de-excitation of its daughter nucleus ^{135}Xe [116]. In an attempt to independently measure the ^{135m}Cs half-life and unambiguously identify the presence of the isomer, the contribution of the iodine peak was subtracted.

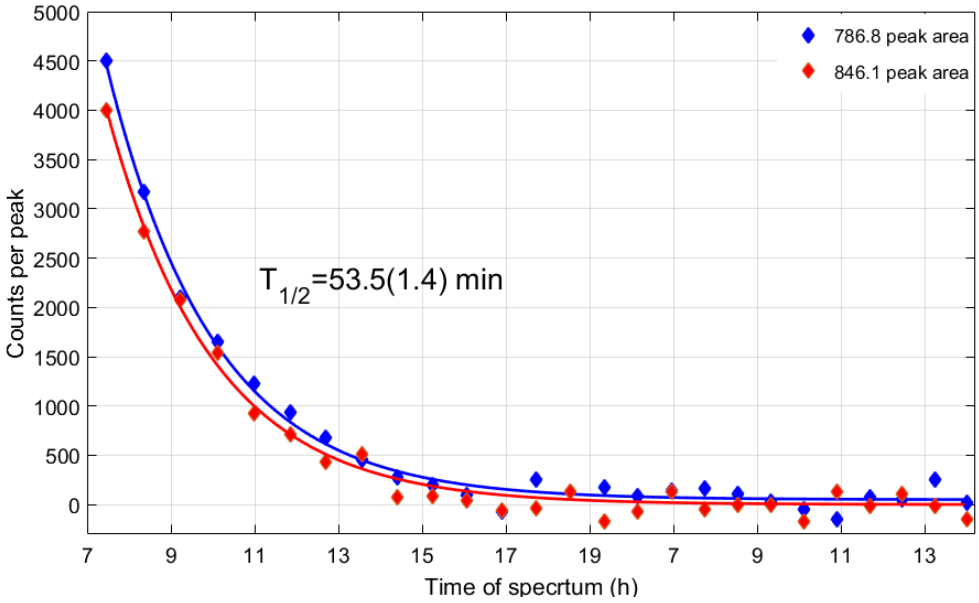

Figure 4.6: Decay curves of the two characteristic γ-peaks of the ^{135m}Cs.The data points represent the counts in the areas defined by each peak for multiple consecutively acquired 20-min spectra. By adding both set of data and fitting a single exponential, we calculate $T_{1/2}$ =53.5(1.4) min.

A standard methodology was followed for decoupling the two contributions. Firstly, in addition to the 785.48(5) keV (0.15% intensity) ^{135}I peak, a second peak was identified at 546.557(16) keV (7.15% intensity). For clarity, we will call the part of the count area defined by the 785.48 keV peak, which overlaps with the ^{135m}Cs 786.8 keV peak, as A^{I*}, the total count area defined by the stronger iodine peak as A^{I} and the total Cs peak count area as A^{Cs}. Then we calculate the ratio $r=A^{I*}/A^{I}$ for several spectra when both iodine peaks are observed with no interferences, and we find the average, r_{avg}. Finally, for all the spectra we calculate the counts of the 786.8 keV ^{135m}Cs peak as: $A=A^{Cs}-r_{avg}\cdot A^{I}$. The decay of the two peaks, after the successful subtraction of the iodine contribution, is shown in Fig. 4.6. By adding the data for the two peaks, and fitting them with a single exponential curve, we calculate $T_{1/2}$ =53.5(1.4) min [2], with the uncertainty being only statistical. Our calculation agrees with the previous published values by Warhanek et al. [117], $T_{1/2}$ =53(2) min and

by Häller et al. [118], $T_{1/2}$ =53(3) min.

4.2.2.3 Preliminary results of ^{135}Cs MOT

In a separate experiment, proton-induced fission fragments from a ^{nat}U target with A=135 were implanted into the Y foil for approximately 3 days (total 64 hours of implantation). The primary beam's energy was 50 MeV with 5 μA intensity. An average implantation rate, for the ^{135m}Cs, was measured $\approx$11.2$\times$10^3 isomers/s. Following the lack of success with the trapping of ^{134}Cs, ^{135}Cs was concluded to be the ideal Cs isotope for trapping because: 1) it has been already trapped, hence the published spectroscopic data are precise enough for laser cooling and 2) it is populated, not only directly from the fission reaction, but also indirectly from numerous other decaying isotopes and isomers (e.g. ^{135m}Cs, ^{135}I, ^{135}Xe etc.), while itself can be considered "stable" with $T_{1/2}$ =2.3$\times$10^6 years. The trapping efforts started almost one month after the end of the implantation, when it could be safely assumed that the majority of the radioactive isotopes and isomers would have decayed and, eventually, enhanced the ^{135}Cs population.

The two lasers were initially tuned on the calculated frequencies reported in Table 4.2, and the foil was operated at T$_Y$ >800 K to enhance thermal diffusion. During the experiment, the cooling laser's frequency was scanned $\pm$10 MHz or $\approx \pm 2\Gamma$ from the calculated frequency, and the repumper's relative frequency ranged from +140 to +410 MHz. We recall here the calculated relative (to the ^{133}Cs case) laser frequencies (see Table 4.2) for the ^{135}Cs: $\nu_c = -252$ MHz (-2.65Γ detuning included) and $\nu_r = +263$ MHz. The cooling laser's frequency can be controlled via a computer, thanks to the shifts provided by the chain of AOMs. This allowed us to lock the laser system to a known transition of ^{133}Cs. Therefore, we ran several trapping attempts by changing the cooling frequency in steps of 0.5Γ. The total cooling power available was 127 mW.

At the same time, because of the lack of locking for the repumper laser and the uncertainty on the best detuning, a two-fold strategy was employed. Firstly, the laser frequency was continuously swept around a given value by a 100 kHz sine wave. This roughly corresponded to a $\pm$55 MHz oscillation much faster that the MOT dynamics. As demonstrated in separate experiments with the ^{133}Cs$^+$ beam, this allows trapping even with slow drift of the laser frequency: at the $\sim$s time-scale, on average, the laser is always tuned at the right frequency. At the same time, the laser's central frequency (i.e. the 'centre-of-mass' of the fast sweep) was slowly modulated by a 10 mHz triangular waveform, between the aforementioned limits of +140 MHZ and +410 MHz. This slow sweep - monitored by the

wavemeter - ensured that all possible frequencies useful for trapping were covered. The total repumper power obtained in this condition was 15 mW.

By using this technique, preliminary evidence of ^{135}Cs trapping was obtained. Although it was not possible to confirm this finding because of depletion of the Y foil, post-analysis confirmed the significance of these results, well above the detection threshold of the system.

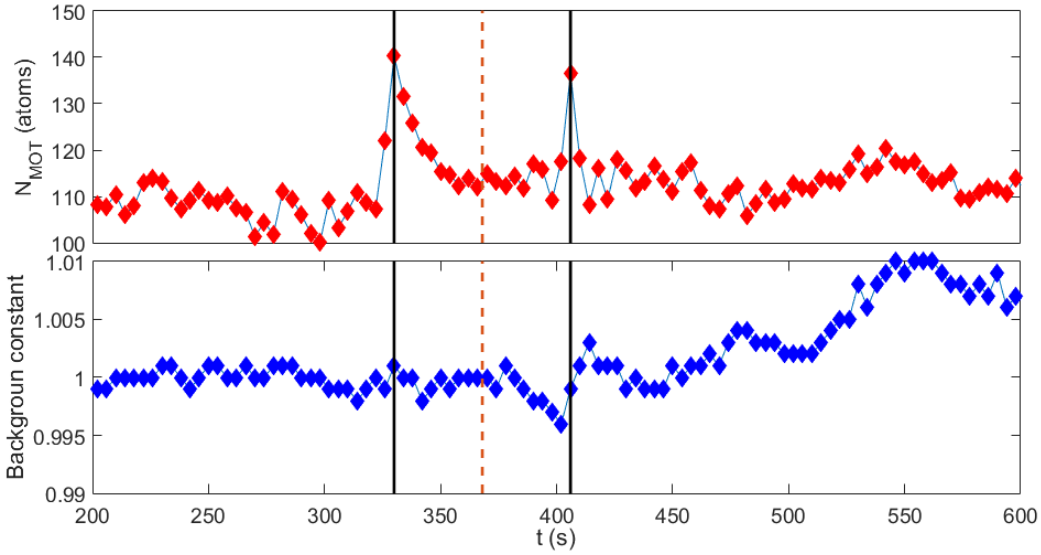

Figure 4.7: MOT fluorescence and background signals at -252 MHz (-2.65Γ detuning) cooling laser relative frequency shift and T_Y =880 K. The repumper relative frequency's central position was approximately $+150$ MHz, with a frequency modulation amplitude of 110 MHz. Top: MOT fluorescence signal. The solid lines mark the fluorescence's peaks and the dashed line marks the rough position of the repumper's scan inversion. Regarding the significance of the measured peaks, the first peak is $\approx 7\ \sigma$ higher than the mean background value and the second $\approx 6\ \sigma$. Bottom: the background constant representing the contribution of the background (mainly scattered light from the MOT beams) as recorded by the camera's CCD sensor.

In Fig. 4.7, two fluorescence peaks appear at t=330 s and t=406 s for a cooling detuning of -2.65Γ from resonance and the repumper's central relative frequency at approximately $+150$ MHz. The frequency of the repumper has the same value for the two peaks, which can be also seen by looking at the timings of the peaks, which are approximately symmetrical to the inversion of the sweep. The frequency of the cooling laser is consistent with the trapping frequencies reported in Di Rosa [14], while the repumper's central frequency is -allegedly- about $+113$ MHz (± 55 MHz modulation on top of that) far from the $+263$ MHz reported in Table 4.2.

The events were not repeatable hence no solid conclusion can be made. However, offline analysis and separate tests confirmed that: i) the signals are genuine, i.e. no spurious effect produced them; ii) influence from the background can be excluded, as demonstrated

by the on-line background monitoring (bottom part of Fig. 4.7); iii) the fluorescence level (here measured in number of atoms) is well above the detection limit of our system and the background statistical fluctuations (whose mean and standard deviation are equivalent to 111 and 4 atoms, respectively). Based on these considerations, we consider this event of ^{135}Cs MOT significant, although no final conclusion can be drawn at this stage. We attribute the lack of repeatability to the early depletion of ^{135}Cs in the Y foil. This is the main rationale pointing towards required improvements in the beam diagnostics closer to the trapping cell. This will provide us with a direct measurement of the incoming ions' rate and the opportunity to tackle the problem - if confirmed - of the facility's overall efficiency. Assuming that the $\nu_r = +263$ MHz calculated relative frequency and the measured central frequency detuning of the repumper at the time of trapping are correct, during the above measurement the frequency probably was only matched for a few seconds, when the scanning amplitude was positive and close to its maximum value. This may not be enough for populating a complete MOT with small population available. A MOT can be realised also when the repumper laser is red-detuned from the repump transition ([5] reports repumper detunings down to -50 MHz), but the trapping efficiency decreases significantly with the increase of the detuning's absolute value.

As anticipated, plans for characterising the facility's overall efficiency and improving it - if necessary - are already in place. In addition, the use of alternative radioactive atom supplies is investigated, and more trapping experiments for ^{134,134m,135,135m}Cs will be repeated in the near future.

Chapter 5

Conclusions and Outlook

This thesis reports on my work concerning the building and testing of a facility for laser cooling and trapping stable and unstable Cs atoms [2] at the Accelerator Laboratory of the University of Jyväskylä, Finland. The facility's operation was demonstrated by neutralising a $^{133}Cs^{+}$ beam, thermally diffusing the neutral ^{133}Cs atoms in the science chamber and trapping them in a MOT. Radioactive beam tests took place confirming the strong presence of ^{135m}Cs, an important candidate for γ-ray coherent emission [8]. Preliminary results of ^{135}Cs MOT were obtained. An important part of the work reported here was done in close collaboration with Dr. Luca Marmugi and our JYU colleagues: Dr. Sami Rinta-Antila, Dr. Ilkka Pohjalainen and Prof. Iain Moore. Mr. Tanapoom Poomaradee contributed as well, especially in designing and building the first version of the laser system (prior to updates).

The first phase of my work comprised the building of an off-line laser cooling and trapping set-up, and the realisation and full-characterisation of a ^{133}Cs MOT using a Cs reservoir as the atom supply. For that purpose, I tested and modified (when necessary) the laser system and built the trapping system (optics, vacuum and related hardware). In addition, I built the hardware and developed the software necessary to realise an absorption imaging system for characterising the MOT. Absorption imaging was used to measure the loading rate, lifetime, temperature, density and phase-space density of the MOT versus various parameters (laser intensity, detuning, magnetic field gradient, MOT population). The analysis of the behaviour of the MOT was essential for optimising the trap and creating optimum conditions for the next experimental phases. Having developed and tested the necessary tools for realising and characterising a MOT, I moved to the second experimental phase.

The second experimental phase was the building of a facility for laser cooling and trapping stable and unstable Cs isotopes, coupling to an accelerator and testing it. I built, in collaboration with IGISOL, the ion's beamline and tested the hardware and software which were used to deliver the ions to our chamber. The next part was the assembling and in-

stallation of the accelerator-coupled laser cooling and trapping set-up. A special chamber coated with an anti-adsorption organic coating was installed in one of the IGISOL's output ports. The optics were adjusted accordingly, and a fluorescence imaging system was designed and built to be used in the characterisation of the MOT. Tests with $^{133}Cs^{+}$ beams, produced in the off-line surface ionisation source at IGISOL-4, took place and the facility's operation was demonstrated [2]. The ions were implanted into the neutraliser Y foil, thermally diffused to the science chamber as neutral atoms, and eventually laser cooled and trapped in a MOT. The dynamics involved in the loading of the MOT from the hot neutraliser foil were identified and analysed. One loading process was characterised by fast dynamics and was describing the loading of the MOT from atoms coming from the surface of the Y foil. The second process was characterised by slow-dynamics during which the MOT was loaded primarily with atoms coming from the bulk of the foil. A lower limit in the facility's total efficiency was calculated, $\eta \geq 3\times10^{-6}$.

The last part of my work comprised the radioactive beam tests and the work towards the trapping of ^{134}Cs and ^{135}Cs. Proton-induced fusion-evaporation products of mass 134 (A=134) were implanted into our Y foil, while the laser system was tuned for the trapping of ^{134}Cs. There was not any obvious signature of the ^{134}Cs MOT, with one of the potential causes being the small incoming rate of the isotope. Next, we performed implantation runs of proton-induced fission fragments of mass 135 (A=135). In the first implantation run of A=135, γ-spectroscopy on the ion beam and the Y foil (after extraction from the chamber) successfully identified and quantified the strong presence of ^{135m}Cs [8]. Its half-life was then calculated, $T_{1/2}$ =53.5(1.4) min, in an agreement with the previously reported values. In the second run, the laser system was tuned according to the frequencies needed for a ^{135}Cs MOT. We measured two genuine fluorescence signals, believed to be signatures of the ^{135}Cs MOT, but due to the non-repeatability of the events no final conclusion could be made.

Taking into account the facility's short operation time, in combination with the high-value goals, one can understand that there are numerous improvements and updates to be made in the future. In the long-term, the facility will pass from the "cold" experimental stage to the "ultra-cold" and the achievement of quantum degeneracy in atomic samples of Cs isotopes and isomers. Entering into the ultra-cold era will open new and important avenues, including the testing of coherent γ-ray generation from the collapse of a ^{135m}Cs BEC and the investigation of many-body phenomena in ultra-cold nuclear matter. In addition and independently of the work towards coherent γ-rays, there is the possibility that the facility

will be updated according to the creation and validation of nuclear forensic techniques. In the following section, I will focus on updates that will take place in the near future, and for which I contributed in their planning.

5.1 Future work

Offset-lock

The tuning procedure of the repumper laser, described in Chapter 4, was done according to the frequency reading provided by a MOGLabs wavemeter ($\pm$ 10 MHz relative accuracy), without the possibility of a reliable locking system. Moreover, tuning the laser for different Cs isotopes was a time-consuming process. In order to overcome these difficulties, a Vescent Photonics offset phase lock system [119] was purchased, and its installation procedure has been initiated.

The offset phase lock system (OPLS) offers minimum optical losses, fast, precise and wide-range control of the laser's frequency detuning, based on the detection and manipulation of optical beat notes produced by the interference of two laser beams. The main components of OPLS systems are: two lasers (master and slave), one servo, one high-speed beat note detector and an external frequency reference (e.g. a frequency generator). The two laser beams (one from each laser) are overlapped and injected into the beat note detector, the optical beat notes are detected and then converted to electrical signals. The beat note generation procedure normally requires $\leq$500 μW power from each laser, i.e. almost negligible power losses for the laser system. The generated signals are then mixed with the reference frequency (in the servo module) generating an error signal, which is used to tune the slave laser and phase-lock it with the master.

In our experiment, the master laser will be locked using the DAVLL system (as described in Chapter 2), and the output of the slave laser (an additional laser will be added on the laser table) will be used as the repumper. The OPLS offers a tuning range up to $\geq$9.7 GHz, and a locking reliability which depends only on the external frequency generator's stability. The OPLS will allow us to tune the repumper laser for different isotopes much faster, only by controlling the external frequency generator via software (e.g. LabVIEW platform). Even more importantly, it will provide us with the option to lock the laser on a desired frequency. In the long-term, a similar system will be used for tuning the master laser, thus minimising power losses induced from the chain of AOMs and creating a fast, fully-automated procedure to trap different isotopes.

New Y design

The neutraliser mount system, shown in Chapter 3, Fig. 3.9, has been proven to be reliable, but its long-term stability is still being investigated. In addition, minor improvements to extend the average lifetime have been identified. A new design for the Y foil holder is currently under-way, addressing mainly issues related to the "non-optimum" condition of the system's electrical connection after a few months of frequent heating-cooling cycles with the same foil. Future improvements may also focus on the use of a linear actuator to move the foil closer to the chamber's aperture during implantation, and returning it to its initial position prior to the initiation of the thermal diffusion process. The presence of the linear actuator will provide us with the opportunity to ensure that the ion beam's focal point is on the Y foil, and depending on the geometry used, to reduce atomic losses from the chamber's pumping apertures.

MCP plates and detectors

To date, the $^{133}Cs^{+}$ beam used for demonstrating the operation of our facility is detected using Faraday cups (FC) and the neutraliser foil, which acts as the last beam diagnostic in our line. The limitation of FCs is that their lower detection limit is $\geq 10^{-12}$A or 10^{9} ions/s, which is significantly higher than the most intense radioactive beam. The addition of more and wider-range beam diagnostics will allow us to have a direct measurement of our system's response for low ion currents (as those during radioactive tests), and will lead to a precise estimation of our overall efficiency. Soon, a MagneTOF [120] detector from ETP Electron Multipliers Pty Ltd will be installed in the switchyard area, and potentially another one in our beamline. This particular type of ion detector will allow us to have a precise knowledge of the incoming ion current, with its detection capabilities ranging from Faraday cup amounts ($\sim 10^{10}$ ions/s) down to few ions per second.

Furthermore, updates will take place for the detection and monitoring of radioactivity, which will have a huge positive impact on the on-line radioactive experiments. Until now, the radioactivity monitoring of β-emitters was done by the Si detector positioned in the switchyard, or in the case of γ-emitters, the ion beam was directed to the spectroscopy line for γ-detection. Soon, a Si detector will be installed in our transport line on the same axis with the Faraday cup (see Chapter 3, Fig. 3.3, position (5)). The Si detector will allow us to have a direct identification and quantification of the incoming short-lived β-emitting isotopes, whose yield will be then used to calculate the rate of the long-lived incoming isotopes or/and isomers of interest.

Lower ion acceleration energies

As it was reported in Chapter 3, the accelerations used during the demonstration of the facility's operation are the highest in the literature. Lower acceleration energies, thus smaller implantation depths, will be used in order to reduce the ions' diffusion time and potentially increase the total efficiency of the system. In the future, the minimisation of the diffusion time will become crucial for short-lived isotopes such as ^{139}Cs with $T_{1/2}$ =9.3 min.

Bibliography

[1] Moore, I. D., T. Eronen, D. Gorelov, J. Hakala, A. Jokinen, A. Kankainen, V. S. Kolhinen, J. Koponen, H. Penttilä, I. Pohjalainen, M. Reponen, J. Rissanen, A. Saastamoinen, S. Rinta-Antila, V. Sonnenschein, and J. Äystö, "Towards commissioning the new IGISOL-4 facility," *Nuclear Instruments and Methods in Physics Research, Section B: Beam Interactions with Materials and Atoms*, vol. 317, no. PART B, pp. 208–213, 2013.

[2] Giatzoglou, A., T. Poomaradee, I. Pohjalainen, S. Rinta-Antila, I. D. Moore, P. M. Walker, L. Marmugi, and F. Renzoni, "A Facility for Production and Laser Cooling of Cesium Isotopes and Isomers," *Nuclear Instruments and Methods in Physics Research, Section A: Accelerators, Spectrometers, Detectors and Associated Equipment*, vol. 908, pp. 367–375, 2018.

[3] Gomez, E., L. A. Orozco, and G. D. Sprouse, "Spectroscopy with trapped francium: Advances and perspectives for weak interaction studies," *Reports on Progress in Physics*, vol. 69, no. 1, pp. 79–118, 2006.

[4] Bissell, M.L., K. Flanagan, M. Gardner, M. Avgoulea, J. Billowes, P. Campbell, B. Cheal, T. Eronen, D. Forest, J. Huikari, A. Jokinen, I. Moore, A. Nieminen, H. Penttilä, S. Rinta-Antila, B. Tordoff, G. Tungate, and J. Äystö, "On the decrease in charge radii of multi-quasi particle isomers," *Physics Letters B*, vol. 645, no. 4, pp. 330–334, 2007.

[5] Behr, J. A. and G. Gwinner, "Standard model tests with trapped radioactive atoms," *Journal of Physics G: Nuclear and Particle Physics*, vol. 36, no. 3, 2009.

[6] Agustsson, S., G. Bianchi, R. Calabrese, L. Corradi, A. Dainelli, A. Khanbekyan, C. Marinelli, E. Mariotti, L. Marmugi, G. Mazzocca, L. Moi, L. Ricci, L. Stiaccini, and L. Tomassetti, "Observation of $7p^2P_{3/2} \rightarrow 7d^2D_2$ optical transitions in 209 and 210 francium isotopes," *Optics Letters*, vol. 42, no. 18, p. 3682, 2017.

[7] Zhao, X, S. Crane, R. Guckert, and D. Vieira, “Hyperfine structure and isotope shift of ^{82}Rb D_1 and D_2 transitions,” *Physical Review A*, vol. 60, no. 6, p. 4730, 1999.

[8] Marmugi, L., P. M. Walker, and F. Renzoni, “Coherent gamma photon generation in a Bose – Einstein condensate of ^{135m}Cs,” *Physics Letters B*, vol. 777, pp. 281–285, 2018.

[9] Hu, J., A. Urvoy, Z. Vendeiro, V. Crépel, W. Chen, and V. Vuletić, “Creation of a Bose-condensed gas of ^{87} Rb by laser cooling,” *Science*, vol. 358, no. 6366, pp. 1078–1080, 2017.

[10] McCarron, D. J., H. W. Cho, D. L. Jenkin, M. P. Köppinger, and S. L. Cornish, “A Dual-Species Bose-Einstein Condensate of ^{87}Rb and ^{133}Cs,” *Physical Review A*, vol. 84, no. 1, p. 011603, 2011.

[11] Russell, B. C., I. W. Croudace, P. E. Warwick, and J. A. Milton, “Determination of precise ^{135}Cs/^{137}Cs ratio in environmental samples using sector field inductively coupled plasma mass spectrometry,” *Analytical Chemistry*, vol. 86, no. 17, pp. 8719–8726, 2014.

[12] Yang, Guosheng, H. Tazoe, and M. Yamada, “^{135}Cs activity and ^{135}Cs/^{137}Cs atom ratio in environmental samples before and after the Fukushima Daiichi Nuclear Power Plant accident,” *Scientific Reports*, vol. 6, p. 24119, 2016.

[13] Chino, Masamichi, H. Terada, H. Nagai, G. Katata, S. Mikami, T. Torii, K. Saito, and Y. Nishizawa, “Utilization of134Cs/137Cs in the environment to identify the reactor units that caused atmospheric releases during the Fukushima Daiichi accident,” *Scientific Reports*, vol. 6, no. August, pp. 1–14, 2016.

[14] Di Rosa, M.D., S. Crane, J. Kitten, W. Taylor, D. Vieira, and X. Zhao, “Magneto-optical trap and mass-separator system for the ultra-sensitive detection of ^{135}Cs and ^{137}Cs,” *Applied Physics B: Lasers and Optics*, vol. 76, no. 1, pp. 45–55, 2003.

[15] Russell, B.C., I. W. Croudace, and P. E. Warwick, “Determination of 135Cs and 137Cs in environmental samples: A review,” *Analytica Chimica Acta*, vol. 890, pp. 7–20, 2015.

[16] Soddy, Frederick, “Intra-atomic Charge,” *Nature*, vol. 92, no. 2301, pp. 399–400, 1913.

[17] Soddy, Frederick, “The stability of lead isotopes from thorium [1],” *Nature*, vol. 99, no. 2482, pp. 244–245, 1917.

[18] Hahn, Otto, “Über ein neues radioaktives Zerfallsprodukt im Uran,” *Die Naturwissenschaften*, vol. 9, no. 5, pp. 84–84, 1921.

[19] v. Weizsäcker, C. F., “Metastabile Zustände der Atomkerne,” *Naturwissenschaften*, vol. 24, no. 51, pp. 813–814, 1936.

[20] Dracoulis, G. D., P. M. Walker, and F. G. Kondev, “Review of metastable states in heavy nuclei,” *Reports on Progress in Physics*, vol. 79, no. 7, 2016.

[21] Walker, P. and G. Dracoulis, “Energy traps in atomic nuclei,” *Nature*, vol. 399, no. 6731, pp. 35–40, 1999.

[22] Loveland, W. D, D. J. Morrissey, and G. T. Seaborg, *Modern Nuclear Chemistry*. John Wiley & Sons, 2017.

[23] “Live Chart of Nuclides.” `https://www-nds.iaea.org/relnsd/vcharthtml/VChartHTML.html`. Accessed: October 2018.

[24] Blinder, S. M. , “Theory of Atomic Hyperfine Structure,” vol. 2 of *Advances in Quantum Chemistry*, pp. 47 – 91, Academic Press, 1966.

[25] Steck, D. A, “Cesium D Line Data.” `https://steck.us/alkalidata/cesiumnumbers.pdf`(revision 2.1.4, 23 December 2010). Accessed: November 2018.

[26] Arimondo, E., M. Inguscio, and P. Violino, “Experimental determinations of the hyperfine structure in the alkali atoms,” *Reviews of Modern Physics*, vol. 49, no. 1, pp. 31–75, 1977.

[27] Gerginov, V., A. Derevianko, and C. E. Tanner, “Observation of the Nuclear Magnetic Octupole Moment of ^{133}Cs,” *Physical Review Letters*, vol. 91, no. 7, pp. 4–7, 2003.

[28] Breit, G., “Theory of Isotope Shift,” *Reviews of Modern Physics*, vol. 30, no. 2, pp. 507–516, 1958.

[29] Otten, Ernst W, “Nuclear radii and moments of unstable isotopes,” in *Treatise on heavy ion science*, pp. 517–638, Springer, 1989.

[30] Ashkin, Arthur, “Acceleration and trapping of particles by radiation pressure,” *Physical Review Letters*, vol. 24, no. 4, p. 156, 1970.

[31] Hänsch, T. W. and A. L. Schawlow, "Cooling of gases by laser radiation," *Optics Communications*, vol. 13, no. 1, pp. 68–69, 1975.

[32] Wineland, D. J. and W. M. Itano, "Laser cooling of atoms," *Physical Review A*, vol. 20, no. 4, pp. 1521–1540, 1979.

[33] Phillips, W. D. and H. Metcalf, "Laser deceleration of an atomic beam," *Physical Review Letters*, vol. 48, no. 9, p. 596, 1982.

[34] Chu, S., L. Hollberg, J. E. Bjorkholm, A. Cable, and A. Ashkin, "Three-dimensional viscous confinement and cooling of atoms by resonance radiation pressure," *Physical Review Letters*, vol. 55, no. 1, p. 48, 1985.

[35] Raab, E. L., M. Prentiss, A. Cable, S. Chu, and D. E. Pritchard, "Trapping of neutral sodium atoms with radiation pressure," *Physical Review Letters*, vol. 59, no. 23, p. 2631, 1987.

[36] Lett, P. D., R. N. Watts, C. I. Westbrook, W. D. Phillips, P. L. Gould, and H. J. Metcalf, "Observation of atoms laser cooled below the doppler limit," *Physical Review Letters*, vol. 61, no. 2, pp. 169–172, 1988.

[37] Dalibard, J. and C. Cohen-Tannoudji, "Laser cooling below the Doppler limit by polarization gradients: simple theoretical models," *Journal of the Optical Society of America B*, vol. 6, no. 11, p. 2023, 1989.

[38] Anderson, M H, J. R. Ensher, M. R. Matthews, C. E. Wieman, and E. A. Cornell, "Evidence for Bose-Einstein Condensation in a Dilute Atomic Vapor," *Science*, vol. 269, no. 0, p. 3, 1995.

[39] Foot, C. J. *et al.*, *Atomic physics*, vol. 7. Oxford University Press, 2005.

[40] Metcalf, H. J. and P. Van der Straten, *Laser cooling and trapping*. Springer Science & Business Media, 2012.

[41] Li, R., K. Gibble, and K. Szymaniec, "Improved accuracy of the NPL-CsF2 primary frequency standard: evaluation of distributed cavity phase and microwave lensing frequency shifts," *Metrologia*, vol. 48, no. 5, p. 283, 2011.

[42] Xiaowei, Z., J. Zhong, B. Tang, X. Chen, L. Zhu, P. Huang, J. Wang, and M. Zhan, "Compact portable laser system for mobile cold atom gravimeters," *Applied Optics*, vol. 57, no. 22, pp. 6545–6551, 2018.

[43] Eto, Y., M. Sadrove, and T. Hirano, “Cold atom magnetometers,” in *Principles and Methods of Quantum Information Technologies*, pp. 111–133, Springer, 2016.

[44] Corwin, K. L., Z.-T. Lu, C. F. Hand, R. J. Epstein, and C. E. Wieman, “Frequency-stabilized diode laser with the Zeeman shift in an atomic vapor,” *Applied Optics*, vol. 37, no. 15, p. 3295, 1998.

[45] Chin, C., R. Grimm, P. Julienne, and E. Tiesinga, “Feshbach resonances in ultracold gases,” *Reviews of Modern Physics*, vol. 82, no. 2, pp. 1225–1286, 2010.

[46] Chin, C., V. Vuletić, A. J. Kerman, and S. Chu, “High resolution feshbach spectroscopy of cesium,” *Physical Review Letters*, vol. 85, no. 13, pp. 2717–2720, 2000.

[47] Bradley, C., “Design and realisation of an anti-Helmholtz and Feshbach coils system for ultra-cold atoms experiments with ^{133}Cs,” *University College London (UCL)*, 2015.

[48] Weiss, D. S., E. Riis, Y. Shevy, P. J. Ungar, and S. Chu, “Optical molasses and multilevel atoms: experiment,” *Journal of the Optical Society of America B*, vol. 6, no. 11, p. 2072, 1989.

[49] Anwar, M., V. Magalhães, S. T. Müller, M. Faisal, M. Nawaz, and M. Ahmed, “Revisiting the capture velocity of a cesium magneto-optical trap: Model, simulation and experiment,” *Laser Physics*, vol. 24, no. 12, 2014.

[50] Sesko, D., C. Monroe, A. Gallagher, T. Walker and C. Wieman, “Collisional losses from a light force atom trap,” *Physical Review Letters*, vol. 63, 961, no. 9, 1989.

[51] Suominen, Kalle-Antti, “Theories for cold atomic collisions in light fields,” *Journal of Physics B: Atomic, Molecular and Optical Physics*, vol. 29, no. 24, pp. 5981–6007, 1996.

[52] Gallagher, A. and D. E. Pritchard, “Exoergic collisions of cold Na*-Na,” *Physical Review Letters*, vol. 63, no. 9, pp. 957–960, 1989.

[53] Arnold, A. S. and P. J. Manson, “Atomic density and temperature distributions in magneto-optical traps,” *Journal of the Optical Society of America B*, vol. 17, no. 4, p. 497, 2000.

[54] Cooper, C. J., G. Hillenbrand, J. Rink, C. G. Townsend, K. Zetie, and C. J. Foot, “The temperature of atoms in a magneto-optical trap,” *Europhysics Letters*, vol. 28, no. 6, pp. 397–402, 1994.

[55] Drewsen, M., P. Laurent, A. Nadir, G. Santarelli, A. Clairon, Y. Castin, D. Grison, and C. Salomon, "Investigation of sub-Doppler cooling effects in a cesium magneto-optical trap," *Applied Physics B: Lasers and Optics*, vol. 59, no. 3, pp. 283–298, 1994.

[56] Overstreet, K., P. Zabawa, J. Tallant, a. Schwettmann, and J. Shaffer, "Multiple scattering and the density distribution of a Cs MOT," *Optics express*, vol. 13, no. 24, pp. 9672–9682, 2005.

[57] Townsend, C. G., N. H. Edwards, C. J. Cooper, K. P. Zetie, C. J. Foot, A. M. Steane, P. Szriftgiser, H. Perrin, and J. Dalibard, "Phase-space density in the magneto-optical trap," *Physical Review A*, vol. 52, no. 2, pp. 1423–1440, 1995.

[58] Sesko, D. W., T. G. Walker, and C. E. Wieman, "Behavior of neutral atoms in a spontaneous force trap," *Journal of the Optical Society of America B*, vol. 8, no. 5, p. 946, 1991.

[59] Walker, T., Sesko, David and Wieman, Carl, "Collective behavior of optically trapped neutral atoms," *Physical Review Letters*, vol. 64, no. 4, pp. 408–411, 1990.

[60] Marcassa, L. G., V. Bagnato, Y. Wang, C. Tsao, J. Weiner, O. Dulieu, Y. B. Band, and P. S. Julienne, "Collisional loss rate in a magneto-optical trap for sodium atoms: Light-intensity dependence," *Physical Review A*, vol. 47, no. 6, pp. 0–3, 1993.

[61] Weiner, John, "Experiments in cold and ultracold collisions," *Journal of the Optical Society of America B*, vol. 6, no. 11, p. 2270, 1989.

[62] Haw, M., N. Evetts, W. Gunton, J. Van Dongen, J. L. Booth, and K. W. Madison, "Magneto-optical trap loading rate dependence on trap depth and vapor density," *Journal of the Optical Society of America B*, vol. 29, no. 3, p. 475, 2012.

[63] Marcassa, L. G., K. Helmerson, A. M. Tuboy, D. M. Milori, S. R. Muniz, J. Flemming, S. C. Zílio, and V. S. Bagnato, "Collisional loss rate of sodium atoms in a magneto-optical trap operating on the D_1 line," *Journal of Physics B: Atomic, Molecular and Optical Physics*, vol. 29, no. 14, pp. 3051–3057, 1996.

[64] Van Dongen, J., C. Zhu, D. Clement, G. Dufour, J. L. Booth, and K. W. Madison, "Trap-depth determination from residual gas collisions," *Physical Review A*, vol. 84, no. 2, pp. 1–11, 2011.

[65] Fortagh, J., A. Grossmann, T. W. Hänsch, and C. Zimmermann, “Fast loading of a magneto-optical trap from a pulsed thermal source,” *Journal of Applied Physics*, vol. 84, no. 12, pp. 6499–6501, 1998.

[66] Fagnan, D. E., Wang, J. and Zhu, C., Djuricanin, P., Klappauf, B. G., Booth, J. L. and Madison, K. W., “Observation of quantum diffractive collisions using shallow atomic traps,” *Physical Review A*, vol. 80, no. 2, pp. 1–8, 2009.

[67] Telles, G. D., W. Garcia, L. G. Marcassa, V. S. Bagnato, D. Ciampini, M. Fazzi, J. H. Müller, D. Wilkowski, and E. Arimondo, “Trap loss in a two-species Rb-Cs magneto-optical trap,” *Physical Review A*, vol. 63, no. 3, pp. 1–7, 2001.

[68] Lindquist, K., M. Stephens, and C. Wieman, “Experimental and theoretical study of the vapor-cell Zeeman optical trap,” *Physical Review A*, vol. 46, no. 7, pp. 4082–4090, 1992.

[69] Sagna, N, G. Dudle, and P. Thomann, “The capture process in spherical magneto-optical traps: experiment and 1D magnetic field models,” *Journal of Physics B: Atomic, Molecular and Optical Physics*, vol. 28, pp. 3213–3224, 1995.

[70] Bagnato, V. S., L. G. Marcassa, S. G. Miranda, S. R. Muniz, and A. L. de Oliveira, “Measuring the capture velocity of atoms in a magneto-optical trap as a function of laser intensity,” *Physical Review A*, vol. 62, no. 1, p. 5, 2000.

[71] Magalhães, K. M. F., S. R. Muniz, G. D. Telles, P. W. Courteille, V. S. Bagnato, and L. G. Marcassa, “The Escape Velocity in a Magneto-Optical Trap and Its Importance to Trap Loss Investigation,” *Laser Physics*, vol. 12, no. 1, pp. 145–151, 2002.

[72] Muniz, S. R., K. M. Magalhães, P. W. Courteille, M. A. Perez, L. G. Marcassa, and V. S. Bagnato, “Measurements of capture velocity in a magneto-optical trap for a broad range of light intensities,” *Physical Review A*, vol. 65, no. 1, pp. 154021–154023, 2002.

[73] Hoffmann, D., S. Bali, and T. Walker, “Trap-depth measurements using ultracold collisions,” *Physical Review A*, vol. 54, no. 2, pp. R1030–R1033, 1996.

[74] Ritchie, N. W. M., E. R. Abraham, Y. Y. Xiao, C. C. Bradley, R. G. Hulet, and P. S. Julienne, “Trap-loss collisions of ultracold lithium atoms,” *Physical Review A*, vol. 51, no. 2, pp. 890–893, 1995.

[75] Wallace, C. D., T. P. Dinneen, K. Y. N. Tan, T. T. Grove, and P. L. Gould, "Isotopic difference in trap loss collisions of laser cooled rubidium atoms," *Physical Review Letters*, vol. 69, no. 6, pp. 897–900, 1992.

[76] Bali, S., K. M. O'Hara, M. E. Gehm, S. R. Granade, and J. E. Thomas, "Quantum-diffractive background gas collisions in atom-trap heating and loss," *Physical Review A*, vol. 60, no. 1, pp. R29–R32, 1999.

[77] Sesko, D., C. G. Fan, and C. E. Wieman, "Production of a cold atomic vapor using diode-laser cooling," *Journal of the Optical Society of America B*, vol. 5, no. 6, p. 1225, 1988.

[78] Gabbanini, C., A. Evangelista, S. Gozzini, A. Lucchesini, A. Fioretti, J. H. Müller, M. Colla, and E. Arimondo, "Scaling laws in magneto-optical traps," *Europhysics Letters*, vol. 37, no. 4, pp. 251–256, 1997.

[79] "Vaclon Plus 20 pumps User Manual," 2011.

[80] Stephens, M., R. Rhodes, and C. Wieman, "Study of wall coatings for vapor-cell laser traps," *Journal of Applied Physics*, vol. 76, no. 6, pp. 3479–3488, 1994.

[81] Gwinner, G., J. A. Behr, S. B. Cahn, A. Ghosh, L. A. Orozco, G. D. Sprouse, and F. Xu, "Magneto-optic trapping of radioactive $^{79}\mathrm{Rb}$," *Physical Review Letters*, vol. 72, pp. 3795–3798, 1994.

[82] Weber, K.-H. and C. J. Sansonetti, "Accurate energies of ns, np, nd, nf, and ng levels of neutral cesium," *Physical Review A*, vol. 35, no. 11, pp. 4650–4660, 1987.

[83] Speight, James G, *Lange's handbook of chemistry*, vol. 1. McGraw-Hill New York, 2005.

[84] Hölzl, J and F. Schulte, "Work function of metals," *Solid Surface Physics*, vol. 85, pp. 1–150, 1979.

[85] Gorelov, A., J. A. Behr, M. R. Kalita, M. R. Pearson, M. Tandecki, D. L, S. Aubin, R. Collister, A. C. Dehart, G. Gwinner, E. Gomez, L. A. Orozco, J. Z,, "Neutralizer for TRIUMF's experiment for measurements of parity non-conservation in francium," in *DNP16 Meeting of The American Physical Society Neutralizer*, vol. 61, 2016, abstract ID: BAPS.2016.DNP.HG.7.

[86] Crane, S. G., X. Zhao, W. Taylor, and D. J. Vieira, “Trapping an isotopic mixture of fermionic ^{84}Rb and bosonic ^{87}Rb atoms,” *Physical Review A*, vol. 62, no. 1, p. 011402, 2000.

[87] Agustsson, S., G. Bianchi, R. Calabrese, L. Corradi, A. Dainelli, A. Khanbekyan, C. Marinelli, E. Mariotti, L. Marmugi, L. Ricci, L. Stiaccini, L. Tomassetti, and A. Vanella, “Enhanced Atomic Desorption of 209 and 210 Francium from Organic Coating,” *Scientific Reports*, vol. 7, no. 1, pp. 1–7, 2017.

[88] Ziegler, J. F., M. D. Ziegler, and J. P. Biersack, “SRIM - The stopping and range of ions in matter (2010),” *Nuclear Instruments and Methods in Physics Research, Section B: Beam Interactions with Materials and Atoms*, vol. 268, no. 11-12, pp. 1818–1823, 2010.

[89] Burchianti, A., C. Marinelli, A. Bogi, E. Mariotti, S. Veronesi, F. Della Valle, G. Bevilacqua, and L. Moi, “Light-induced atomic desorption from PDMS films and porous glass: Application and fundamental issues,” *Journal of Physics: Conference Series*, vol. 19, no. 1, pp. 78–85, 2005.

[90] Bouchiat, M. A. and J. Brossel, “Relaxation of optically pumped Rb atoms on paraffin-coated walls,” *Physical Review*, vol. 147, no. 1, pp. 41–54, 1966.

[91] Budker, D., L. Hollberg, D. F. Kimball, J. Kitching, S. Pustelny, and V. V. Yashchuk, “Microwave transitions and nonlinear magneto-optical rotation in anti-relaxation-coated cells,” *Physical Review A*, vol. 71, no. 1, pp. 1–9, 2005.

[92] Scheer, M. D., R. Klein, and J. D. McKinley, “Surface Lifetimes of Alkali Metals on Molybdenum,” *The Journal of Chemical Physics*, vol. 55, no. 7, pp. 3577–3584, 1971.

[93] Aubin, S., E. Gomez, L. A. Orozco, and G. D. Sprouse, “High efficiency magneto-optical trap for unstable isotopes,” *Review of Scientific Instruments*, vol. 74, no. 10, pp. 4342–4351, 2003.

[94] Stephens, M. and W. C., “High Collection Efficiency in a Laser Trap,” *Physical Review Letters*, vol. 72, no. 24, pp. 3787–3790, 1994.

[95] Akoum, R. A., Vaulot, C. , Schwartz, D. , Hirn, M. and Haidar, B., “How Silanization of Silica Particles Affects the Adsorption of PDMS Chains on Its Surface,” *Journal of Polymer Science Part B: Polymer Physics*, vol. 48, pp. 2371–2378, 2007.

[96] Mariotti, E., S. Atutov, M. Meucci, P. Bicchi, C. Marinelli, and L. Moi, "Dynamics of rubidium light-induced atom desorption (LIAD)," *Chemical Physics*, vol. 187, no. 1-2, pp. 111–115, 1994.

[97] Atutov, S. N., R. Calabrese, V. Guidi, B. Mai, A. G. Rudavets, E. Scansani, L. Tomassetti, V. Biancalana, A. Burchianti, C. Marinelli, E. Mariotti, L. Moi, and S. Veronesi, "Fast and efficient loading of a Rb magneto-optical trap using light-induced atomic desorption," *Physical Review A*, vol. 67, no. 5, p. 053401, 2003.

[98] Marinelli, C., A. Burchianti, A. Bogi, F. Della Valle, G. Bevilacqua, E. Mariotti, S. Veronesi, and L. Moi, "Desorption of Rb and Cs from PDMS induced by non resonant light scattering," *European Physical Journal D*, vol. 37, no. 3, pp. 319–325, 2006.

[99] Gozzini, S. and A. Lucchesini, "Light-induced potassium desorption from polydimethylsiloxane film," *European Physical Journal D*, vol. 28, no. 2, pp. 157–162, 2004.

[100] Lu, Z.-T., K. L. Corwin, K. R. Vogel, C. E. Wieman, T. P. Dinneen, J. Maddi, and H. Gould, "Efficient Collection of ^{221}Fr into a Vapor Cell Magneto-optical Trap," *Physical Review Letters*, vol. 79, no. 6, pp. 994–997, 1997.

[101] Coppolaro, V., N. Papi, A. Khanbekyan, C. Marinelli, E. Mariotti, L. Marmugi, L. Moi, L. Corradi, A. Dainelli, H. Arikawa, T. Ishikawa, Y. Sakemi, R. Calabrese, G. Mazzocca, L. Tomassetti, and L. Ricci, "Light desorption from an yttrium neutralizer for Rb and Fr magneto-optical trap loading," *Journal of Chemical Physics*, vol. 141, no. 13, pp. 0–9, 2014.

[102] Lucchesini, A., S. Gozzini, C. Marinelli, and L. Marmugi, "Low Energy Atomic Photodesorption from Organic Coatings," *Coatings*, vol. 6, no. 4, p. 47, 2016.

[103] Garrison, B. J., N. Winograd, D. M. Deaven, C. T. Reimann, D. Y. Lo, T. A. Tombrello, D. E. Harrison, and M. H. Shapiro, "Many-body embedded-atom potential for describing the energy and angular distributions of Rh atoms desorbed from ion-bombarded Rh{111}," *Physical Review B*, vol. 37, no. 13, pp. 7197–7204, 1988.

[104] Udem, Th., J. Reichert, R. Holzwarth, and T. W. Hänsch, "Absolute Optical Frequency Measurement of the Cesium D_2 line," *Physical Review Letters*, vol. 82, no. 18, pp. 3568–3571, 1999.

[105] Thibault, C., F. Touchard, S. Büttgenbach, R. Klapisch, M. De Saint Simon, H. Duong, P. Jacquinot, P. Juncar, S. Liberman, P. Pillet, J. Pinard, J. Vialle, A. Pesnelle, and G. Huber, "Hyperfine structure and isotope shift of the D_2 line of $^{118^{\vee}145}$Cs and some of their isomers," *Nuclear Physics A*, vol. 367, no. 1, pp. 1–12, 1981.

[106] Fuller, Gladys H., "Nuclear Spins and Moments," *Journal of Physical and Chemical Reference Data*, vol. 5, no. 4, pp. 835–1092, 1976.

[107] Ackermann, F., E. Otten, G. zu Putlitz, A. Schenck, and S. Ullrich, "Determination of the spectroscopic quadrupole moments of ^{131}Cs, ^{132}Cs and ^{136}Cs," *Nuclear Physics A*, vol. 248, no. 2, pp. 157–172, 1975.

[108] Svanberg, S. and S. Rydberg, "Level crossing investigation of the $6p^2P_{3/2}$ and $7p^2P_{3/2}$ levels of Cs^{133}, Cs^{135}, and Cs^{137}," *Zeitschrift für Physik A Hadrons and nuclei*, vol. 227, no. 3, pp. 216–233, 1969.

[109] Stroke, H. H., V. Jaccarino, D. S. Edmonds, and R. Weiss, "Magnetic moments and hyperfine-structure anomalies of Cs^{133}, Cs^{134}, Cs^{135}, and Cs^{137}," *Physical Review*, vol. 105, no. 2, pp. 590–603, 1957.

[110] Svanberg, S and G. Belin, "Redetermination of the hyperfine structure of the $6p^2P_{3/2}$ in Cs^{133} by the zero field optical double resonance method," *Zeitschrift für Physik A Hadrons and nuclei*, vol. 251, no. 1, pp. 1–5, 1972.

[111] Sonzogni, A. A., "Nuclear data sheets for A = 134," *Nuclear Data Sheets*, vol. 103, no. 1, pp. 1–182, 2004.

[112] Mughabghab, S. F., *Atlas of Neutron Resonances: Resonance Parameters and Thermal Cross Sections. Z= 1-100*. Elsevier, 2006.

[113] Penttilä, H., P. Karvonen, T. Eronen, V. V. Elomaa, U. Hager, J. Hakala, A. Jokinen, A. Kankainen, I. D. Moore, K. Peräjärvi, S. Rahaman, S. Rinta-Antila, V. Rubchenya, A. Saastamoinen, T. Sonoda, and J. Äystö, "Determining isotopic distributions of fission products with a Penning trap," *European Physical Journal A*, vol. 44, no. 1, pp. 147–168, 2010.

[114] De Laeter, J. R., J. K. Böhlke, P. De Bièvre, H. Hidaka, H. S. Peiser, K. J. R. Rosman, and P. D. P. Taylor, "Atomic weights of the elements. Review 2000 (IUPAC Technical Report)," *Pure and Applied Chemistry*, vol. 75, no. 6, pp. 683–800, 2003.

[115] Tilley, D.R., H. Weller, and C. Cheves, "Energy levels of light nuclei A = 16–17," *Nuclear Physics A*, vol. 564, no. 1, pp. 1–183, 1993.

[116] Singh, B., A. A. Rodionov, and Y. L. Khazov, "Nuclear Data Sheets for A = 135," *Nuclear Data Sheets*, vol. 109, no. 3, pp. 517–698, 2008.

[117] Warhanek, Hans, "A 53 min isomer of caesium 135," *Nuclear Physics*, vol. 33, pp. 639–647, 1962.

[118] Häller, I.B. and B. Jung, "Spin-parity of 53 min Cs^{135m}," *Nuclear Physics*, vol. 52, pp. 524 – 528, 1964.

[119] "D2-135 Offset Phase Lock Servo, Vescent electronics." `https://www.vescent.com/products/electronics/d2-135-offset-phase-lock-servo/`. Accessed: November 2018.

[120] "MagneTOF, ETP Electron Multipliers." `https://www.etp-ms.com/technology/the-etp-difference/ion-detection`. Accessed: November 2018.